TOPICAL REVIEW • OPEN ACCESS

Powering internet-of-things from ambient energy: a review

IOP Publishing J. Phys. Energy 5 (2023) 022001 https://doi.org/10.1088/2515-7655/acb5e6

Journal of Physics: Energy

TOPICAL REVIEW

Powering internet-of-things from ambient energy: a review

Arindom Chatterjee[1], Carlos Nuñez Lobato[1], Haiwu Zhang[1], Achilles Bergne[1], Vincenzo Esposito[1], Shinhee Yun[1], Andrea Roberto Insinga[1], Dennis Valbjørn Christensen[1], Carlos Imbaquingo[1], Rasmus Bjørk[1], Hamsa Ahmed[3], Mariam Ahmad[3], Chun Yuen Ho[3], Morten Madsen[3], Jixi Chen[1], Poul Norby[1], Francesco Maria Chiabrera[1], Felix Gunkel[1,4], Ziwei Ouyang[2] and Nini Pryds[1,*]

[1] Department of Energy Conversion and Storage, Technical University of Denmark, DK-2800 Kongens Lyngby, Denmark
[2] Department of Electrical Engineering, Technical University of Denmark, DK-2800 Kongens Lyngby, Denmark
[3] Mads Clausen Institute, SDU NanoSYD, University of Southern Denmark, 6400 Sønderborg, Denmark
[4] Peter Gruenberg Institute (PGI-7), Forschungszentrum Juelich GmbH, 52425 Juelich, Germany; Juelich-Aachen Research Alliance (JARA-FIT), 52425 Juelich, Germany
* Author to whom any correspondence should be addressed.

E-mail: nipr@dtu.dk

Keywords: internet-of-things, energy harvesting devices, energy storage devices, power management

OPEN ACCESS

RECEIVED
5 April 2022

REVISED
17 October 2022

ACCEPTED FOR PUBLICATION
29 November 2022

PUBLISHED
14 February 2023

Abstract

Internet-of-thing (IoT) is an assembly of devices that collect and share data with other devices and communicate via the internet. This massive network of devices, generates and communicates data and is the key to the value in IoT, allowing access to raw information, gaining insight, and making an intelligent decisions. Today, there are billions of IoT devices such as sensors and actuators deployed. Many of these applications are easy to connect, but those tucked away in hard-to-access spots will need to harvest ambient energy. Therefore, the aim is to create devices that are self-report in real-time. Efforts are underway to install a self-powered unit in IoT devices that can generate sufficient power from environmental conditions such as *light, vibration*, and *heat*. In this review paper, we discuss the recent progress made in materials and device development in power- and, storage units, and power management relevant for IoT applications. This review paper will give a comprehensive overview for new researchers entering the field of IoT and a collection of challenges as well as perspectives for people already working in this field.

Contents

1. Introduction

The internet of things (IoT) is a giant network that connects a huge number of physical objects—'things'-through the internet. Remote accessibility and automatization allow us to perform tasks efficiently and repeatedly. IoT is considered one of the leading technologies, which is projected to increase and reach 50 billion devices by the year 2030 [1, 2]. Applications of IoT are primarily based on low-power consumable devices, which are used in home appliances or automation [3], hospitals [1], and healthcare [4, 5] as well as in numerous industrial processes [6]. Typically, IoT devices receive or generate data and then transmit it wirelessly to other devices to perform any given task. It consists of mainly three parts: IoT units (wireless sensor networks (WSNs), processors, actuators, etc), power units, and electronics.

Powering billions of devices remains an open technological challenge. At the same time, the installation of billions of devices will require the miniaturization of IoT units, power units, and electronics. Therefore, IoT-based industries face several technological challenges: (a) creating low-power electronics, including wireless communications, sensors, and actuators, (b) producing reliable and maintenance-free autonomous powering devices with a long life span, (c) developing low-cost fabrication technology that supports the miniaturization of billions of IoT units, and (d) creating reliable and safe wireless communication methods [7–10].

The current technological solution for powering IoT-based devices mainly relies on the battery industries [11–15]. However, their lifetimes are generally much less than the expected lifetimes of the WSNs and hence, replacement of batteries is required periodically to keep the devices operational. This creates extra expenses and additional complications for remote sensors, and in some cases, it can even be impossible to replace batteries. Moreover, batteries are expensive, bulky, and contain harmful chemicals. Although an effort is currently taken to improve the energy storage capacity and therefore the lifetime of IoT devices, the miniaturization of batteries remains a major technological challenge.

As an alternative, a self-powered unit can be installed in the IoT devices, which can harness sufficient power from ambient energy sources [16]. Usually, a few energy conversion technologies are available to date which can convert various sources of ambient energy into electricity. Some examples are a) thermoelectric (TE) or pyroelectric generators, which can harness energy from ambiance waste heat, b) piezoelectric, flexoelectric, and electromagnetic vibration energy devices which can convert mechanical (vibrational) energy to electric voltage; c) photovoltaic devices, which can convert light into electricity etc. Depending on the available ambient energy sources and conversion efficiencies, these energy-harvesting technologies can power varieties of IoT devices, as shown in figure 1. The energy demand for low-power IoT devices typically lies between several microwatts (μWs) to a few milliwatts (mWs) or between 10–1000 μW cm^{-2} in terms of area-specific power density [17].

In this review paper, we report the current developments in the above mentioned important powering- and storage units, and the electronics of IoT devices. The paper is divided into three sections: section 2 describes energy harvesting devices, which include energy harvesting only from ambient heat, vibration, and light. Section 3 describes energy storage devices, which is mainly devoted to batteries. The use of micro-fuel cells for on-demand powering of IoT devices is included in this section. Section 4 describes the electronic power management for IoT devices.

It is noteworthy that other energy harvester- (wind- [17, 18], bio-waste- [19, 20], electromagnetic radiation energy [21]), storage devices (supercapacitors [22–28]) and the economic competitiveness of these devices for IoT applications [29–31] are not discussed here due to the large volume of this article. Above referred articles might help readers to dive deeper into each topic.

2. Section-I: energy harvesting devices

In this section, we present five different types of harvesting devices, which include thermoelectricity, piezoelectricity, flexo-electricity, electromagnetic vibration energy harvesters, and photovoltaics (PV).

2.1. Thermoelectricity for IoT applications

A few comprehensive review articles are published in the literature based on the μ-TE generators [32, 33], wearable TE generators [34–36], and the use of TE devices for the IoT applications [29, 37]. Here, we have updated the current developments on the materials and micro-devices, which are potential for IoT applications.

TE devices are considered as one of the attractive solutions for powering IoT-based WSNs due to their long operational lifetime, high reliability, and more importantly, their maintenance-free characteristics [38]. These devices are capable of converting electric voltage output directly from ambient heat sources using the Seebeck effect, without involving any mechanical part on it. Typically, a thermoelectric generator (TEG)

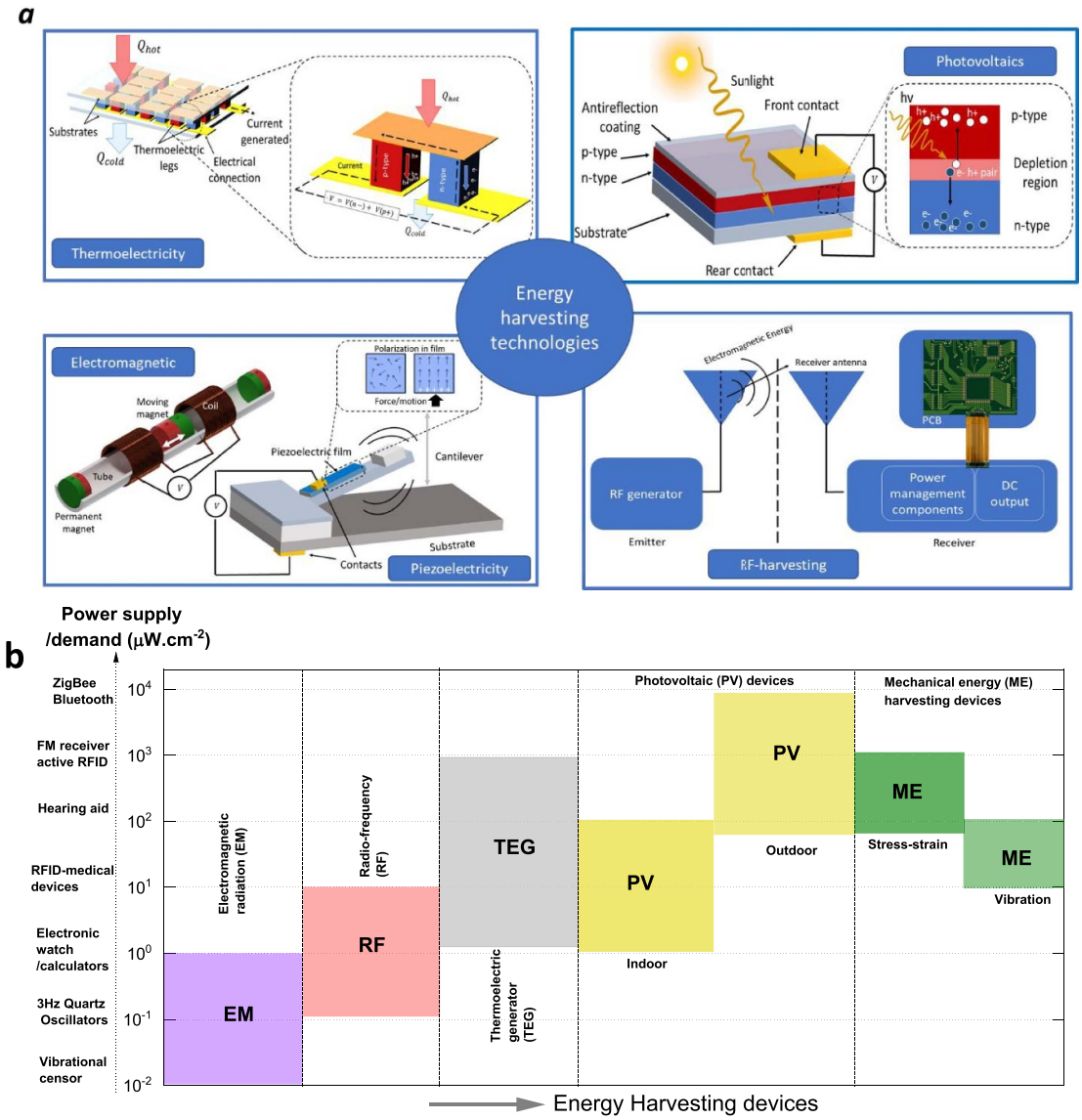

Figure 1. Example of energy conversion devices relevant for internet-of-thing applications. (a) Device architectures of thermoelectric-, photovoltaic-, piezoelectric-, and radio frequency generators. (b) Energy spectrum of specific power requirements of variable wireless sensor nodes and the energy supplying capabilities of different harvesting devices. Actual conditions for the operating devices are listed in tables in their respective sections.

consists of both p- and n-type semiconductors (that is, p–n thermocouples) that are connected electrically in a series but thermally in parallel [39]. The maximum achievable conversion efficiency of such TEG (η_{TEG}) is given by equation (1) [40]:

$$\eta_{\mathrm{TEG}} = \frac{T_{\mathrm{Hot}} - T_{\mathrm{Cold}}}{T_{\mathrm{Hot}}} \frac{\sqrt{1+ZT}-1}{\sqrt{1+ZT}+\frac{T_{\mathrm{Cold}}}{T_{\mathrm{Hot}}}}, \tag{1}$$

The overall efficiency depends on (a) the Carnot efficiency ($\frac{T_{\mathrm{Hot}}-T_{\mathrm{Cold}}}{T_{\mathrm{Hot}}}$), and (b) the TE figure of merit (ZT). The quality of a TE material is determined by the factor ZT ($ZT = \frac{\sigma S^2}{\kappa} T$; where σ, S, κ, and T are electrical conductivity, Seebeck coefficient, thermal conductivity, and the mean temperature between the hot, and the cold end, respectively). Therefore, it suggests that an appropriate design of the device for the propagation of heat flux from the hot to the cold end [41], and the use of high ZT materials are essential to achieve high-energy conversion efficiency. However, the output power is equally important as the efficiency for some miniature devices (such as IoT-based WSNs, micro-temperature sensors, etc.) [42] because the amount of heat flow from the hot to the cold reservoir in such devices is very small [43]. Depending on the ambient temperature sources and the materials used, TEGs are capable of supplying power to those WSNs in a spectrum that lies between 10 and 1000 μW cm^{-2} as shown in figure 1(b) (see also figures 18–20 in [37]).

2.1.1. Materials

Implementation of both p- and n-type semiconducting materials with high ZT is necessary to achieve maximum conversion efficiency in a TEG. Obtaining materials with high ZT is challenging because (a) the electronic conductivity and the electronic part of the thermal conductivities are interrelated to each other through the density of charge carriers according to Wiedemann–Franz law [44], and (b) in a band-gap material, the electrical conductivity and the Seebeck coefficients behave oppositely as a function of the density of charge carriers [45]. Hence, optimization of the density of charge carriers and the minimization of the lattice part of the thermal conductivity is required, independently [44, 46]. As shown in figure 2, the library of TE materials shows many families of compounds with $0.5 \leqslant ZT < 3$ [47]. Examples include Skutterudites [48], half-Heusler [49, 50] clathrates [51], zintal-phase [52–54], silicates [55], silicon-germanium [56], heavy metal-based chalcogenides [57, 58], transition-metal-based oxides [59–61] etc. Recently, polycrystalline SnSe-based chalcogenides exhibit ZT slightly above 3 (i.e. $2 < ZT_{max} < 3.2$) [62–64] but only at higher temperatures (∼800–1000 K). Therefore, their use for near room-temperature applications remains unattainable. Additionally, not all of these materials have been implemented in devices and therefore, additional challenges associated with electrical contact resistance [65] and thermal contact resistances [66] are not known. Recently, half-Heusler-based thin films grown on silicon substrates show an estimated $ZT_{max} \approx 6$ near 75 °C [67]). This value is extremely high due to the fact that the figure of merit was calculated by combining power factor measured in the in-plane direction together with the thermal conductivity measured in the out-of-plane direction. Nonetheless, although this value should be taken with caution, it is interesting to point out that films were deposited on silicon substrates. n-type organic TE materials also exhibit potential figure-of-merit (FOM) ($ZT > 0.3$ at 120 °C [68]), which can be used to convert energy from waste heat of a human body (i.e. in wearable devices).

2.1.2. Devices

Appropriate design of the device architecture allows for improving the device performance by reducing electrical- and thermal contact resistance [69]. On the other hand, technologies that allow a high-density integration of thermocouples can generate sufficient power output even by using a low ZT material (such as silicon) [42]. As the power output from a TEG device is more relevant for IoT-based applications [42], our discussion includes the progress on the overall power output but not the overall efficiency. The power output of a TEG is proportional to the cross-section area of the device (A) and the square of the applied temperature gradient ($(\Delta T)^2$). Usually, two parameters are used in the literature to quantify the power output capacity of TEGs; area-specific power density (i.e. $P_A = P_{max}/A$) and specific power generation capacity ($\Gamma_P = P_{max}/[A.(\Delta T)^2]$).

A list of commercial TEGs and their performance can be found in [29, 37]. The power output of some commercial TEGs can be as high as 0.69 W cm^{-2}, where the temperature at the hot end and the footprint area were 500 °C and 5.6 × 5.6 cm^2, respectively [29]. This indicates that commercial TEGs can power a long-range of IoT-based sensors [37]. However, the footprint area of IoT-based devices shrinks continuously (<1 cm^3) [37, 70] and so, more attention is paid to the miniaturization of TEGs [43, 69]. In this sense, the development of cost-effective micro-devices (μ-TEGs) is becoming significantly important.

Depending on the propagation of heat from the hot to the cold reservoir, μ-TEGs devices can have three different architectures; planar, vertical, and hybrid [32, 33]. Thermocouples are suspended on a membrane (or substrates) in a planar TEG device and heat propagates parallel to the substrates. The membranes used in this design often show poor mechanical stability and a large parasitic heat transfer but remain technologically important as are compatible with the silicon integrated circuit technology. Temperature gradients and the power output in this architecture can be tuned by optimizing the length and the thickness of thermocouples. In a vertical μ-TEG, thermocouples are placed vertically and so heat propagates vertically to the substrate. A large density of thermocouples can be integrated with this device layout and high power output can be achieved, which can further be tuned by controlling the width of the thermocouples [69]. Some of the common features of the vertical and planar designs are merged in a hybrid configuration where heat flows out-of-plane of the substrate but current flow in-plane and therefore have some more flexibilities [71]. In this layout, cavities are created in the substrate below the thermocouple pair to further suppress the heat flow [29, 32, 71]. The performances of a long list of μ-TEGs with different device layouts and with different TE materials can be found in [32] and some recent advancements are shown in table 1 in this article.

Incompatibility of exotic TE materials such as Bi_2Te_3, PbTe, SnSe, etc into silicon technology prevents their applications in the area of IoT and microelectronics. Only a few silicon-based materials such as Si and SiGe are compatible with silicon-based micro-fabrication techniques. As discussed in the materials section, SiGe-based materials are one of the promising TE materials used in space missions [38], which work more efficiently at nanoscales especially due to the reduced total thermal conductivity [56]. Recently, SiGe nanowire-based μ-TEG fabricated by using micro-electro-mechanical system (MEMS) technology shows a

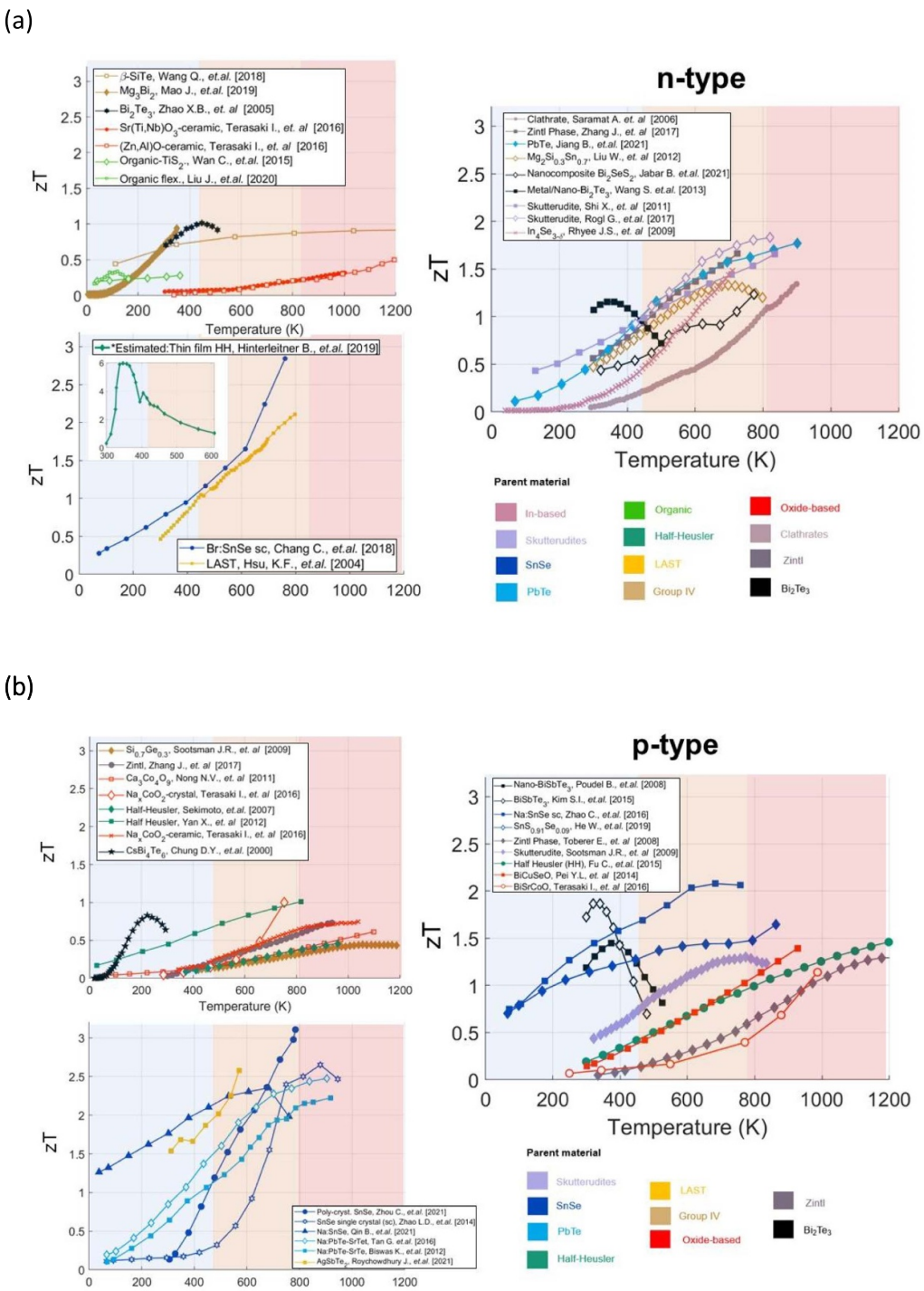

Figure 2. State-of-the-art p- and n-type thermoelectric materials with a high thermoelectric figure of merit (*ZT*). (a)-temperature dependence on the *ZT* of the best p-type materials reported to date. **Materials with 0 < *ZT* ⩽1**- Zintl phase (Toberer *et al* [72]) half-Heusler (Yan *et al* [73]), half-heusler (Sekimoto *et al* [74]), $Ca_3Co_4O_9$ ceramic (Nong *et al* [75]), Na_xCoO_2-crystal and ceramic (Terasaki [59]), $CsBi_4Te_6$ (Chung *et al* [76]), p-$Si_{0.7}Ge_{0.3}$ (Sootsman *et al* [46]); **materials with 0 < ZT ⩽2** $Bi_2Sr_2Co_2O_x$, (Terasaki [59]), BiCuSeO (Pei *et al* [77]), Nanocomposite-$BiSbTe_3$ (Poudel *et al* [78]), $BiSbTe_3$ (Kim *et al* [79]), Na:SnSe-single crystal (Zhao *et al* [80]), $SnS_{0.91}Se_{0.09}$ (Wenke *et al* [81]), Skutterudiet (Sootsman *et al* [46]), half-heusler (Fu *et al* [82]). **Materials with 0 < ZT ⩽3** polycrystalline-SnSe (Zhou *et al* [64]), single-crystalline-SnSe (Zhao *et al* [83]), 1.5%Na-SnSe (Qin *et al* [84]), PbTe-SrTe (Tan *et al* [58]), Na-PbTe-SrTe (Biswas *et al* [85]), $AgSbTe_2$ (Roychowdhury *et al* [86]). (b)- temperature dependence on the ZT of the state-of-the-art n-type materials. **Materials with 0 < ZT ⩽1**- n-Bi_2Te_3 (Zhao *et al* [87]), SiTe (Wang *et al* [88]), Mg_3Bi_2 (Mao *et al* [89]), Half-Heusler, $Y_{14}Mn_{1-x}Al_xSb_{11}$, $Sr(Ti,Nb)O_3$ and ZnO:Al (Terasaki [59]), TiS_2 (Wan *et al* [90]), Organic thermoelectric (Liu *et al* [68]); **materials with 0 < ZT ⩽2**- Zintl phase (Zhang *et al* [91]), Clathrates (Saramat [92]), PbSe (Jiang *et al* [93]), $Mg_2Si_{0.3}Sn_{0.7}$ (Liu *et al* [94]), nanocomposite-Bi_2SeS_2 (Jabar *et al* [95]), metal-nano +Bi_2Te_3 (Wang *et al* [96]), Skutterudites (Shi *et al* [97]), Skutterudites (Rogl *et al* [48]), $In_4Se_{3-\delta}$ crystal (Rhyee *et al* [98]); **materials with 0 < ZT ⩽3**- half-heusler thin film (Hinterleitner *et al* [67]), Br:SnSe single crystal (Chang *et al* [99]), LAST-$AgPb_{10}SbTe_{12}$ (Hsu *et al* [100]). Different colored regimes in the figures represent different ranges of temperatures.

Table 1. Comparison of the electrical power output and footprint areas of commercial TEGs, micro-TEGs based on the Bi_2Te_3-Sb_2Te_3 family, organic TEGs, and micro-TEGs that are compatible with MEMS and CMOS technologies. $P_A = (P_{max}/A)$; $\Gamma_A = [P_{max}/(A.(\Delta T)^2)]$. P_{max} and A are the maximum power output and the footprint area of the device, respectively.

Materials	Cross-section area	$P_{max}/\Delta T$	Power density (P_A)	Γ_p (μWcm^{-2}K^{-2})	Source
Commercial TEGs					
TGPR-22 W-7 V-56 S	5.6 × 5.6 cm^2	21.7 W	0.69 W cm^{-2}	—	[29]
HZ-2	2.9 × 2.9 cm^2	2.25 W/200 K	0.267 W cm^{-2}	6.69	[29, 106]
TGM-127-1,9-0,8	3.0 × 3.0 cm^2	5.1 W/170 K	0.57 W cm^{-2}	19.61	[29, 107]
TG12-2.5 (II–VI MARLOW)	3.0 × 3.0 cm^2	0.41 W/180 K	0.045 W cm^{-2}	1.4	[108]
Heavy metal chalcogenides: μ-TEGs					
Bi_2Te_3-Sb_2Te_3	0.5–25 cm^2	2.8 mW	—	83.8	[109]
Bi_2Te_3-Sb_2Te_3	0.325 cm^2	2.99 mW/52.5 K	9.2 mW cm^{-2}	3.3	[110]
Bi_2Te_3/Cu, Cu annealed	1.04 cm^2	2.34 mW	2.434 mW cm^{-2}	1.63	[111]
CMOS-based fabrication technology: μ-TEGs					
Si NWs/SOG	50 × 50 (μm)^2	29.3 μW/56 K	—	—	[112]
Si	—	0.41	—	0.48	[42]
Si NWs	5 ×5 mm^2 (TEG)	1.5 nW/0.12 K	—	—	[113]
Si NWs blades	—	–/5 K	12 μW cm^{-2}	0.48	[103]
Poly-Si(SiGe) quantum well-like str.	60 × 4 (μm)^2	–/20 K	—	0.251	[114]
Poly Si	3 ×3 mm^2	—	—	0.252	[115]
Si blades	48 × 36 (μm)^2	0.60 μW/33.9 K	∼35.0 mW cm^{-2}	29.0	[69]
Si(0.97)Ge(0.03)	48 × 36 (μm)^2	0.38 μW/16.1 K	∼22.0 mW cm^{-2}	84.0	[43]
Si(0.98)Ge(0.02)	48 × 36 (μm)^2	—	—	78.0	[43]
Si(0.99)Ge(0.01)	48 × 36 (μm)^2	—	—	52.0	[43]
Si(1.00)Ge(0.00)	48 × 36 (μm)^2	—	—	25.	[43]
MEMS-based fabrication technology: μ-TEGs					
Si NWs	2.0 mm^2(*)	832.0 nW	41.6 μW cm^{-2}	—	[102]
SiGe NWs	2.0 mm^2	900.0 nW	45.2 μW cm^{-2}	—	[102]
Si microbeam	2.0 mm^2	690.0 nW	34.5 μW cm^{-2}	—	[102]
SiGe Nw	2.0 mm^2	142.0 nW/14.3 K	7.1 μW cm^{-2}	0.034	[116]
Silicon membrane	0.25 mm^2	11.25 nW/5.5 K	4.5 μW cm^{-2}	0.149	[101]
Polymer-based flexible TEGs					
Organic: poly[Cu_x(Cu-ett)]: p-type + poly[Na_x(Ni-ett)]: n-type	26.7 mm^2	750.0 μW/82 K	2.8 μW cm^{-2}	4.16 × 10^{-4}	[117
Organic-inorganic hybrid	0.2 mm^2	335.0 nW/20 K	1.68 W m^{-2}	4.0 × 10^{-4}	[118]

Note: (*)active device area.

high power density [101] (∼7.1 μW cm^{-2}) and was further improved (to 45.5 μW cm^{-2}) by integrating a heat exchanger [102]. Similarly, power densities as high as 41.2 and 34.5 μW cm^{-2} were obtained by using μ-TEGs based on Si nanowires and Si microbeams [102], respectively (see table 1 for comparison). Therefore, these planar devices show full technological potential for powering low-power IoT-based WSNs].

On the other hand, specific power generation capacity (Γ_P) as high as 29 μW cm^{-2} K^{-2} (estimated $P_A = 0.034$ W cm^{-2}) has been achieved recently at room temperature in nanostructured silicon thermopiles by using silicon complementary metal-oxide-semiconductor (CMOS) technology, in a vertical device structure [69]. Using the same technology, a systematic increase in Γ_P from 25 to 84 μW cm^{-2} K^{-2} at room temperature was achieved in $Si_{1-x}Ge_x$ ($x = 0.0$, 0.01, 0.02, and 0.03) blades as shown in table 1. These Γ_Ps are comparable to the Bi-Te-based exotic μ-devices from the viewpoint of power output [103, 104]. This success is credited to the ability of the cost-effective CMOS technology that offers (a) a high-density integration of thermocouples, (b) low electrical and thermal contact resistances, and (c) the ability to tune electrical and thermal properties by controlling doped levels, the width of the thermopiles, and by engineering packing fraction [42, 69]. All these features make CMOS technology a more realistic technological solution for device

fabrication for powering IoT-based SNWs from ambient waste heat. Further tests of μ-TEGs based on silicon-NWs might provide interesting results as they are predicted to generate P_A in the range of $\sim$mW cm^{-2} with CMOS technology using miniaturization and integration [105].

2.1.3. Outlook

Focus on the cost-effective fabrication processes such as CMOS, MEMS technology, which allow fabrication of devices with small footprint area and high power output, is increasing. More attention must be paid to the design of heat from the hot to the cold end propagation in the micro-TEGs, as the large temperature gradients will result in larger power output. As the key compatible materials for such technologies are mainly Si and SiGe, therefore, the discovery of more silicon compatible materials is also necessary. Beyond the need to deploy novel technologies replacing the standard ones some factors must be considered that currently hamper a larger utilization of thermal energy harvesters: (a) improvement in materials (b) circuits consumption with extremely low power (c) TEG often requires additional power-conditioning electronics to be integrated with the harvesters, and (d) the cost factor should be minimized. Finally, TEGs are perhaps the best alternative when the use of other energy harvesting technologies is impractical.

2.2. Piezoelectric energy harvester

Piezoelectric energy harvesters (PEH) convert mechanical vibrations into electrical energy using piezoelectric materials. PEH is a crucial technology for self-power sources of unattended electronics, WSN, and biomedical and wearable devices. Detailed literature about PEH has been released in the last decade [119–124]. Here, we focus on the fundamental working mechanisms of PEH, the key parameters of mainly used piezoelectric materials, and the design principle, given by their technological potential in the IoT field.

PEH is based on the direct piezoelectric effect, where piezoelectric materials generate electrical energy when under external stress. The effect is described by the constitutive equations [119]:

$$D_i = \varepsilon_{ij}^{S} S_j + d_{ij}\sigma_j\,, \tag{2}$$

where vector D and E are the electrical displacements, d_{ij} is the piezoelectric constant, S_j and σ_j are the mechanical strain and stress, ε_{ij}^{S} is dielectric constant under constant strain. For the converse piezoelectric effect, an electrical stimulus is converted into strain in the materials. With a similar equation:

$$S_j = c_{ij}^{E}\sigma_j + d_{ij}E_i, \tag{3}$$

where c_{ij}^{E} is mechanical stiffness under a constant electrical field.

For an efficient PEH, piezoelectric materials require a large electromechanical coupling factor (k), piezoelectric constant d. Notably, the k characterizes the mechanical–electrical energy conversion efficiency. For the transversal and longitudinal effects, e.g. the 31- and 33-mode, it follows [122]:

$$k_{ij}^2 = \frac{W_{\text{electrical}}}{W_{\text{mechanical}}} = \frac{e_{ij}^2}{\varepsilon_{ij}^{T} c_{pq}^{E}} = \frac{e_{ij}^2}{\varepsilon_{ij}^{S} c_{pq}^{E} + e_{iq}^2}, \tag{4}$$

where Y is Young's modulus, e_{ij} is the piezoelectric constant. ε_{ij}^{T} is dielectric constant under constant stress. For ambient mechanical vibrations, the piezoelectric energy harvester generally operates at much lower frequencies than the mechanical resonance of the materials. In such a case, the PEH operates in off-resonance conditions and the piezoelectric element can thus be approximated as a parallel plate capacitor, where the electric energy is given as $U = 1/2CV^2$, or by the energy per unit volume [125]:

$$u = \frac{1}{2}\,(d \times g)\,(F/A)^2, \tag{5}$$

where C is the capacitance, V is the output voltage, F is the applied force, g is the piezoelectric voltage constant ($=d/\varepsilon_0\varepsilon_r$), and A is the area. The product of d and g ($d \times g$) is the so-called FOM. With a given area and thickness under the same driving force, piezoelectric materials with a large FOM provide more power.

However, to maximize the mechanical harvesting, resonant devices are the choice. For maximum harvested electrical power in resonant conditions with high efficiency (η), want piezoelectric with high k and high mechanical quality factor Q_m:

$$A = \frac{\left(\frac{1}{2}\right)\frac{k^2}{1-k^2}}{\frac{1}{Q_m} + \frac{1}{2}\frac{k^2}{1-k^2}}, \tag{6}$$

where $Q_m = F_r/\text{BW}$, characterizes the sharpness of the piezoelectric's electromechanical response spectrum. BW is the bandwidth, denoting the frequency span around the resonance frequency (F_r). A high Q_m is important for resonant devices to avoid losses to heat and problems with self-heating.

Table 2. The piezoelectric and electromechanical properties of typical piezoelectric materials.

Material	Material type	k_{31}/k_{33}	d_{31}/d_{33} (pC/N)	g_{31}/g_{33} (10^{-3}Vm/N)	FOM (x10^{-12})	Y (Gpa)	Reference
PVDF	Polymer	0.11/0.15–0.25	−23/33	−216/330	10.89	∼3.0	[123, 139]
PMN-PT	Single crystal	0.76/0.94	−1283/2365	−21.22/39.11	92.49	16.5	[139, 140]
PZN-PT	Single crystal	0.50/0.90	−970/2000	−21.0/44	88.00	8.2	[141, 142]
PZT-5H	Ceramic	0.39/0.75	−274/593	−9.11/19.7	11.68	55	[139, 143]
KNN	Single crystal	0.646*/0.827	−77/162	−32.6/68.5	11.10	—	[144]
BTO	Ceramic	24.4/53.9	−92.3/205	−5.8/12.3	2.52	—	[145]

2.2.1. Materials

Piezoelectric materials for PEH can be both inorganic and organic. Among the inorganic materials, ferroelectric materials are often the best choice as they have high FOM and their properties are tunable by both composition and microstructure. Some high-performing materials are lead-based materials such as $PrZr_xTi_{1-x}$ (PZT), $Pb(Mg_{1/3}Nb_{2/3})O_3$ (PMN). However, lead is toxic and is restricted to be used due to environmental concern. Among various lead-free ferroelectrics, $BaTiO_3$ (BTO), $K_xNa_{1-x}NbO_3$ (KNN), and solid solution of BTO with relaxor $(Na_{1/2}Bi_{1/2})TiO_3$ (NBT) show promising piezoelectric properties and attracting increasing interest in recent years.

In recent years, nanostructuring, doping, and defect chemistry are very effective strategies to boost the properties and performances of the piezoelectric material [126–128]. For ferroelectric, for instance, structuring of nano-domains can lead to superior properties with piezoelectric coefficients above 1000 pC N^{-1} [126]. Atomistic mechanisms causing such changes are not completely clarified and new tools in materials combinatorial screening, design, and simulation can be of great relevance in the coming years [129–131]. The role of interface and nanoscale also introduced new possible criteria for an extremely miniaturized system that requires high energy density [132–134].

For organic materials, phase polyvinylidene fluoride (PVDF) is one of the most common choices due to its overall performance. Polymeric materials are softer than ceramic piezoelectric (lower Y), and they have a negative strain with the electric field. Many efforts have been spent in the last decade to fabricate hybrid materials with synergic performances between mechanical flexibility, and easy processing of the polymers, with high piezoelectric performances of inorganic materials [135, 136]. However, such an integration is not always trivial as it requires novel methodologies and chemical methods to interface different materials efficiently. Recent advances in the field of nano-generators, however, indicate that novel heterostructures and carbon-metal oxide piezoelectric can achieve impressive results [137, 138]. Table 2, summaries such parameters for typical piezoelectric materials. Compare with inorganic piezoelectrics, organic materials such as PVDF has lower k and d values. However, the FOM value is comparable to PZT-based ceramics due to its large g value. Remarkably, PMN-PT and PZN-PT single crystals show much higher FOM compared with other materials.

2.2.2. Devices

Besides the selection of the material, the specific design of the PEH depends on its application requirement, such as the dimension limits, the mechanical energy source, the operating frequency, etc. Typical applications for WSN lay in the mW power generations [153]. However, the general trend is to reduce the power consumption of the sensor and communication systems, and PEH is the nW power generation, i.e. nano-generators, conveys a large variety of designs and solutions.

For the micro-power, extensive works have been carried out to improve the design of micrometric PEH in MEMS. Typical structures for silicon-based MEMS use a cantilever configuration with unimorph, bimorph, and a proof mass attached to the free end of the cantilever. The mass is used for tuning the resonance in the low-frequency range (<kHz) [146]. To amply the effective piezoelectric strain of the piezoelectric materials, the cymbal structure with metal end caps is designed. However, the resonance frequency of this configuration is very high, and a high mechanical source is needed to activate the PEH with this configuration [147]. Another approach is the multilayer design, which stacks piezoelectric layers together to enhance the output [148]. In particular, Xu *et al* [149] designed a new structure, which combined the cantilever and cymbal structures. This configure uses the bending motion of the cantilever to compress the two cymbals to generate electrical energy. Therefore, the resonance frequency decreases effectively, making it suitable for low-frequency applications.

In recent years, hybrid energy harvesters (HEH), merging piezoelectric harvesting with other mechanical harvesting technologies, are attracting increasing research interest. An example of HEH combining piezoelectric and electromagnetic energy harvesting approaches is designed by Li *et al* [150] The authors

Table 3. Comparison of various piezoelectric energy harvesting devices. The main properties are characterized by the dimensions of the devices, power (U), output voltage (V), loading resistance (R), and operating frequency (f).

Material	Configuration	Dimension	U	R	V	f	Reference
PZT-5A ceramics	Cantilever	1 mm^3	375 μW	200–300 kΩ	69.8 V	120 Hz	[146]
PMN-PT single crystal	Cymbal	≈30 ×5 mm^2	14 mW	74 kΩ	45.7 V	500 Hz	[147]
Polypropylene (IXPP)	Stacked or/and folded IXPP Piezoelectret films	20 × 20 mm^2	82 μW	93 MΩ	—	400 Hz	[148]
PMN-PT single crystal	Cantilever + Cymbal	≈35 × 5 × 8 mm^3	3.7 mW	251 kΩ	38 V	102 Hz	[149]
PZT ceramics	Piezoelectriccantilever + electromagnetic coil	≈60 × 15 × 40 mm^3	3.0 mW	170 kΩ/24 kΩ[a]	—	73 Hz	[150]
PVDF	Hybrid cell/multilayered planar structure	63.5 cm^2	0.95 mW	140 MΩ	—	4.4 Hz	[151]
PZT ceramics	Piezoelectric bimorphs	47 × 20 × 0.5 mm^3	613 μW	20 kΩ	13 V	20 r min^{-1}	[152]

[a] For piezoelectric and electromagnetic load, respectively.

found that enhancing the coupling between the piezoelectric and electromagnetic coupling not only improves the power and power spectral density but also broadens the frequency range to capture random vibrations. However, the electromagnetic system can interfere with electronics and is generally avoided in IoT applications. Alternatively, Zi *et al* [151] designed a triboelectric-pyroelectric-piezoelectric hybrid cell composed of a sliding mode (TENG) and a pyroelectric-piezoelectric nanogenerator for hybrid energy harvesting. At a sliding frequency of 4.4 Hz, the TENG alone generates a power density of 0.15 W m^{-2}. Using the mechanical energy and friction-induced heat on the TENG, the hybrid device gives rise to a power density two times that generated by TENG alone. With a small load resistance of 1 kΩ, the energy efficiency could reach up to 26.2% with the potential to be further improved with proper operations or power management. Another promising application area of PEH is to capture the energy from fluid flow (e.g. wind, tide, etc). For example, Yang *et al* [152] designed a rotational piezoelectric wind energy harvester using impact-induced resonance. The optimal DC output power reaches 613 μW across the 20 kΩ resistors at a rotation speed of 200 r min^{-1}. This kind of PEH is suitable for environments that are lacking vibrational energy but are rich in fluid flow (e.g. wind, water, etc). Table 3 summarizes the main properties of various piezoelectric energy harvesting devices.

In the field of nano generations, a wide variety of sensors are based on nano-tube, graphene, etc. For tribological energy, fluid flow, etc, many include biocompatible and integration on implantable and wearable flexible electronics. Although the power of such devices is currently too low, more efficient generation and reduced consumption of sensor and communication devices can be the next frontier for the IoT.

2.2.3. Summary and outlook

In summary, PEH are of particular interest as autonomous power sources. To further improve the overall performance, future works can be carried out via three different approaches:

- Optimize the electromechanical properties of the piezoelectric materials. Except for k, $d(e)$, other parameters are also relevant, such as mechanical quality factor Q, dielectric loss; the development of PEH based on lead-free piezoelectric materials, which is desirable for biomedical applications; the development of flexible piezoelectric materials, etc;
- Use of non-toxic materials. The most used piezoelectric materials currently in use are lead-based. However, new regulations in the act limit or even ban their use in future technologies. New materials with enhanced properties are thus needed and demonstrated for IoT applications, especially for those devices that are meant to be spread in the environment or in contact with the human body.
- The use of nanostructured and materials discovery initiatives would allow to further improve the performance of piezoelectric materials, and expand their application field, e.g. in the high-temperature range, where they are currently only a few compositions are in play.
- The design of PEH with novel configurations to tune the resonance frequencies for specific applications, broaden the bandwidth, the energy conversion efficiency;
- Improve the matching circuit and impedances of the electrical devices to reduce the electrical energy loss during transportation and storage.

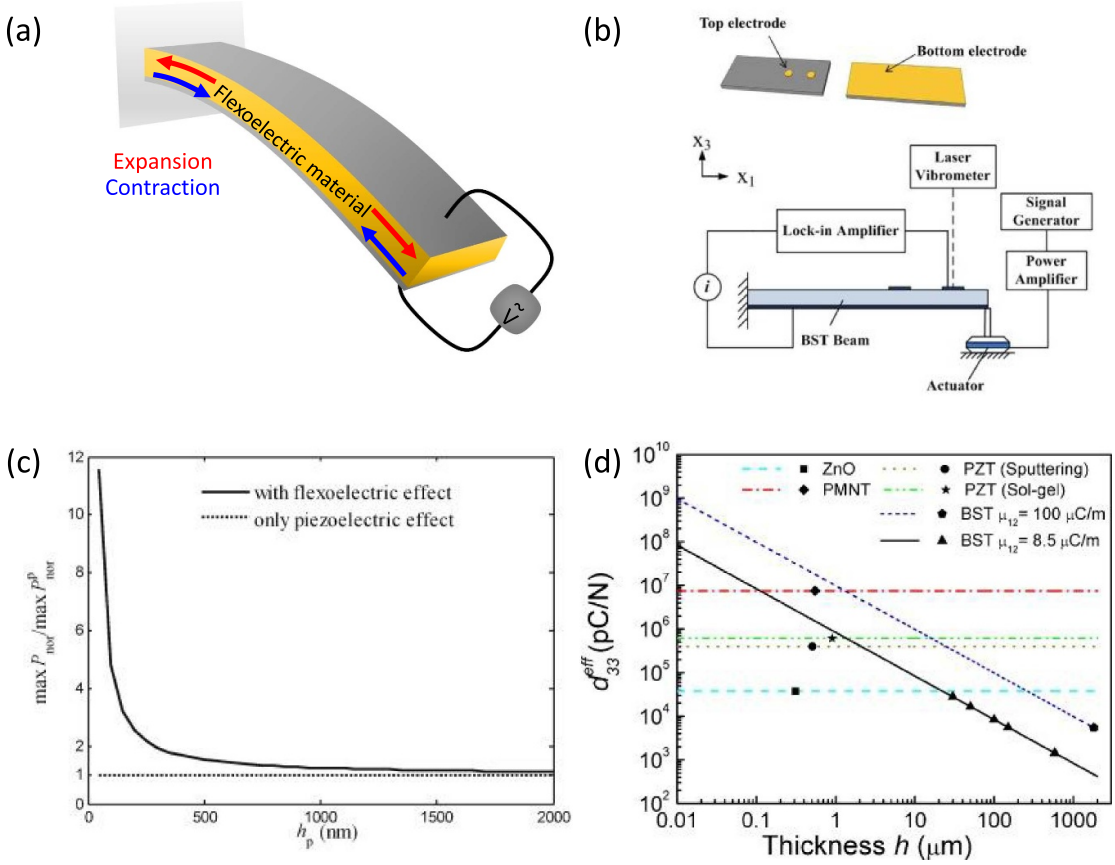

Figure 3. (a) Cantilever-type flexoelectric actuators. (b) Experimental setup for d_{33}^{eff} measurements led by flexoelectric effect in a cantilever beam [165]. (c) Energy conversion efficiencies with and without flexoelectric effect depending on the film thickness [164]. Reprinted from [164], Copyright (2018), with permission from Elsevier. (d) Thickness dependent d_{33}^{eff} for the configuration shown in (b) with the values of piezoelectric devices. Here, the thickness is decreased while simultaneously keeping the ratio between cantilever length and thickness fixed at 50 [165]. (c), (d) [165] John Wiley & Sons. Copyright © 2011 WILEY-VCH Verlag GmbH & Co. KGaA, Weinheim.

2.3. Flexoelectricity for IoT applications

Piezoelectricity is traditionally used for converting kinetic energy into electricity in IoT devices., as the devices shrink and the active materials for harvesting reach the nanoscale, electromechanical conversion due to flexoelectricity can be comparable to or even more efficient than that from piezoelectricity. Flexoelectricity manifests itself as an electromechanical coupling between a strain gradient ($\partial\varepsilon_{kl}/\partial x_j$) and induced electrical polarization (P_i):

$$P_i = \mu_{ijkl}\frac{\partial \varepsilon_{kl}}{\partial x_j}, \tag{7}$$

where μ_{ijkl} denotes the flexoelectric coefficient [154, 155]. In analogy with piezoelectric energy conversion, where strain causes a change in polarization and induces a current between two electrodes as an attempt to screen the polarization, flexoelectric energy harvesters use strain gradients to induce polarization and current. Since flexoelectricity is a universal phenomenon exhibited in all-dielectric materials, the range of available materials for flexoelectric devices is much wider than that of piezoelectric devices, which is allowed only in 21 symmetry point groups. Consequently, not only harmful lead-composite materials can be avoided, but also extreme operating temperatures are possible due to the lack of Curie temperature [156]. Furthermore, flexoelectric devices do not need an elastic passive layer to be bent [157] (figures 3(a) and (b)), and do not suffer from the hysteretic nature of the spontaneous polarization that can induce a dramatic performance reduction and irreproducibility.

As shown in equation (7), flexoelectric polarization is directly proportional to the flexoelectric coefficient and strain gradient. Since the strain gradient scales inversely with the dimension of the material, the flexoelectric effect can dominate at the nanoscale where large values of the strain gradients up to $\sim 10^6$–10^8 m^{-1} can be achieved [158]. In this range of high strain gradients, unusual flexoelectric phenomena such as polarization enhancements [159, 160], flexoelectric field effects on electronic conduction [161, 162], and enhanced electromechanics [163] have been reported. In the same way, the

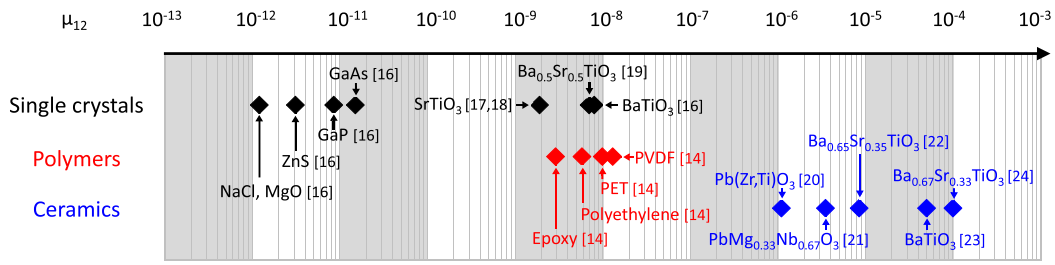

Figure 4. Flexoelectric coefficients of polymers, ceramics, and single crystals.

electromechanical properties of flexoelectric devices, such as energy conversion efficiency from mechanical energy to electrical energy, are highly enhanced at the nanoscale [164] (figure 3(c)). In several studies on flexoelectric cantilever devices, the effective piezoelectric coefficient (d_{33}^{eff}) has been considered to characterize the electromechanical properties of the flexoelectric cantilevers, which is defined as the generated flexoelectric charge per unit area by an applied normal force. The expression is

$$d_{33}^{eff} = \frac{6\mu_{3311}l^2}{Et^3}, \tag{8}$$

where μ_{3311} ($=\mu_{12}$ in a cubic symmetry, which is expressed in Voigt notation) is the transverse flexoelectric coefficient, l is the cantilever length, t is the cantilever thickness, and E is Young's modulus [165, 166]. Since d_{33}^{eff} is inversely proportional to the cube of the cantilever thickness, the electromechanical performance is significantly enhanced when the thickness decreases. The value of d_{33}^{eff} can be experimentally obtained by measuring the induced current flowing between a bottom and top electrode to screen the polarization in a vibrating flexoelectric cantilever [165] (figure 3(b)). Based on the measured d_{33}^{eff} values in a $Ba_{0.65}Sr_{0.35}TiO_3$ cantilever, the electromechanical performance in a few nanometer thick cantilever is expected to exceed that of piezoelectric ones by up to two orders of magnitude, as evident from figure 3(d) where the thickness is decreased while keeping $l/t = 50$ fixed [165].

2.3.1. Materials

Since d_{33}^{eff} is directly proportional to μ_{3311}/E, materials with a high flexoelectric coefficient or low Young's modulus are favorable for flexoelectric energy harvesting. Accordingly, soft polymers and oxides with high flexoelectric coefficients are promising candidates for flexoelectric devices. Polymers such as polyethylene, epoxy, and polyvinylidene typically have elastic moduli two orders of magnitude lower than ceramics, which could induce considerable enhancement in d_{33}^{eff} [167, 168]. However, to date, the flexoelectric coefficients of polymers ($\sim 10^{-9}$–10^{-8} Cm^{-1}) are in general 2–5 orders lower than those of ceramics ($\sim 10^{-6}$–10^{-4} Cm^{-1}) [165, 167, 169–175] (figure 4), although the large flexoelectric coefficient of α- PVDF ($\sim 10^{-5}$ Cm^{-1}) was reported, which is still controversial due to the discrepancy between the different authors with unclearness [167, 176–178]. Consequently, the flexoelectric coefficient and elastic modulus compensate each other, so the d_{33}^{eff} of polymers generally becomes smaller than for ceramics. Nonetheless, the stability of polymers under large deformations is better due to their softness, leading to a longer lifetime. The advantage of ceramics is the high flexoelectric coefficient, with for example μ_{3311} of paraelectric $Ba_{0.67}Sr_{0.33}TiO_3$ reaching $\sim 10^{-4}$ Cm^{-1} at room temperature, which is at least four orders higher than polymers and single crystals [175] (figure 4). In general, since the flexoelectric coefficient is proportional to the dielectric constant, materials such as (Ba,Sr)TiO_3, (Pb,Sr)TiO_3, and $Pb(Mg_{1/3}Nb_{2/3})O_3$-$PbTiO_3$ (PMN-PT) have very large flexoelectric coefficients near the ferroelectric-to-paraelectric phase transitions, which could be manipulated for flexoelectric devices (figure 4) [154, 175, 178].

2.3.2. Devices

Experiments using various designs of flexoelectric devices including cantilevers have been successfully executed as shown in figure 5 and table 4 [156, 157, 165, 179, 180]. In the ribbon-type PZT devices, the piezoelectric effect is increased by 70% in the curved region, which seems to come from the flexoelectric effect due to the strain gradient effect formed when the curved structure is stretched (figure 5(a)) [179]. Periodic stretching (8% strain) of the device consisting of ten PZT ribbons generates an electrical current of ~40 pA by converting mechanical energy into electrical energy. In another device with a dome-shaped ceramic wafer made of $Ba_{0.6}Sr_{0.4}TiO_3$, a finite d_{33}^{eff} exists above the Curie temperature due to the flexoelectric

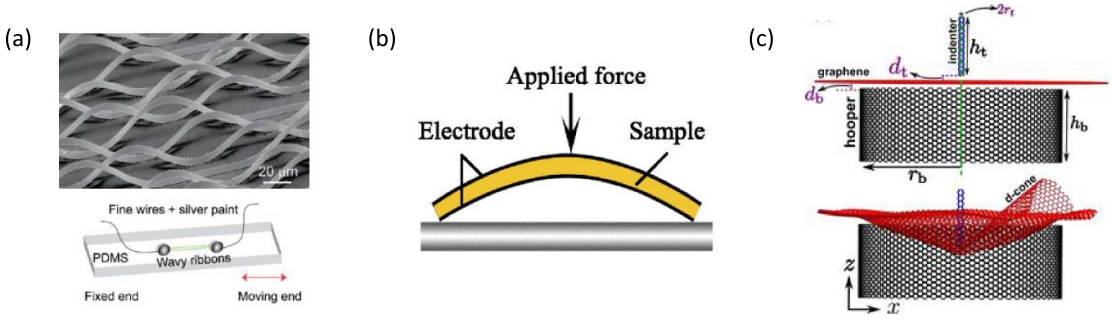

Figure 5. Flexoelectric devices. (a) PZT ribbons (upper) with a schematic (bottom) of the energy generation measurement by stretching [179]. Reprinted with permission from [179] Copyright (2011) American Chemical Society. (b) Dome-shaped $Ba_{0.6}Sr_{0.4}TiO_3$ wafer [156]. Reprinted from [156], with the permission of AIP Publishing. (c) Schematic of d-cone formation (bottom) in a PVDF foil [187]. Reprinted from[187], with the permission of AIP Publishing.

effect (figure 5(b)) [156, 181]. Using polymers, electrical energy can also be generated through flexoelectricity by a so-called d-cone formation in the wrinkle of a PVDF foil for wearable electronics (figure 5(c)) [180, 182].

Theoretical studies have also been performed to describe and optimize the electrical power analytically or numerically for the various designs of flexoelectric devices. In the cantilever design, induced electrical power is enhanced by 100% when both flexoelectricity and piezoelectricity are considered on nanometer scales compared to piezoelectricity alone [183]. It also has been reported that the output power of a cantilever depends on the residual surface effects such as surface elasticity, surface stress, and surface piezoelectricity [184]. The flexoelectric devices can be improved by considering a three-layered cantilever resulting in an energy conversion efficiency much larger than for single- or double-layered cantilever [185], or by attaching heavier masses at the end of the cantilevers arranged in an array to broaden the bandwidth of the resonance frequency [186]. It has also been investigated whether it is more convenient to connect the cantilevers in series or in parallel, which led to the conclusion that the induced power is largest for an array of cantilevers connected in series [186].

2.3.3. Outlook

Although the various experiments and theoretical analyses of flexoelectric devices have been studied, few papers report on experimental nanoscale devices [157, 188]. Among the reported results, the nanometer-thick $SrTiO_3$ cantilever is one of the most promising electromechanical devices for nanoscale flexoelectric energy harvesting [157]. In this device, not only the measured electromechanical performance is comparable to those of piezoelectric materials, but also its flexoelectric coefficient is maintained on the nanoscale with a similar value as in the bulk. This result is promising for making highly efficient flexoelectric devices from the recently developed freestanding membranes and cantilevers using oxide materials with thicknesses down to a single unit cell [157, 189]. In particular, a recent study reports an abnormally large flexoelectric polarization in the few-nanometer-thick epitaxial film with an extreme strain gradient value of $\sim 10^7$ m^{-1}. This phenomenon is expected to originate from the interplay between piezoelectricity and flexoelectricity in the highly curved film with the unusual Poisson's ratio distribution along the film-normal axis [190]. By combining nanofabrication technology with this polarization enhancement in the extreme deformation range, 2D-like flexoelectric energy harvesters could be a promising route for efficient power generators in IoT devices.

2.4. Electromagnetic vibration energy harvester for IoT applications

Almost all large-scale power generation today consists of turning mechanical energy into electrical energy through electromagnetic radiation. It is also possible to utilize this phenomenon to harvest power for IoT devices. In this case, the mechanical energy is usually provided as the vibration of the environment on which the IoT devices are mounted. There are two approaches to harvesting vibrational energy, namely piezoelectric, and electromagnetic energy harvester (EMEH). In this section, we consider the latter approach. A few comparisons of these two types of technologies exist, but a single study on wearable devices finds that the efficiency of piezoelectric generators is quite lower, as is their power density, compared to magnetic harvesters [193].

The core principle of an EMEH is that ambient vibrations cause a permanent magnet to vibrate through the coil, i.e. a time-varying magnetic flux density (φ_B) through the coil which results in an induced electromotive force as $\in = -(d\varphi_B/dt)$.

Table 4. Experimental and theoretical performances of flexoelectric devices (see table footnote[a]).

Technology	Device geometry	Active material	Energy source	Input	Energy production	Output	Conversion efficiency	Operation temperature	Remarks
Flexoelectricity	Cantilever	$SrTiO_3$	Elec.	Voltage	Mech.	Curvature/E-field = 3.33×10^6 V^{-1}	—	RT	Exp.[157]
Flexoelectricity	Cantilever	$Ba_{0.65}Sr_{0.35}TiO_3$	Mech.	Point force	Elec.	$d_{33}^{eff} = \sim 10^3$–10^4 pC/N	—	RT	Exp.[165]
Flexoelectricity Piezoelectricity	Buckled ribbons	PZT	Mech.	Stretch (8% strain)	Elec.	$I_{SC\ Max.} = \sim 40$ pA	—	RT	Exp.[179]
Flexoelectricity	Domed wafer	$Ba_{0.6}Sr_{0.4}TiO_3$	Mech.	Point force	Elec.	$d_{33}^{eff} = \sim 1$–24 pC/N	—	RT—200 °C	Exp.[156]
Piezoelectricity		$Na_{0.5}Bi_{0.5}TiO_3$-$BaTiO_3$				$d_{33}^{eff} = \sim 10$–24 pC/N		RT—400 °C	
Flexoelectricity Piezoelectricity	Crumpled foil	PVDF	Mech.	Point force	Elec.	$I_{SC\ Max.} = \sim 100$ nA $V_{OC\ Max.} = \sim 0.06$ V	—	RT	Exp.[180]
Flexoelectricity Piezoelectricity	Cantilever	PZT	Mech.	Vibration excitation	Elec.	Up to $\sim 1.8 \times 10^8$ W m^{-3}	—	RT	Theor.[184]
Flexoelectricity Piezoelectricity	Cantilever	PVDF	Mech.	Vibration excitation	Elec.	—	Up to ∼5%	RT	Theor.[185]
Flexoelectricity	Cantilever	$Ba_{0.6}Sr_{0.4}TiO_3$	Mech.	Vibration excitation	Elec.	>0.04 μW (90–110 Hz)	—	RT	Theor.[191]
Flexoelectricity	Cantilever	$Ba_{0.6}Sr_{0.4}TiO_3$	Mech.	Vibration excitation	Elec.	Up to ∼12.2 μW	—	RT	Theor.[192]
Flexoelectricity Piezoelectricity	Circular plate	PVDF	Mech.	Vibration excitation	Elec.	—	Up to 6.6%	RT	Theor.[164]
Flexoelectricity	Circular membrane	PVDF	Mech.	Vibration excitation	Elec.	Up to $\sim 8 \times 10^8$ W m^{-3}	Up to 11.93%	RT	Theor.[192]
Flexoelectricity	Ring	PVDF	Mech.	Vibration excitation	Elec.	Up to ∼50 μW	—	RT	Theor.[192]

[a] Elec.: Electrical energy, Mech.: Mechanical energy, d_{33}^{eff}: Effective piezoelectric coefficient, RT: Room temperature, $I_{SC\ Max.}$: Short circuit maximum current, $V_{OC\ Max.}$: Open circuit maximum voltage, Exp.: Experimental result, Theor.: Theoretical result.

Table 5. Power output from typical electromagnetic vibrational energy harvesting devices.

EMEH Motion	Category	Peak power density (μW cm^{-3})	References
1D	Single coil single magnet	7229	[194]
	Single coil multiple magnets	8015	[195]
	Multiple coils single magnet	1710	[196]
	Multiple coils multiple magnets	2800	[197]
2D	Multiple colis multiple magnets	788	[198]

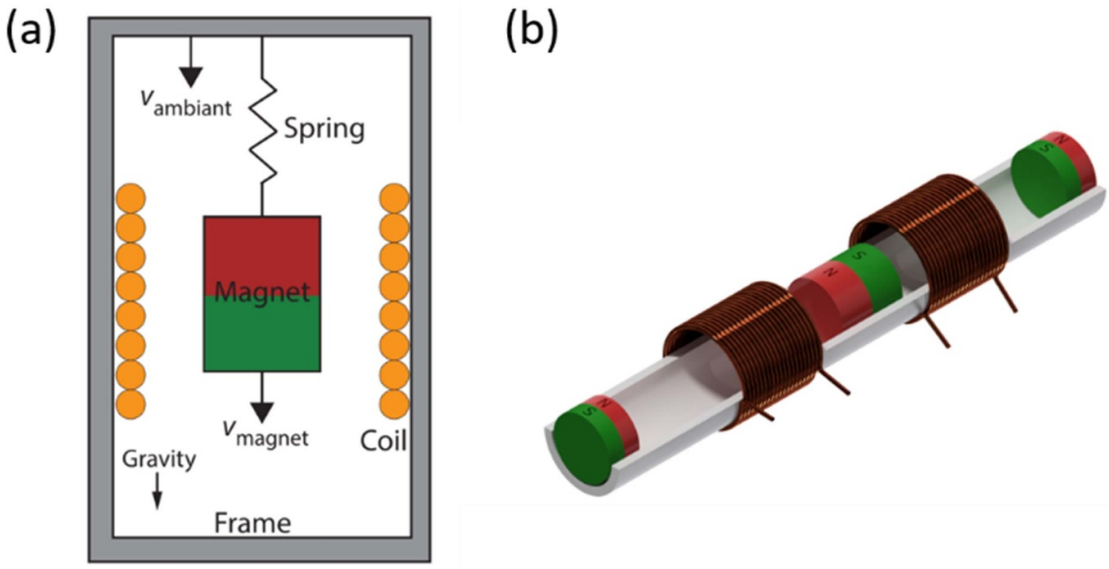

Figure 6. (a) Cross-section of a simple electromagnetic energy harvester consisting of a magnet that vibrates past a coil, caused by ambient vibration, and (b) basic schematics of a monostable electromagnetic energy harvester. The central magnet is levitated by the two fixed magnets at the end of the device.

2.4.1. Materials

To make EMEHs having as high power-density as possible, Neodymium Iron Boron or Samarium Cobalt magnets (also known as NdFeB and SmCo magnets respectively) are the most powerful type of permanent magnets commercially available today, with magnetic properties that are far exceed AlNiCo and ferrite magnet materials. While NdFeB magnets have a high-magnetic remanence and much higher coercivity than other permanent magnets, SmCo magnets rank similarly in strength, but they have much higher temperature stability. Both types have used manufacturing EMEHs with different power densities for four categories of one-dimensional harvesters and one category for two-dimensional motion as described in table 5.

2.4.2. Device

The simplest EMEH one can consider is a permanent magnet mounted on a spring and surrounded by a coil [199], as illustrated in figure 6(a). When ambient vibrations cause the spring to oscillate, the permanent magnet moves through the coil, causing a time-varying magnetic flux density and thus an induced electromotive force.

However, such magnets-on-a-spring devices can be plagued by mechanical friction, and also the wear and tear of the spring. Further, making these devices strong enough to act as harvesters for IoT devices would likely be problematic. Instead, the focus on electromagnetic energy harvesting has been on utilizing a configuration of permanent magnets that levitates a single permanent magnet with a spring-like restoring force. Such a device typically consists of three coaxial cylindrical permanent magnets, facing each other with polarities that make the middle magnet keep levitating, avoiding mechanical friction [196, 200, 201], as shown in figure 6(b). However, stable magnetic levitation is not possible as per Earnshaw's theorem, the permanent magnet must be enclosed in a cube, to prevent the middle magnet from flipping. We here term such configurations as mono-stable. When subjected to an ambient vibration the middle levitated magnet moves through one or more coils where an electromotive force is induced.

A substantial number of such EMEH mono-stable harvesters have been realized and tested. These can employ block or ring magnets, circular or rectangular containers, a different number of coil windings,

guidance for the middle magnet with or without spacers, and the spring on the top and/or the bottom edges to replace the fixed magnets [202]. These devices can also be classified according to e.g. their excitation and robustness [203]. A good physical description of the mono-stable EMEH devices exists, as the force on the levitated magnet can often be approximated with a spring-like force [201]. There is generally a very good agreement between modeling and experimental data for these devices [203], e.g. a mean absolute percentage error of 6% has been demonstrated [204]. Most current-state devices are in the centimeter range and produce a voltage in the mV–V range and power in the mW range [202], although this depends on the exact way that the device is operated as EMEH devices can have a quite complex phase space [205].

Besides the mono-stable EMEH design, several other designs have been considered. For example, in one approach, the coil is considered as the moving part instead of the permanent magnet [206]. In this case, the magnetic flux is enhanced due to a steel frame, but a couple of stoppers are needed at the edges of the harvesters. Likewise, attaching a coil winding to a rod that is exposed to ambient vibrations and vibrating this through a double concentric Halbach array magnetic structure can also be used to harvest power [207]. It is also possible to modify the one-directional movement of the free magnet in an EMEH to a multi-dimensional EH by making the fixed magnet similar to a doughnut-shaped container [208] and such devices have recently been shown to have a larger and more easily tunable harvesting bandwidth compared to monostable EMEHs [209, 210]. Finally, permanent magnets and springs can also be combined [211, 212] to specifically harvest power from very low-frequency vibrations.

Other electromagnetic harvesters: other electromagnetic energy harvesting designs than the levitated magnet design and the variants of this discussed above are also possible. One example is a harvester with a spring-less spherical permanent magnet with a non-uniform mass distribution, that generates a roly-poly-like motion in response to external vibrations, which induces a current in a coil [213]. Other designs use a joint about which the floating magnet in figure 6(b) rotates [214] or more chaotic movements using the random movement of a soft composite in a magnetic field with vibrations [215]. Moreover. Bi-stable prototypes have been also contemplated [216] so that moving restriction is attained in only one axis of the 3D space. The moving magnets keep levitating due to the repulsive force interaction with a set of permanent magnets around it. As a result, such EMEH can generate power from low frequencies and low g applications. Complex three-dimensional stable harvesters have also been studied [217], consisting of a set of lifting magnets, diamagnetic plates made of pyrolytic graphite, a floating magnet, and a couple of copper coils. This is also suitable for low frequency and low g applications. Finally, a design where the moving magnet does not depend on the repulsive force produced by a fixed magnet, but by a fluid has also been presented [218]. This EMEH employs a spherical magnet that rotates while fluid flows through the harvester.

2.4.3. Outlook

To be useful as energy harvesters for IoT applications, harvesters must typically be small e.g. about 1 cm^3 in size. This is a challenge for EMEHs, as these contain permanent magnets which have to be manually handled and positioned in the harvester and cannot be produced with e.g. lithography or other manufacturing techniques. However, microfabricating the coil in an EMEH is not challenging, and examples exist of harvesters where the common coil winding is replaced by a micro coil that can be fabricated on silicon or printed circuit boards [219], an example of such type of harvester can be seen in [220], where the micro-fabricated coil is placed on the bottom edge of the harvester. When the magnets are also miniaturized so that a miniaturized-sized device is produced, a few micro-watts of power can be generated when vibrated [221].

EMEHs have in the recent decade been shown to be able to produce a reasonable amount of power from the ambient vibrations, with power densities up to 8 mW cm^{-3} [195, 202], which is enough to supply energy to a sensor as it is detailed in the self-power monitoring system described in [210]. The technology is advantageous compared to other harvesting technologies because there is no wear on the device, the induction mechanism is simple and direct, and the device has low internal friction.

However, several issues must still be tackled with EMEH devices before these are fully ready to be commercialized. Besides the issue with miniaturization discussed above, further optimization of the design of the device, especially with a focus on multivariable performance optimization [198, 202] is necessary. Finally, ensuring a broader frequency harvesting range is likely needed for EMEH to be truly adaptable to the range of environments that IoT devices experience.

2.5. PV generators for IoT

PV convert light into electrical energy and is another promising way to power IoT devices [222–226]. IoT technology focuses mainly on indoor usages, where the spectra and intensities of light sources are quite different from the standard outdoor AM1.5G solar irradiation. In contrast to the AM1.5G solar spectrum,

which includes a significant portion of intensity in the infrared region, indoor light sources from fluorescent and light-emitting diodes (LEDs) have a spectrum with intensities primarily in the visible light range, from 350 to 700 nm, and with much weaker light intensities; the intensity from a ∼500 lux white light-emitting diode (WLED) is only roughly 0.15% of the AM1.5G 1 sun intensity [31, 227]. Consequently, conventional PV based on e.g. crystalline silicon, which possess a narrow indirect band gap of 1.12 eV and being optimized for outdoor use, do not perform well under indoor lightning due to a non-ideal match between the absorption spectrum of the materials, and the illumination spectrum of the indoor light sources. This results in significant thermalization losses, and from that too low photovoltages. This has recently driven research towards the use of new thin-film PV technologies based on wider band gap semiconductors for IoT applications.

The performance of a PV device is characterized by the power conversion efficiency (PCE), which is defined as the fraction of the electrical output power to that of the incident light power [228]: $PCE = \frac{J_{SC}V_{OC}FF}{P_{in}}$, where J_{SC}, V_{OC}, FF, and P_{in} are the short-circuit current density, open-circuit voltage, fill factor, and input light power, respectively. The numerator in equation (1) thus represents the electrical output power of the solar cell. As noted above, both the light spectrum and intensities for indoor and outdoor (sunlight) light sources are different, which is affecting the P_{in} parameter. Depending on the illuminance of the indoor light source, an output power of 10–100 μWcm^{-2} can typically be reached by indoor PV devices [222], which also means that a 10 cm^2 indoor PV device is large enough to power most wireless protocols used within IoT [7]. Further improvement of this requires optimization of materials and device architectures towards utilization under indoor light. Furthermore, such materials and architecture choices may affect not only efficiency but also the lifespan of the PV devices. An example of such considerations is for organic PV (OPV); for outdoor use, the PCE of OPV is slightly lacking behind that of silicon PV, which for indoor use is the opposite.

In terms of stability and lifespan, OPV still lacks behind silicon PV due to photo-degradation of organic molecules when exposed to light, heat, water, and oxygen [229]. In fact, the stability topic of organic photovoltaics (OPV) has been a large research field of its own for many years, also demonstrating the complexity of this topic due to the presence of multiple possible degradation routes. It is well known that photo-oxidation of organic molecules may take place under simultaneous exposure to oxygen and light [230, 231], something that can be partially mitigated via antioxidant additives [232, 233] and different encapsulation routes [234, 235]. The antioxidants are relevant as industrial processing always allows for inclusion of small amounts of oxygen in the cell during fabrication (done in air), which even the best encapsulant cannot protect against. Transport layer interface degradation is also well-known, in particular for many new non-fullerene based organic solar cell systems [236, 237], for example due to photocatalytic decomposition of these molecules at metal oxide interfaces. This has made studies on transport layer interfaces very relevant for the OPV field [238]. For indoor PV, however, these effects are much less of an issue due to the lack of harsh and alternating weather conditions, and in particular, the different light spectrum and intensity at indoor conditions, i.e. low light conditions and lack of UV component. Indeed, the photo-oxidation of OPV molecules is well-known to be wavelength dependent, and much more effective under UV light [239]. This leads to much more stable OPV devices at indoor conditions, which opens up for new routes for some emerging PV technologies within IoT applications.

2.5.1. Materials

The theoretical efficiency limit of a PV cell under a given incident illumination spectrum and intensity has been calculated for indoor light sources. For a single-junction solar cell with an optimum band gap lying between 1.82 and 1.96 eV, a theoretical PCE of higher than 50% can be reached [240], compared to the PCE limit of ∼33% under AM1.5 G solar irradiation using a semiconductor with a band gap of 1.34 eV [241]. The effect of the semiconductor band gap on the PCE can be seen when comparing crystalline and amorphous Si [242]. While crystalline Si solar cells only deliver a PCE of <10% under low-lux LED illumination, due to the low band gap of 1.12 eV, PV based on amorphous Si with a much wider band gap of ∼2 eV have demonstrated PCEs of >15% [242, 243]. Similarly, materials with band gaps that are normally not ideal for outdoor PVs can perform well under indoor lightning. For indoor OPV (1650 lux illumination) based on the polymer donor PM6 and the small molecule NFA Y6-O [244], an impressive PCE, of 30.9%, and an open-circuit voltage, V_{oc}, of 0.84 V has been recorded, mainly given by the strong light absorption between 400 and 800 nm for this material system. For indoor perovskite solar cells (iPsc), a PCE of 40% has been recently achieved for $(FAPbI_3)_{0.92}(MAPbBr_3)_{0.08}$ cells under 824 lux illumination [245]. Although many metal oxides are too wide band gap materials (above 3 eV), some binary and ternary oxide semiconductors exhibit strong optical absorption in the visible light range. For example, Cu_2O [246], α-Fe_2O_3 [247, 248], $Zn_{0.5}Mn_{0.5}O$ [249], and $Zn_{1-x}Cd_xO$ ($x = 0.4$–0.7) [250–253] all have band gaps in the range of 1.8–2.2 eV and thus may also be promising materials as light absorbers for indoor PVs to power IoT devices.

Table 6. Overview of recent works in perovskite solar cells (adapted from [222]).

Layer structure	Active-area (cm^2)	Irradiance (Lux)	Light type	PCE (%)	Voc (V)	Jsc ($\mu A\ cm^{-2}$)	FF (%)	References
Glass/ITO/SnO_2/$(MA_{0.91}FA_{0.09})Pb(I_{0.094}Br_{0.06})$/HTM/Au	0.2	1000	LED (5000 K)	38.2	0.96	188	78.7	[259]
Au/poly(3-hexylthiophene) (P_3HT)/Poly[(9,9-dioctyfluorenyl-2,7-diyl)-co-(4,4′-(N-(4s butylphenol) diphenylamine)(TFB)/$CsPbI_2$ Br/SnO_2/ITO/glass	0.1	1000	LED (6000 K)	27.16	0.94	122.0	0.77	[263]
Glass/ITO/SnO_2/$Cs_{0.05}(FA_{0.6}MA_{0.4})_{0.95}Pb(I_{0.6}Br_{0.4})_3$/PEAI/spiroOMeTAD/Au	0.2	1000	White LED (cool)	33.42	0.95	135	69.6	[264]
Glass/FTO/$cTiO_2$/$(FAPbI_3)_{0.97}(MAPbBr_3)_{0.03}$/spiroMeOTAD/Au	0.08	824.5	White LED (2700 K)	40.1	1	152	79.5	[245]
FTO/SnO_2/$Cs_{0.05}(FA_{0.85}MA_{0.15})_{0.95}$ PB$(I_{0.85}Br_{0.15})_3$/SpiroOMeTAD/M-oO_3/Ag	—	1000	LED	37.9	0.96	156	79	[262]
Glass/FTO/SnO_2/TiO_2/**$MAPbI_3$**/spiro-MeOTAD/Au	0.2	1000	LED	29.83	0.81	154.4	66.3	[265]
Glass/FTO/TiO_2/$CsPbBrI_2$:$(NH_4)C_2O_4$/PTAA/MoO_3/Ag	—	1000	FL	28.48	0.75	170	62	[266]
Glass/FTO/SnO_2-**PbO**/$MAPbI_3$/spiro-OMeTAD/Au	0.24	285	—	34.2	—	—	—	[267]
Glass/FTO/TiO_2/CsPbBrI2 $(NH_4)C_2O_4$/PTAA/MoO_3/Ag	—	1000	FL	28	0.75	170	62	[266]
Flexible glass/ITO/SnO_2/m-TiO_2/$CH_3NH_3PbI_3$/Spiro-OMETAD/Au	0.1	200	LED	20.6	0.82	30.7	72.2	[268]
ITO/SnO2/Pe/PEABr/Spiro/Au	—	1000	LED	42.1	1.10	5810	77.8	[269]
Glass/FTO/SnO_2/perovskite/spiro-OMeTAD/MoO3/Ag	—	1062	LED	31.9	0.92	0.150	77.1	[270]
CsPbI2Br:Pb(Ac)2/PM6	—	1000	LED	33.7	1.15	118	81.8	[271]

2.5.2. Devices

OPV have gained a lot of popularity due to their desirable properties, such as light-weight, mechanical flexibility, easy processability, and low-cost manufacturing, making them a cheaper alternative to the conventional Si-based solar cells. Owing to the switch from fullerene to non-fullerene acceptors (NFAs), the PCE of OPV has reached a record of 18.2% under 1 sun illumination (outdoor) [254], cutting it close to state-of-the-art Silicon-based PV, and above 30% under 1650 lux illumination (indoor) [244]. In contrast to fullerene acceptors, NFAs offer a larger degree of tunability in light absorption and also low voltage loss upon free charge carrier generation, which has been the main driver for this improvement. Besides their low environmental impact, OPVs are especially well-suited for indoor applications thanks to their large absorption coefficients, low leakage currents, and the tunable energy levels of organic semiconductors typically having band gap values well-suited for indoor lighting [255–257].

While the low light intensity generally causes lower open-circuit voltages for indoor applications, it also modifies the effect of charge recombination on device performance. Under low-intensity light, OPV has a higher susceptibility to leakage current and charge recombination caused by trap states, due to the overall lower charge carrier density [244, 256], which is in contrast to bimolecular recombination effects that are minor under these conditions [255]. These issues can be minimized by passivating defects and tuning the energy levels of the charge transport layers, to achieve a more desirable energy level alignment and form charge carrier selective contact layers, as well as by adjusting the energy levels of the organic active layer materials to increase the V_{oc} under low-intensity light [258]. Part of that is behind the success demonstrated recently for NFA OPV cells.

The integration of an unconventionally used copolymer has enabled the PCE of iPsc to reach the highest efficiency of Pb mixed halide iPsc of 38.2% [222, 259] under indoor 1000 lux. In tables 6 and 7, an overview of the most recent works on indoor perovskite and organic solar cells are summarized.

Table 7. Overview of recent works in organic solar cells.

Layer structure	Active area (cm^2)	Irradiance (Lux)	Light type	PCE (%)	Voc (V)	Jsc ($\mu A\ cm^{-2}$)	FF (%)	References
Glass/ITO/PEDOT/PM6:Y6-O/PDINO/Al	0.08	1650	LED (3000 K)	30.89	0.84	24.5	76	[244]
Glass/ITO/PEDOT:PSS/PM6:Y6-Y-Th2/PDI-NO/Al	0.00477	1000	LED	22.72	0.701	32.01	74.48	[272]
Glass/ITO/PEDOT:PSS/PBDB-TF:IO-4Cl/poly(PFN-Br)/Al	1	1000	LED (2700 K)	26.1	1.1	90.6	79.1	[273]
Glass/ITO/ZnO/PBDB-TSCl:IT-4 F/MoO_x/Ag	—	500	FL	21.53	0.63	60.44	76.29	[274]
PET/IMI/PEI/PC_{60}BM(443 nm)/PEDOt:PSS/Ag(Full Roll to Roll)	0.55	1000	LED	26	0.643	124	69.0	[275]
Glass/ITO/ZnO/D18:FCC-Cl/MoO_3/Ag	0.07	2000	LED (2600 K)	30.1	0.975	245.4	80.1	[276]
Glass/ITO/ZnO/PM6:FCC-Cl/MoO_3/Ag	0.07	2000	LED (2600 K)	28.5	0.914	244.1	81.2	[223]
ITO/ZnO/PFN-Br/PM6-BTP-BO-4Cl	0.04	1000	LED (3000)	20.20	0.67	104.82	73	[264]
ITP/ZnO/Polyethylenimine Ethoxylated/PBDB-T:M-ITIC-O-EH/MoO_x/Ag	0.1	1000	LED	21.6	678	163.9	69.8	[277]
PM6-BTP-BO-4CL	—	1000	LED	20.2	0.67	115.6	0.73	[278]
6K-PDMS/PEDOT/PSS	—	1500	LED	20.5	0.732	178.4	74.3	[279]
PBDB-TF:Y6-O	—	1650	LED	30.8	0.84	245	76	[244]

As mentioned above, the illumination intensities play an important role in the mechanisms governing the PCE of solar cells, such as current generation and recombination effects. Consequently, the PCE value is influenced according to the subjected illumination. Therefore, for further enhancement of PCE, the assessment of the traps associated with recombination mechanisms influencing the power efficiency must be considered both indoor and outdoor, especially under low light intensities, where the effect of these traps is prominent [222]. Attempting to mitigate the effects of trap-assisted recombination would require some treatments, for instance, the passivation of interface defects or the implementation of some additive to enhance their PCE [260]. Additionally, it was possible to fabricate a low-trap CsPbI2.7Br0.3 perovskite cell that performed superbly and outperformed c-Si cells in low-light conditions under illumination from a 1000 lux fluorescent lamp and a WLED, the optimized device attained PCE values of 32.69 and 33.11% [261]. Besides, doping by strong electron acceptor of the perovskite demonstrated a viable method for effective charge transport, opening the door to their use as IPVs. The ideal perovskite solar cell has achieved an outstanding indoor PCE with PCE values of 37.9% under 1000 lux low light and 21.3% under one sun illumination [262]. This emphasizes the importance of gauging the trap states experimentally in indoor PV technology, in addition to a standard comparison of the solar cell performance between indoor light sources.

2.5.3. Outlook

Compared to conventional outdoor solar cells, indoor PV is still in an early stage. The effects of lower light intensity and hence reduced photo-generated carrier concentrations should be more carefully studied for device optimizations [222]. Currently, a standard protocol for indoor light sources does not exist [226]. We emphasize the importance of establishing such a standard for reporting efficiencies of indoor PVs, such that a fair comparison can be made.

While OPVs and perovskites have demonstrated high PCE values of >30% under indoor light illuminations, stability issues remain although they are less significant under indoor conditions. Therefore, the commercialization of indoor OPV has also started recently. Furthermore, perovskite solar cell efficiencies at low light illuminations have rendered them to be promising for indoor application compared to other technologies. For both OPV and perovskite, the potential low cost is a further driver for commercialization. At present time, efforts to implement these photovoltaic technologies in indoor applications, and more specifically, to power IoT devices, are already yielding promising results. For example, iOPVs have successfully been used to supply smart temperature and humidity sensors using indoor-like illuminations as low as 300 lux [256].

3. Section-II: energy storage and on-demand powering devices

In this section, we present recent developments on energy storage and on-demand power devices used for IoT applications. The major focus of this section is devoted to battery technologies which represent the most mature and most common solution for microscale powering devices (section 3.1), while we additionally discuss micro-fuel-cell-based technologies as an alternative pathway for on-demand powering of IoT devices, which may complement battery technologies in applications where fast charging/fueling processes are needed.

3.1. Batteries for IoT applications

IoT devices with energy harvesting may work as independent devices without onboard energy storage [280]. Most of these micro-harvesters are based on intermittent energy sources, therefore, integration of rechargeable energy storage in IoT devices is of importance for continuous, long-term, and independent functionality, ensuring that the harvested energy does not go to waste. Combining energy harvesting and storage allows utilization of very low-power energy sources while still enabling higher energy use at a given time independently of the availability of the external energy source [280]. Integrating energy harvesting and storage may lead to efficient utilization of the harvested energy, e.g. by combining PV with a lithium-ion battery (LIB) [281, 282].

The requirements for IoT rechargeable batteries are very dependent on their size and use. For instance, flexible batteries could be of interest for IoT wearables [283, 284], high- or low-temperature performance would be a need for devices working in extreme environments and micro-batteries would be needed for very small IoT sensor devices. Generally, the characteristics of IoT on-board rechargeable batteries are e.g. size, reliability, low self-discharge, safety, and durability. The batteries should ideally be scalable with a tailor-made design and format so that the batteries are made to fit the device instead of having to design the device to fit a specific battery format.

All-solid-state thin-film lithium batteries (TFLBs) with outstanding safety and excellent integration ability are the best candidate so far to fulfill this purpose [285]. Similar to LIBs, TFLBs consist of cathode, electrolyte, anode, and collectors [286]. This section presents the state-of-the-art materials for cathode, anode, and electrolyte with different advantages and challenges. Then, some full cell assembly is presented with some commercial examples. TFLBs are highly customizable, which could support low-power IoT devices with a power consumption of between 10–1000 μW cm^{-2}. Higher energy density and longevity are what is been pursued in the development of TFLBs. TFLBs can be fabricated by various vacuum-based and wet-chemical methods. For physical vapor deposition (PVD) vacuum-based methods, there are magnetron sputtering and pulsed laser deposition (PLD); atomic layer deposition (ALD) is a common technique in terms of chemical vapor deposition vacuum-based methods. Sol-gel, spray pyrolysis, dip coating, and spin coating are examples techniques of wet-chemical methods [287]. A schematic of the cross-section of a TFLB is shown in figure 7. In this review, we are focusing on PVD methods, which have better integrations of micro on-chip devices.

3.1.1. Materials

3.1.1.1. Electrolyte

Many materials have been developed as solid electrolytes (SEs) including inorganic, organic, and inorganic/organic hybrid materials [289, 290]. For thin-film batteries produced by deposition methods, PLD, sputtering or ALD, inorganic materials are the most relevant SEs. LiPON, $Li_{3-x}PO_{4-y}N_z$, is a lithium phosphate-derived material, which has been used extensively as SEs in thin-film LIBs despite its rather low intrinsic lithium-ion conductivity [290], due to its good stability in air and against metallic lithium [291]. NASICON-type (structurally equivalent to $Na_{1+x}Zr_2P_{3-x}Si_xO_{12}$) materials e.g. $LiM_2(PO_4)_3$ (M=Zr, Ti, Hf, Ge or Sn) showed good lithium-ion conductivities [289], and partially substituted materials, e.g. $Li_{1.3}Al_{0.3}Ti_{1.7}(PO_4)_3$ (LATP), show even higher ion conductivity. The major issue of NASICON electrolytes is the interfacial instability both on cathode and anode [292]. Another perovskite-type material with a general formula of ABO_3 also has good Li-ion conductivity (10^{-4} S cm^{-1}). Lithium lanthanum titanate (LLTO) is one of the most promising perovskite electrolytes with a high ionic conductivity due to the vacancies in the A sites. Similar to LATP, the electrolyte/electrode interface of LLTO is thermodynamically unstable, resulting in increased resistance [293]. Garnet structure solid electrolyte (LLZO) is a promising material due to its high ionic conductivity and good chemical stability against metallic lithium. This outstanding stability is originated from the kinetic stabilization of the decomposition interphases [294]. However, it suffers from Li metal dendrites growth, due to the grain boundary originating from its polycrystalline structure [295]. The growth of this dendrite will eventually lead to a short-circuit, which hinders the use of Li metal as the anode material. Employment of single-crystal or amorphous LLZO could block the Li dendrite growth [295]. The

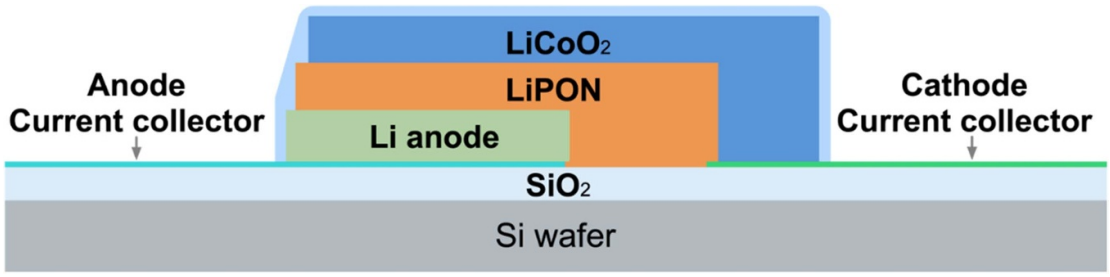

Figure 7. Schematic illustration of the cross-section of a TFLB [288].

ionic conductivity of thin-film LLZO is reported to be lower than that of bulk LLZO, due to the difficulty of depositing Li-containing thin films with sufficient crystallinity and density. This difficult crystallization of LLZO is caused by the volatilization of lithium at higher temperatures (both deposition and annealing) which results in unexpected stoichiometry [296]. More importantly, the higher surface-to-volume ratio of thin-film materials compared to bulk materials brings more severe Li loss [297]. Several sulfide-based SEs have been discovered with very high lithium-ion conductivity, especially related to $Li_{10}GeP_2S_{12}$ (LGPS). An example is $Li_{9.54}Si_{1.74}P_{1.44}S_{11.7}Cl_{0.3}$ (LSPS) [298], which has the highest room-temperature lithium ionic conductivity published so far. However, sulfide-based SEs such as LGPS and LSPS is not stable both mechanically and chemically against Li metal. They are also suffering from the toxic gas released when exposed to air [299].

3.1.1.2. Cathode

Current high-performance cathode materials used in thin-film micro-batteries are mostly lithium transition metal oxide materials. Due to the wider electrochemical window of SEs, some high-voltage cathode materials with promising specific capacities are readily available. $LiCoO_2$ (LCO) has an exceptionally high volumetric capacity (700 Wh l^{-1}) and relatively high gravimetric capacity [300]. The charging cut-off voltage of LCO is about 4.2 V, which gives a gravimetric capacity of about 140 mAh g^{-1}. Recently, the cut-off voltage had been pushed up to 4.55 V, which delivers a promising 190 mAh g^{-1} specific capacity [301]. High-voltage spinel $LiNi_{0.5}Mn_{1.5}O_4$ (LNMO) has been intensively studied [302, 303] and employed in TFLBs [302–305]. It can reach a high voltage of up to 4.7 V [306]. The specific capacity of PLD deposited LNMO is significantly lower than that of bulk LNMO, due to the difficulties of maintaining its ordered $P4_332$ structure at 700 °C, which is the normal temperature for PLD and sputtering [307]. Ni-rich layered oxide (NMC or NCA) is commercially used in electric vehicles, which is a promising high-capacity material with reduced Co content. The synthesis of thin-film Ni-rich material with good crystallinity is challenging. Only a few studies had reported Ni-rich TFLBs [308]. Li-rich layer-structured oxide (LRO) materials could reach a capacity of 275 mAh g^{-1} with a 4.9 V cutoff voltage, which is higher compared to other cathode materials discussed here [309]. However, the lithium loss during the deposition and annealing processes is still a challenge, especially at a higher temperature [310, 311]. The stoichiometry of LRO is also difficult to control using vacuum-based deposition methods [311]. Low initial Coulombic efficiency, and poor cycle and rate capability also hinder the implementation of LRO [312].

3.1.1.3. Anode

$Li_4Ti_5O_{12}$ (LTO) is a Li-insertion material that is widely employed as an anode material in TFLBs. The main advantage of LTO is that the volume exchange during charge/discharge is minimal (<1%), so-called zero-strain materials [313]. However, the low capacity (<175 mAh g^{-1}) and high voltage (1.55 V vs Li) make it less appealing compared with silicon (>3500 mAh g^{-1}) and lithium metal (3860 mAh g^{-1}) [314–316]. The high capacity and good lithography process compatibility of Si make it a promising candidate for on-chip TFLBs. The main challenge of Si used as an anode material is the large volume expansion (>400%) [317]. The large volume change may cause a structural failure which leads to a short lifespan. To relieve the effects of this drastic Si volume change, many 3D-structured silicon anodes have been designed [318, 319]. This high-aspect ratio of 3D Si anode could also increase the areal power density of TFLBs. Li metal anode has the highest gravimetric capacity among all anode materials. The utilization of Li metal anode could drastically increase the gravimetric capacity of Li batteries. However, the lithium dendrite/void formation during the discharge (plating)/charge (striping) process gives a critical current density which limits the high power application of Li metal anode [320]. Dendrite formation is less crucial for TFLBs when employing LiPON or amorphous LLZO as SEs, because these homogeneous defects free materials can completely prevent the dendrite penetration [295, 320], for instance, a study using LiPON as SE, ($LiNi_{0.5}Mn_{1.5}O_4$)LNMO as cathode

Table 8. Examples of commercial TFLBs.

Manufacturer	Model	Composition	Capacity (μAh)	Size (mm)	Weight (mg)	Cycle life	Operating temperatures
TDK Electronics AG	CeraCharge [326]	$Li_3V_2(PO_4)_3$/ $Li_{1.3}Al_{0.3}Ti_{1.7}(PO_4)_3$	100	4.4 × 3.0 × 1.1	40	—	−40 to +80 °C
Cymbet Corporation	EnerChip Bare Die CBC050 [327]	$LiCoO_2$/ LiPON/Li	50	5.7 × 6.1 × 0.2	—	>5 000 at 10% discharge	−40 to +70 °C
Front Edge Technology, Inc.	NanoEnergy [328]	$LiCoO_2$/ LiPON/Li	100–1,000	20 × 25 × (0.1–0.3)	—	<10% loss after 1 000 cycles	−40 to +100 °C
Infinite Power Solutions	Thinergy MEC225 [329]	$LiCoO_2$/ LiPON/Li	130	12.7 × 12.7 × 0.17	125	10 000	−40 to +85 °C
STMicroelectronics	EnFilm EFL700A39 [330]	$LiCoO_2$/ LiPON/Li	700	25.7 × 25.7 × 0.22	200	<20% loss after 4,000 cycles	−40 to +60 °C

and Li metal as anode had achieved a cycle life of 10 000 with 90% capacity retention [305]. Anode-free configuration can be seen as a special type of Li metal anode. As the name suggests, anode-free batteries do not have an anode when it is been manufactured. Its Li metal anode forms during the charging process. This could lower the manufacturing cost with improved safety [321]. An uneven lithium deposition (dendrite) is the major challenge of anode-free batteries, because the contact between the SE and current collector may be insufficient [322]. The large volume change of Si also plagues Li anode/anode-free TFLBs, as the entire active layer is consumed and redeposited during a discharge/charge cycle.

3.1.2. Devices

Although the first secondary TFLB was developed more than three decades ago [323], only a few TFLBs are commercially available. Table 8 lists some commercially available TFLBs. The capacities of these commercial TFLBs are highly flexible, varying from tens to thousands μAh, which corresponds to the power consumption of lower-power IoT devices with a typical energy demand of several microwatts (μWs) to a few milliwatts (mWs). The composition of these TFLBs is mostly $LiCoO_2$/LiPON/Li, which attributes to the high energy density of Li metal/$LiCoO_2$ and the chemical/mechanical stability of LiPON. Despite its low ionic conductivity, LiPON is still the mainstream of TFLBs, showing the lack of development of other SE materials (NASICON, perovskite, Garnet). Among these TFLBs, only the EnerChip Bare Die batteries from Cymbet Corporation are designed for implementation in embedded systems (can be placed directly on a PCB), which is manufactured on p-type silicon wafers. Others are implemented as surface-mounted devices in IoT devices. One example of the powering IoT devices using thin film batteries is radio-frequency identification (RFID) tags, which are used in shipping and inventory control. Some of the RFID tags include sensors that can act as IoT nodes, and these tags are so thin that regular methods are not applicable in such case [324].

Some examples of reported TFLBs are also discussed here, as shown in table 9. Again, the electrolyte material for those TFLBs is LiPON, and for anode material is Li metal. A recent study utilizing LLZO electrolyte has shown an increased areal and gravimetric capacity compared to LiPON electrolyte [325]. The capacity retention of a polycrystalline LLZO electrolyte TFLB is still far away from that of a TFLB with an amorphous LiPON electrolyte.

3.1.3. Outlook

Although there are already some TFLBs commercially available, their specific energy and energy density is orders of magnitude lower than conventional pouch/cylindrical cells. The energy density of the TFLBs listed in table 8 ranges from 3.7 to 30 Wh kg^{-1} (10–86 Wh l^{-1}). In comparison, an LG INR 18650 MJ1 cylindrical cell (3500 mAh) has an energy density of 257 Wh kg^{-1} (710 Wh l^{-1})[338]. Micro-batteries have lower energy density due to their lower active material/inactive material ratio. Nonetheless, the energy density of TFLBs still needs to be increased to improve the overall performance of micro- harvest/storage devices. In addition, the areal power capability of TFLBs is another limiting factor of their application to IoT devices. One method of increasing the areal power capability is replacing LiPON electrolyte with other SEs with a higher ionic conductivity, such as LLZO. This will need to solve the interfacial stability issue which could be challenging for both TFLBs and regular-sized batteries. A recent study realized an ultrathin amorphous

Table 9. Examples of reported TFLBs.

Year	Composition	Gravimetric capacity (mAh g^{-1})	Areal capcacity (μAh cm^{-2})	Thickness (μm)	Voltage (V)	Cycle life	Deposition	References
2000	LCO/LiPON/Li	137	—	15	3.0–4.2	<2% loss after 4,000 cycles	RF sputtering	[331]
2014	LNMO/LiPON/Li	122	—	3	3.5–5.1	10% loss after 10 000 cycles	RF sputtering	[305]
2018	LTO/LiPON/Li	162	2.7	—	1.0–2.0	<10% loss after 200 cycles	Flame aerosol	[332]
2019	LCO/LiPON/ Anode-free	110	5.7	ca. 9.7	2.0–4.2	<20% loss after 100 cycles	RF sputtering & aerosol	[333]
2020	LCO/Li-Nb-O/LLZO half-cell	142	20.9	0.5	3.0–4.25	>80% after 138 cycles	RF sputtering	[325]

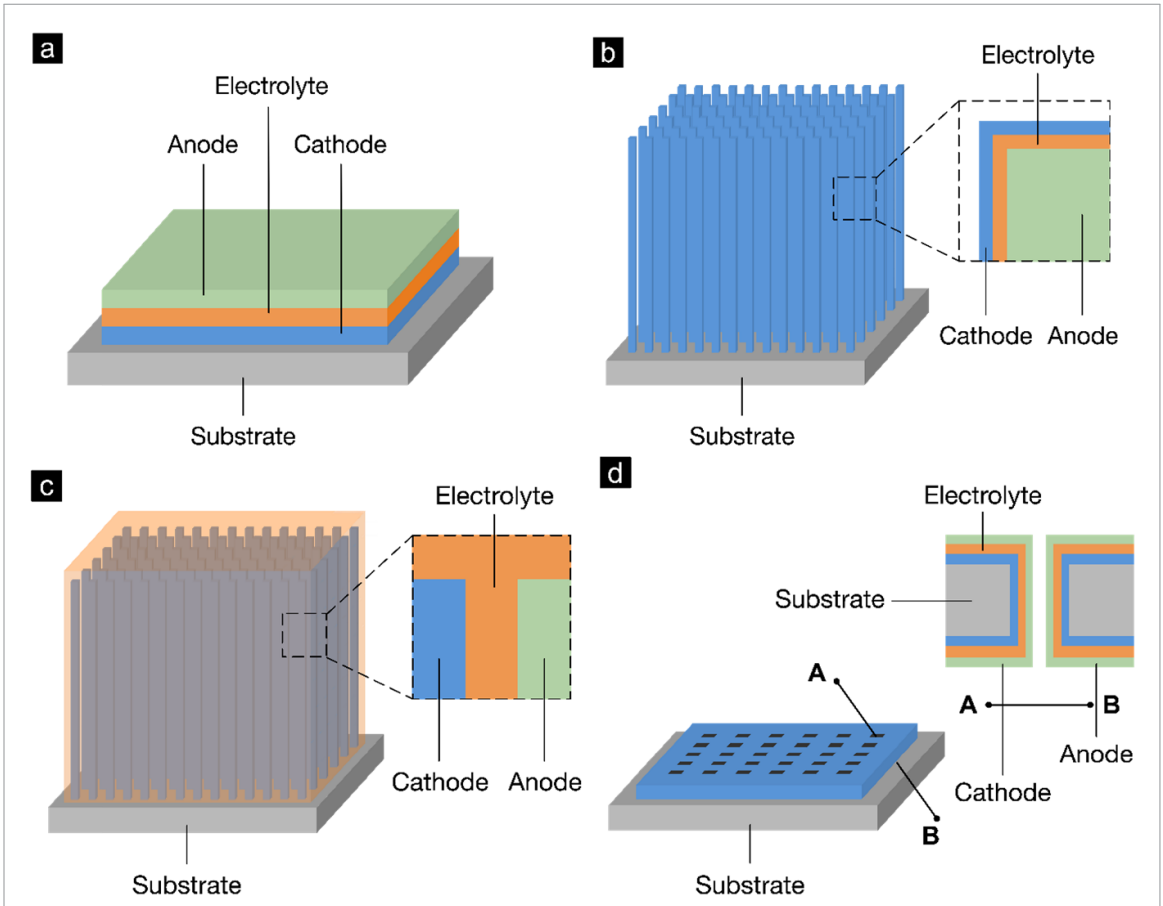

Figure 8. Illustration of TFLB architectures [305]. (a) 'Traditional' planar design. (b) 3D microbattery based on nanorods [334]. (c) 3D microbattery based on microchannels [335]. (4) 3D microbattery with interdigitated design [336]. Illustration and microscopic images of TFLB architectures [337].

LLZO electrolyte, which has shown its ability to block the growth of Li dendrite like LiPON thin films [295]. Another approach to improving the capacity and rate capability is to fabricate TFLBs with 3D architectures. Xia *et al* reported self-standing 3D cathodes for TFLBs with improved interface kinetics. They deposited 3D $LiMn_2O_4$ (LMO) nanowall arrays and planar LMO thin films on conductive substrates using magnetron sputtering. The 3D TFLB has shown a superior capacity and rate capability compared to the 2D TFLB with discharge capacities of 119 and 83 mAh g^{-1} at 2 and 20 C rates, in contrast to 87 and 16 mAh g^{-1} of the 2D TFLB. Figure 8 illustrated some TFLB designs with different 3D architectures.

3.2. Micro-fuel cells for on-demand powering of IoT devices

Batteries represent by far the most common energy storage and powering concept for IoT devices. However, recent developments in micro-fabrication of electrochemical cells, such as fuel cells and electrolyzers, enable

a new perspective on the integration of fuel cell technologies as powering device also in self-controlling or remote applications, providing a compensation of power limits and intermittency of direct energy harvesting. By definition, a fuel cell is neither an energy storage nor an energy harvesting device. However, when integrated with a fuel reservoir/storage they hold the potential to work as an on-demand powering device like a battery, and at the same time, may harvest excess energy to internally recover their fuel via electrolysis (in reverse mode). Microscaled fuel cells and electrolyzers may hence complement batteries as a sustainable on-demand powering device based on hydrogen technology. However, such device concepts typically rely on an active supply of a chemical fuel, limiting their operation to niche applications. For example, IoT applications that allow external access for recharging/refueling, but require fast charging times (e.g. a hearing aid as medical device [339]), can benefit from micro fuel cell technologies. Hydrogen-based fuel cells were also proposed as a competitive powering solution for different types of IoT systems [340] and also explored in current European initiatives such as Harvestore [10, 341, 342].

Fuel cell devices are based on the idea of converting chemical energy into electrical output by forcing complementary redox half-reactions and subsequent ion transport across a membrane. Electrochemical energy conversion typically reflects a reaction of hydrogen and oxygen in the overall fuel cell reaction, leaving behind water as the main reaction product. As a result, the ion transport required for fuel cell operation is either proton transport or oxygen ion transport. Typical fuels are gaseous hydrogen or methane. The basic operation of fuel cells is CO_2-emission-free, making its technology sustainable and in principle green. Miniaturization of fuel cells and particularly micro-scale solid oxide fuel cells may be considered a key ingredient for their potential application in remote IoT devices. The ability to structure and build fuel cells based on nano- to microscale thin films allows the compact design ($\sim$1 cm^3) of fuel cell devices that are compatible with the need of IoT devices.

3.2.1. Materials

In general, the two main types of micro fuel cells for portable application are micro proton-exchange membrane fuel cells (μPEM) and micro Solid oxide fuel cells (μSOFC). In μPEMs, the electrolyte is commonly a proton-conducting polymeric membrane that allows the exchange of ions between the oxidizing atmosphere at the cathode electrode and the gaseous fuel flowing through the anode electrode [343]. The high protonic conductivity of polymeric membranes such as Nafion® allows PEM to operate between ambient temperature and 90 °C, while their high humidity content prohibits the use above the water boiling point. This operational range permits a facile integration of μPEM into standard Si microfabrication techniques, as was demonstrated by different authors [344–347].

Another promising type of miniaturized power generator for portable application is micro Solid oxide fuel cells (μSOFCs) [348, 349]. μSOFCs are characterized by the use of an oxygen ion conducting metal oxide thin film as an electrolyte. While in traditional SOFC temperatures higher than 700 °C are needed to overcome the ohmic losses derived by the poor ionic transport, nanometric electrolyte thin films can drastically reduce the operating temperature of μSOFCs down to 400 °C, making them accessible to remote applications where waste heat is available in large amounts [350]. Research and development efforts toward nanoscale manipulation of ionic properties of materials principally allow realizing micro-scale membranes and exchange electrodes, building a fully operational fuel cell on the micrometer lengths scale. In addition to that, a vast variety of research is devoted to harvesting nanoscale materials science for improved fuel cell performance, including tailored nano-composite materials [351–353] and heterogeneously layered superlattices [354–358], or interface concepts with tailored ion conduction along and across interfaces [357, 359–361]. The interested reader is referred to Garbayo *et al* [362], Wen *et al* [363] and Shin *et al* [364] for more details on the strategies for improving the performances of electrode and electrolyte thin films for μSOFC.

3.2.2. Devices

Table 10 shows a collection of characteristics, operating conditions, and performances reported in the literature for different types of μSOFCs and μPEMs. For comparison, table 10 is also reported a selection of results obtained for proton-conducting μSOFCs (PE- μSOFCs), in which the electrolyte is based on a protonic conducting oxide thin film, and thin films based SOFC (TF-SOFC), where thin films components are integrated with a bulk anode supported fuel cells. To better visualize the large spreading of μSOFC performances, figure 9 shows the specific power density and total power reported in table 10. In the figure 9(b), the performances of μSOFCs are also divided into the three main substrates used, i.e. (a) Microfabricated Si substrates, (b) Porous Anodized Aluminum oxides (AAO) and (c) Porous Metallic substrates. μSOFCs reach very high values of power densities that place them among the most efficient micropower systems [348, 349]. Yet, the increase in power density is also observed to go along with a decrease

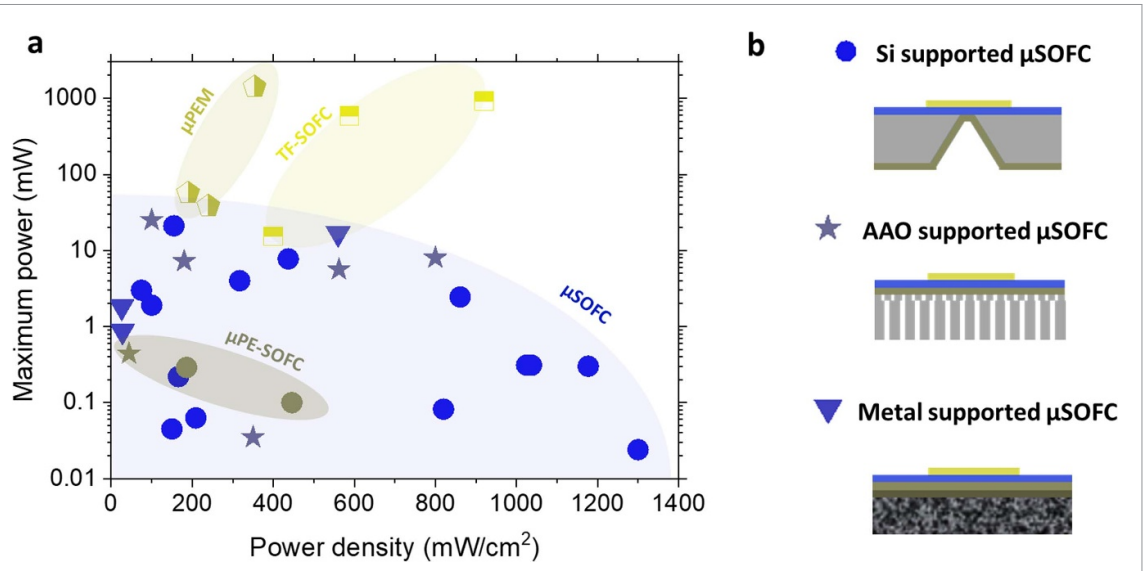

Figure 9. (a) Maximum power and power density were obtained in literature for the different types of miniaturized fuel cells reported in table 5. Thin Film SOFC (TF) is also included in the graph for comparison. The main types of μSOFCs, sorted by the type of support used, are schematically shown in (b), along with cross-sectional images of the fuel cell.

in total power measured, meaning that such power densities are mainly achievable when using very small active areas. This limitation is not due to poor performances of the μSOFC components, since TF-SOFC can deliver power up to Watts, rather to the integration of dense thin films into porous substrates or self-sustained membranes, which may result in gas leakages or short circuits when large active areas are used. Another challenge that remains to be fully addressed is the integration of the fuel cell with the other auxiliary components, such as fuel micro-reformer or post combustor unit, in a compact and miniaturized system [365, 366].

3.2.3. Outlook

For rechargeable on-demand powering devices in IoT applications, fuel cell concepts may be preferred against battery solutions, when fast charging times are required or their implementation is beneficial for specific device functionality. Therefore, fuel cells have found their way into commercialization in small devices, with a prime example of a methanol fuel-cell-powered hearing aid brought into the market by Widex Inc.® (Widex Energy Cell®), which allows recharging of the methane-based PEM power supply within 20 s, rather than within hours for typical battery-power devices, and allowing 24 h of operation [367].

Finally, we notice that one of the main appealing features of micro fuel cells is the large energy density deriving from the use of liquid or gaseous fuels (up to 1 Wh L^{-1}), which is expected to allow a long off-grid (off-refueling) operation [368]. Yet, the employment of fuels may also represent a limitation when powering remote IoT devices, since the refilling of the fuel tank would be needed to 'recharge' the μSOFCs. As a possible solution, a micro Solid Oxide Electrolysis Cell may be envisioned for promoting the reverse electrochemical reaction and generating a fuel, such as a hydrogen from environmental humidity, when excess energy from neighboring energy harvesting devices is available. In this way, a long-term operation in remote IoT devices may be achieved. Such remote electrolyzer technology, however, is yet in the early stage of research. Nevertheless, electrolyzer functionality is in principle accessible by running micro fuel cells in 'reverse' mode, to switch electrochemical conversion from fuel to electrical power in opposite direction and thus generating fuel from water. A futuristic prospect for a remote IoT device may be equipped with such a bifunctional electrochemical cell, capable of burning fuel when electrical power is required and producing fuel when excess electrical energy is available. Systemically collecting water by a capillary or microfluidic collector device may e.g. allow providing humidity in a small and controlled amount to the electrolyzer to restore the fuel level of the devices.

At this stage, the application of fuel cells and electrolyzers may be considered a niche in current IoT technologies. However, increasing degrees of miniaturization further enhanced power density, and increased conversion efficiency can be expected from fundamental research in the coming years, making such technologies a valuable member of the IoT toolbox.

Table 10. Comparison among performances, operating conditions, and characteristics of a selection of micro fuel cells presented in the literature. Notation: Si: Silicon supported, STS: Stainless steel, AAO: anodized aluminum oxide, YSZ: Yttria stabilized zirconia, LSCF: Sr doped Lanthanum cobalt ferrite, LSC: Strontium doped lanthanum cobaltite, GDC: Gadolinium doped Ceria, SDC: Samarium doped Ceria, BZY: Yttrium doped Barium Zirconate.

	References	Year	Substrate	Composition Cathode/ electrolyte/ anode	Op. T (°C)	Max. Power (mW)	Max. power density (mW/cm^2)	Active area (mm^2)	Current at power peak (A cm^{-2})	Voltage at current peak (V)	V_{oc} (V)
μSOFC	An *et al* [369]	2013	Si, corrugated	Pt/YSZ-YDC/Pt	450	0.024	1300	0.002	4.1	0.32	1.05
	Chao *et al* [370]	2011	Si, corrugated	Pt/YSZ/Pt	450	0.082	820	0.01	3	0.27	1.11
	Su *et al* [370]	2008	Si, corrugated	Pt/YSZ/Pt	450	2.44	861	0.3	2.7	0.318	1.09
	Tölke *et al* [371]	2012	Foturan®	Pt/YSZ/Pt	550	0.063	209	0.03	0.62	0.34	0.57
	Muecke *et al* [372]	2008	Foturan®	Pt/YSZ/Pt	550	0.045	150	0.03	0.36	0.42	0.77
	Schlupp *et al* [373]	2014	Si	Pt/YSZ/Pt	410	0.22	166	0.13	0.47	0.35	0.84
	Kerman *et al* [374]	2011	Si	Pt/YSZ/Pt	500	0.31	1037	0.03	3.3	0.314	0.97
	Tsuchiya *et al* [375]	2011	Si	Pt/YSZ/LSCF	510	21.1	155	25	0.46	0.34	0.75
	Kerman *et al* [376]	2012	Si	Pt/YSZ-CGO/Pt	510	0.31	1025	0.03	4.4	0.23	0.41
	Kerman *et al* [377]	2012	Si	Pt/CGO/Pt (Ru)	520	0.3	1177	0.03	4	0.29	0.6
	Kerman *et al* [378]	2015	Si	Pt/YSZ/Pt	500	3	75	3.14	0.25	0.3	0.87
	Garbayo *et al* [379]	2014	Si	LSC/YSZ/CGO	750	1.9	100	1.9	0.17	0.58	1.1
	Baek *et al* [380]	2015	Si	Pt/YSZ/Pt	400	7.72	437	17.6	1.3	0.34	1.1
	Baek *et al* [381]	2016	Si	Pt/YSZ/Pt	400	4	317	1.2	1.1	0.29	1.04
	Kim *et al* [382]	2016	STS/YSZ	LSC/YSZ/Ni-YSZ	550	16.8	560	3	1.3	0.46	1.1
	Joo *et al* [383]	2008	Ni	Pt-LSC/GDC/Ni	450	1.82	26	7	0.07	0.37	0.87
	Lee *et al* [384]	2014	Ni/STS	Pt-LSC/YSZ-GDC/Ni-GDC	450	0.87	28	3.1	0.07	0.4	0.91
	Kwon *et al* [385]	2011	AAO	Pt/YSZ/Pt	500	0.035	350	0.01	1.2	0.29	1.02
	Park *et al* [386]	2014	AAO	Pt/YSZ-GDC-YSZ/Pt	500	25	100	25	0.25	0.40	1.1
	Oh *et al* [387]	2018	AAO	Pt/SDC-YSZ-SDC/Pt	450	5.62	562	1	1.25	0.45	1.07
	Ha *et al* [388]	2013	AAO	Pt/YSZ/Pt	450	7.2	180	4	0.37	0.48	1.14
	Shin *et al* [389]	2019	AAO	Pt/SDC-YSZ-SDC/Pt-Ceria	500	8	800	1	1.8	0.44	1.14
μ-PC-SOFC	Li *et al* [390]	2016	Si	Pt/GDC-BZY/Pt	425	0.1	446	0.022	2.25	0.20	1.1
	Kim *et al* [391]	2011	Si, corrugated	Pt/BZY/Pt	450	0.29	186	0.16	0.9	0.21	1.0
	Chang *et al* [392]	2013	AAO	Pt/BZY/Pt	450	0.44	44	1	0.12	0.37	1.0
TF-SOFC	Reolon *et al* [393]	2018	NiO-YSZ	Pt-LSC/CGO-YSZ/Ni-YSZ	650	15.4	400	38.5	0.7	0.57	0.91
	Shin *et al* [384]	2020	NiO-YSZ	LSC/CGO/Ni-YSZ	500	920	920	100	1.7	0.54	1.14
	Noh *et al* [394]	2014	NiO-YSZ	LSC-GDC/CGO-YSZ/Ni-YSZ	500	588	588	100	1.2	0.49	1.1
μ-PEM	Yu *et al* [347]	2019	Si	Pt-C/Nafion/Pt-C	80	1416	354	400	0.8	0.44	0.98
	Yu *et al* [344]	2003	Si	Pt-C/Nafion/Pt-C	25	57	190	30	0.26	0.73 (2 cells)	1.9
	Morisawa *et al* [347]	2014	Si	Pt-C/Nafion/Pt-C	45	38.4	240	16	0.4	0.5	1

4. Section-III: power management for IoT applications

Power management units (PMUs) are rapidly being developed to provide a significant amount of power for sensors in IoT networks. The DC–DC power converter is the main component in the PMU placed in between the power sources and the IoT devices. The aims of the DC–DC converters are to:

- **Regulate the input voltage coming from the sources to a required output voltage level to operate the IoT device**; Match the source impedance with the IoT device impedance to achieve the maximum power transfer.

To maintain a long battery or sustainable power sources life, high power-conversion efficiency is critical for the PMU since it can add substantial overhead to the overall power consumption of the chip.

4.1. DC–DC power converters

IoT applications operate at low supply voltages which often range below 1 V, while the battery as the primary or auxiliary power source for their stable voltage supply provides a voltage range from 1.2 V to 5 V. This requires DC–DC converters to step down voltages. Low dropout (LDO) regulators [395, 396] provide high supply rejection and regulated output voltage. However, this approach results in poor power efficiency. Buck converters are a common architecture in step-down voltage converters for higher power regulations [397, 398]. Because of the large overhead associated with its control [398] along with the inductor size, buck converters are also not good candidates for low power applications. Another approach is to use a switched-capacitor DC–DC converter which has a power efficiency of up to 97% [399]. However, switched capacitor designs typically only divide the input voltage and do not provide the ability of voltage regulation [400]. A hybrid architecture has been shown in [401–403] where the first stage divides the battery voltage by five using a switched capacitor DC–DC converter, then the design uses an LDO in the second stage for output voltage regulation. However, the two-stage approaches suffer a lower conversion efficiency. It has been shown to achieve maximum efficiency, where the hybrid architecture regulates a 1.3 V input to 0.4 V and achieves a power efficiency of >80% for load ranges 1–240 μA [401].

4.2. Maximum power point tracking (MPPT) control

When electrically connected to an external load, the power energy sources such as solar and TEGs have power characteristic curves where the impedance of the external load has a particular unique size, maximum power is retrieved. This unique impedance varies considerably with both the design of the power energy sources and their operating conditions. Subsequently, a MPPT control method needs to be utilized to actively emulate the impedance of DC–DC to match the inner impedance of the power energy sources so that the sources are always operating at the maximum power point.

State-of-the-art solutions are capable of performing MPPT and/or charging capabilities with dc renewable sources [404–408]. As the I–V and P–V characteristics of the TEG follow the same principles as that of the solar panel, MPPT techniques that are commonly used for solar panels can be reused for the TEG, for instance, the perturb and observe (P&O) algorithm, hill climbing, and incremental conductance technique. One of the most popular MPP finding methods in IoT applications is called fractional open-circuit voltage (FOCV)[408]. FOCV method samples the open-circuit voltage (VOC) of the energy harvester first and then determines the ratio of the VOC, which corresponds to the maximum power point of the energy harvester. It is an *a priori* technique based on many past analyses and experiments with the findings that the MPP for PV cells is around 0.71–0.82 of their VOC while other types of energy sources, such as RF rectennas, TEGs, PEHs, and EMGs, are around half of the open-circuit voltage (VOC/2). The PMU proposed in [406] is comprised of a 10× step-up charge pump with two-dimensional (2-D) tuning for MPPT and a digital LDO regulator with input power sense capabilities.

4.3. Challenges and trends

- The single battery source-based IoT system falls into disuse. The more renewable energy sources with a combination of battery sources start to play a mainstreaming to maintain long battery or sustainable power sources' life. This requires new circuit architectures with multiple inputs for power management to efficiently deal with the power.
- Providing both MPPT as well as output voltage regulation is still an issue to be fully resolved. The state of the art still used two-stage power converters. The first stage is usually buck, boost, or switched capacitor converters with the implementation of MPPT power transfer, and the second stage is usually the LDO or another DC–DC converter to regulate the output voltage fitting within the applications. This two-stage solution gives a poor PCE and a relatively larger size of the PMU. There might be a chance for researchers to integrate as a single-stage circuit architecture for both MPPT and output voltage regulation functions.
- The PMU requires low power consumption, small chips, small external components, such as inductors and capacitors, and high efficiency. Therefore, low power and high-efficiency power management integrated circuit (PMIC) is important to extend battery life and sustain the system without charge. The main challenge is how to integrate bulk components such as inductors and capacitors in the same silicon substrate. A novel three-dimensional in-silicon through-silicon via (TSV) magnetic-core toroidal inductor for power supply

in packing is proposed in [409], and the first interposer converter with 3D TSV inductor is demonstrated at DTU [410].

5. Concluding remarks

Harvesting and storage of energy play an important role in the efficiency and lifetime of IoT devices. The central goal of energy harvesting systems for IoT is to move from battery-based devices to an autonomous energy harvesting system that relies on energy harvested from the ambient environment. To reduce the power consumption of batteries, a crucial step is to find alternative harvesting and storage solutions and optimize the PMICs, which helps to enhance the system's life span. In this review paper, we summarized the current state-of-the-art IoT enabling and emerging harvesting and storage technologies covering the areas of energy harvesting- and storage devices, and power management for IoT applications.

To harvest energy from a sustainable power supply, it is important to ensure the availability of the energy source from which energy is supposed to be harvested, the high amount of harvested energy, and the high efficiency of the harvesting system just to name a few. In this review, we have provided some of the limitations and solutions concerning the energy sources and the way to harvest these. However, in reality, the sources of energy are not continuous, and hence, a new way to ensure the continuous operation of IoT devices should be considered. Recent advancements in IoT have drawn the attention of researchers and developers toward systems where the storage unit is installed together with the harvesting units in the same device [9, 281, 282, 411]. This surely increases the complexity of the IoT devices from the viewpoint of electronics, when compared to the electronics associated with only battery-powered IoT devices, but on the other hand, it provides an efficient and autonomous solution.

Furthermore, most of the harvesting devices discussed in this paper show the technological potential to replace batteries for powering the IoT from the viewpoint of power output per unit device cross-section area. The integration of high density of harvesting devices with a small footprint area is required to reach the actual requirements of the power needed for the devices during the different modes of their operation. Finally, the cost factors, such as the cost of the harvester system as compared with the battery storage must also be considered when designing such a system [29]. Despite having still a vast amount of challenges in the integration of the energy harvesting devices into the IoT units and their operation, they remain one of the most reliable practical solutions for the replacement of batteries.

Data availability statement

The data that support the findings of this study are available upon reasonable request from the authors.

Acknowledgments

A C and N P acknowledge the European Union's H2020 Programme under Grant Agreement No. 824072-HARVESTORE. C I and R B acknowledge the Independent Research Fund Denmark, project 8022-00038B for sponsoring part of this work. H Z, V E, and N P acknowledge the BioWings project funded by the European Union's Horizon 2020, Future and Emerging Technologies (FET) program (Grant No. 801267). N P acknowledges the funding from the Independent Research Technology and Production Science, DFF Research 3 PILOT (Grant No. 00069B). F G thanks for funding from the European Union's Horizon 2020 research and innovation program under Marie Sklodowska-Curie Grant Agreement No. 713683 (COFUNDfellowsDTU). H A, M A, C Y H, and M M acknowledge a) Danmarks Frie Forskningsfond, DFF for funding of the project Powering the Internet-of-Things with Ambient Solutions (PIIoT), No. 0217-00069B and b) Danish Ministry of Higher Education and Science for providing support from the project 'SMART—Structure of MAterials in Real-Time'.

Author contributions

Initiating the idea, structuring the review article, abstract, introduction, and concluding remarks- A C, and N P; Thermoelectricity for IoT- A C, C N L, and N P; Piezoelectricity for IoT- H Z, A B and V E; Flexoelectricity for IoT- S Y, A R I, and D V C; Electromagnetic energy harvester- C I and R B; Photovoltaics for IoT- H A, M A, C Y H, and M M; Battery for IoT- J C and P N; Fuel cells and electrolyzers for IoT- F M C and F G; Power management for IoT applications- Z O. All authors reviewed and edited the manuscript.

Conflict of interest

Authors declare no conflict of interest.

ORCID iDs

Arindom Chatterjee https://orcid.org/0000-0002-0861-2058
Carlos Nuñez Lobato https://orcid.org/0000-0002-9423-7740
Haiwu Zhang https://orcid.org/0000-0003-4354-3948
Achilles Bergne https://orcid.org/0000-0003-4666-8965
Vincenzo Esposito https://orcid.org/0000-0002-9817-7810
Shinhee Yun https://orcid.org/0000-0001-6680-3269
Dennis Valbjørn Christensen https://orcid.org/0000-0003-0048-7595
Carlos Imbaquingo https://orcid.org/0000-0003-4343-053X
Rasmus Bjørk https://orcid.org/0000-0002-3728-2326
Mariam Ahmad https://orcid.org/0000-0002-1114-8073
Chun Yuen Ho https://orcid.org/0000-0001-6045-4715
Morten Madsen https://orcid.org/0000-0001-6503-0479
Jixi Chen https://orcid.org/0000-0002-7897-6703
Poul Norby https://orcid.org/0000-0002-2590-7050
Francesco Maria Chiabrera https://orcid.org/0000-0001-8940-2708
Felix Gunkel https://orcid.org/0000-0003-1178-9986
Ziwei Ouyang https://orcid.org/0000-0001-7046-9224
Nini Pryds https://orcid.org/0000-0002-5718-7924

References

[1] Alan Young 2015 The internet of things: the impact on the travel and hotel industry (available at: www.hospitalitynet.org/opinion/4071511.html)
[2] Eid A, Hester J and Tentzeris M M 2019 A scalable high-gain and large-beamwidth mm-wave harvesting approach for 5G-powered IoT *2019 IEEE MTT-S Int. Microwave Symp. (IMS)* (*Boston, MA, USA*) pp 1309–12
[3] McKenna H P 2017 Urbanizing the ambient: why people matter so much in smart cities *Enriching Urban Spaces with Ambient Computing, the Internet of Things, and Smart City Design edited by Shin'ichi Konomi and George Roussos* (Hershey, PA: IGI Global) pp 209–31
[4] Latré B, Braem B, Moerman I, Blondia C and Demeester P 2011 A survey on wireless body area networks *Wirel. Networks* **17** 1–18
[5] Chen M, Gonzalez S, Vasilakos A, Cao H and Leung V C M 2011 Body area networks: a survey *Mob. Networks Appl.* **16** 171–93
[6] Szulewski P 2016 Industrial automation products in the conception of industry 4.0 (Mechanik NR 8-9/2016) 926–33
[7] Jayakumar H, Lee K, Lee W S, Raha A, Kim Y and Raghunathan V 2014 Powering the internet of things *2014 IEEE/ACM Int. Symp. on Low Power Electronics and Design (ISLPED)* (*La Jolla, CA, USA*, *2014*) (ACM) pp 375–80
[8] Ramadass Y 2014 Powering the internet of things *2014 IEEE Hot Chips 26 Symp. (HCS)* (*Cupertino, CA, USA*, *2014*) (IEEE) pp 1–50
[9] Tarancón A 2019 Powering the IoT revolution with heat *Nat. Electron.* **2** 270–1
[10] Raj A and Steingart D 2018 Review—power sources for the internet of things *J. Electrochem. Soc.* **165** B3130–6
[11] Saurav P Batteries for IoT devices (available at: www.baseapp.com/iot/batteries-iot-device-types-character/)
[12] Blomgren G E 2017 The development and future of lithium ion batteries *J. Electrochem. Soc.* **164** A5019–25
[13] Zamarayeva A M, Gaikwad A M, Deckman I, Wang M, Khau B, Steingart D A and Arias A C 2016 Fabrication of a high-performance flexible silver–zinc wire battery *Adv. Electron. Mater.* **2** 1500296
[14] Gaikwad A M, Arias A C and Steingart D A 2014 Recent progress on printed flexible batteries: mechanical challenges, printing technologies, and future prospects *Energy Technol.* **3** 305–28
[15] Liu W, Chen J, Chen Z, Liu K, Zhou G, Sun Y, Song M, Bao Z and Cui Y 2017 Stretchable lithium-ion batteries enabled by device-scaled wavy structure and elastic-sticky separator *Adv. Energy Mater.* **7** 1701076
[16] Force Technology Powering IoT sensors using ambient energy (available at: https://forcetechnology.com/en/articles/iot-sensors-energy-harvesting-energy)
[17] Franciscatto B 2016 Design and implementation of a new low-power consumption *DSRC transponder PhD thesis* Université de Grenoble (available at: https://tel.archives-ouvertes.fr/tel-01293522)
[18] Oy S A and Özdemir A E 2021 Design of a piezoelectric energy conversion based wind generator *Int. J. Electr. Eng. Educ.* 1–14
[19] Bairagi S, Ghosh S and Ali S W 2020 A fully sustainable, self-poled, bio-waste based piezoelectric nanogenerator: electricity generation from pomelo fruit membrane *Sci. Rep.* **10** 12121
[20] Shaukat R A, Saqib Q M, Khan M U, Chougale M Y and Bae J 2021 Bio-waste sunflower husks powder based recycled triboelectric nanogenerator for energy harvesting *Energy Rep.* **7** 724–31
[21] Nasir A A, Zhou X, S Durrani and Kennedy R A 2013 Relaying protocols for wireless energy harvesting and information processing *IEEE Trans. on Wireless Communications* (*July 2013*) vol 12 pp 3622–36
[22] KAMCAP Super capacitor & ultracapacitor for internet of things (available at: www.kamcappower.com/super-capacitor-ultracapacitor-internet-of-things.html)
[23] Zhu Y, Murali S, Stoller M D, Ganesh K J, Cai W, Ferreira P J, Pirkle A, Wallace R M, Cychosz K A, Thommes M, Su D, Stach E A and Ruoff R S 2011 Carbon-based supercapacitors produced by activation of graphene *Science* **332** 1537–41
[24] Zhang H, Zhang L, Chen J, Su H, Liu F and Yang W 2016 One-step synthesis of hierarchically porous carbons for high-performance electric double layer supercapacitors *J. Power Sources* **315** 120–6
[25] Meng C, Maeng J, John S W M and Irazoqui P P 2014 Ultrasmall integrated 3D micro-supercapacitors solve energy storage for miniature devices *Adv. Energy Mater.* **4** 1301269
[26] Ma H, Zhang Y and Shen M 2021 Application and prospect of supercapacitors in internet of energy (IOE) *J. Energy Storage* **44** 103299

[27] Şahin M E, Blaabjerg F and Sangwongwanich A 2022 A comprehensive review on supercapacitor applications and developments *Energies* **15** 674
[28] Kim M-S, Gaudiot J and Goldman A 2016 Survey of supercapacitor's application for power awareness of embedded systems in internet of things *Int. Conf. on EEECS: Innovation and Convergence* (*Phuket, Thailand*)
[29] Narducci D 2019 Thermoelectric harvesters and the internet of things: technological and economic drivers *J. Phys. Energy* **1** 024001
[30] Shirvanimoghaddam M, Shirvanimoghaddam K, Abolhasani M M, Farhangi M, Barsari V Z, Liu H, Dohler M and Naebe M 2019 Towards a green and self-powered internet of things using piezoelectric energy harvesting *IEEE Access* **7** 94533–56
[31] Mathews I, Kantareddy S N, Buonassisi T and Peters I M 2019 Technology and market perspective for indoor photovoltaic cells *Joule* **3** 1415–26
[32] Yan J, Liao X, Yan D and Chen Y 2018 Review of micro thermoelectric generator *J. Microelectromech. Syst.* **27** 1–18
[33] Jaziri N, Boughamoura A, Müller J, Mezghani B, Tounsi F and Ismail M 2020 A comprehensive review of thermoelectric generators: technologies and common applications *Energy Rep.* **6** 264–87
[34] Wang Y, Yang L, Shi X L, Shi X, Chen L, Dargusch M S, Zou J and Chen Z G 2019 Flexible thermoelectric materials and generators: challenges and innovations *Adv. Mater.* **31** 1807916
[35] Nozariasbmarz A, Collins H, Dsouza K, Polash M H, Hosseini M, Hyland M, Liu J, Malhotra A, Ortiz F M, Mohaddes F, Ramesh V P, Sargolzaeiaval Y, Snouwaert N, Özturk M C and Vashaee D 2020 Review of wearable thermoelectric energy harvesting: from body temperature to electronic systems *Appl. Energy* **258** 114069
[36] Khan S, Kim J, Acharya S and Kim W 2021 Review on the operation of wearable sensors through body heat harvesting based on thermoelectric devices *Appl. Phys. Lett.* **118** 200501
[37] Haras M and Skotnicki T 2018 Thermoelectricity for IoT—a review *Nano Energy* **54** 461–76
[38] Yang J and Caillat T 2006 Thermoelectric materials for space *MRS Bull.* **31** 224–9
[39] Rowe D M 1995 *CRC Handbook of Thermoelectrics* 1st edn (Boca Raton, FL: CRC Press) (https://doi.org/10.1201/9781420049718)
[40] Snyder G J and Toberer E S 2008 Complex thermoelectric materials *Nat. Mater.* **7** 105–14
[41] Salleras M, Donmez-Noyan I, Dolcet M, Santander J, Estrada-Wiese D, Sojo J-M, Gadea G, Morata A, Tarancon A and Fonseca L 2021 Managing heat transfer issues in thermoelectric microgenerators *Heat Transfer - Design, Experimentation and Applications* (IntechOpen) pp 1–23
[42] Lee M 2020 Silicon: a revenant thermoelectric material? *J. Supercond. Nov. Magn.* **33** 253–7
[43] Dhawan R, Madusanka P, Hu G, Debord J, Tran T, Maggio K, Edwards H and Lee M 2020 Si0.97Ge0.03 microelectronic thermoelectric generators with high power and voltage densities *Nat. Commun.* **11** 4362
[44] Zeier W G, Zevalkink A, Gibbs Z M, Hautier G, Kanatzidis M G and Snyder G J 2016 Thinking like a chemist: intuition in thermoelectric materials *Angew. Chem. Int. Ed.* **55** 6826–41
[45] Heremans J P, Wiendlocha B and Chamoire A M 2012 Resonant levels in bulk thermoelectric semiconductors *Energy Environ. Sci.* **5** 5510–30
[46] Sootsman J R, Chung D Y and Kanatzidis M G 2009 New and old concepts in thermoelectric materials *Angew. Chem., Int. Ed.* **48** 8616–39
[47] Freer R *et al* 2022 Key properties of inorganic thermoelectric materials—tables (version 1) *J. Phys. Energy* **4** 022002
[48] Rogl G and Rogl P 2017 Skutterudites, a most promising group of thermoelectric materials *Curr. Opin. Green Sustain. Chem.* **4** 50–57
[49] Fu C, Auffermann G, Fecher G H Felser C and Schnelle W Half-Heusler compounds for thermoelectric energy conversion (available at: www.cpfs.mpg.de/thermoelectrics)
[50] Buffon M L C 2017 *Heusler Materials for Thermoelectric Applications: Phase Separation, Atomic Site Disorder, and Interstitials PhD Thesis* University of California, Santa Barbara
[51] Dolyniuk J-A, Owens-Baird B, Wang J, Zaikina J V and Kovnir K 2016 Clathrate thermoelectrics *Mater. Sci. Eng.* **108** 1–46
[52] Kauzlarich S M, Zevalkink A, Toberer E and Snyder G J 2017 Zintl phases: recent developments in thermoelectrics and future outlook *Thermoelectric Materials and Devices* Nandhakumar I, White N M and Beeby S Energy and Environment Series (London: Royal Society of Chemistry) ch 1, pp 1–26
[53] Balvanz A, Qu J, Baranets S, Ertekin E, Gorai P and Bobev S 2020 New n-type zintl phases for thermoelectrics: discovery, structural characterization, and band engineering of the compounds A2CdP2(A = Sr, Ba, Eu) *Chem. Mater.* **32** 10697–707
[54] Kauzlarich S M, Brown S R and Snyder G J 2007 Zintl phases for thermoelectric devices *Dalton Trans.* **2007** 2099–107
[55] Famengo A, Boldrini S, Battiston S, Fiameni S, Miozzo A, Fabrizio M and Barison S 2014 Silica-based materials for thermoelectric-legs embedding *Proc. 11th European Conf. on Thermoelectrics* ed A Amaldi (Cham: Springer) pp 89–98
[56] Pérez-Taborda J A, Caballero-Calero O and Martín-González M 2017 Silicon-germanium (SiGe) nanostructures for thermoelectric devices: recent advances and new approach to high thermoelectric efficiency *New Research on Silicon- Structure, Properties, Technology* ed V I Talanin vol 32 (IntechOpen) ch 8, p 183
[57] Shi Y, Sturm C and Kleinke H 2019 Chalcogenides as thermoelectric materials *J. Solid State Chem.* **270** 273–9
[58] Tan G, Shi F, Hao S, Zhao L-D, Chi H, Zhang X, Uher C, Wolverton C, Dravid V P and Kanatzidis M G 2016 Non-equilibrium processing leads to record high thermoelectric figure of merit in PbTe–SrTe *Nat. Commun.* **7** 12167
[59] Terasaki I 2016 Research update: oxide thermoelectrics: beyond the conventional design rules *APL Mater.* **4** 104501
[60] Chatterjee A, Lan Z, Christensen D V, Bauitti F, Morata A, Chavez-Angel E, Sanna S, Castelli I E, Chen Y, Tarancon A and Pryds N 2022 On the thermoelectric properties of Nb-doped SrTiO3epitaxial thin films *Phys. Chem. Chem. Phys.* **24** 3741–8
[61] Chatterjee A, Chavez-Angel E, Ballesteros B, Caicedo J M, Padilla-Pantoja J, Leborán V, Torres C M S, Rivadulla F and Santiso J 2020 Large thermoelectric power variations in epitaxial thin films of layered perovskite GdBaCo2O5.5±δwith a different preferred orientation and strain *J. Mater. Chem.* A **8** 19975–83
[62] Zhao L D, Chang C, Tan G and Kanatzidis M G 2016 SnSe: a remarkable new thermoelectric material *Energy Environ. Sci.* **9** 3044–60
[63] Xie L, He D and He J 2021 SnSe, the rising star thermoelectric material: a new paradigm in atomic blocks, building intriguing physical properties *Mater. Horiz.* **8** 1847–65
[64] Zhou C, Lee Y K, Yu Y, Byun S, Luo Z Z, Lee H, Ge B, Lee Y L, Chen X, Lee J Y, Cojocaru-Mirédin O, Chang H, Im J, Cho S P, Wuttig M, Dravid V P, Kanatzidis M G and Chung I 2021 Polycrystalline SnSe with a thermoelectric figure of merit greater than the single crystal *Nat. Mater.* **20** 1378–84
[65] Vikhor L M, Anatychuk L I and Gorskyi P V 2019 Electrical resistance of metal contact to Bi_2Te_3 based thermoelectric legs *J. Appl. Phys.* **126** 164503

[66] Wang S, Xie T and Xie H 2018 Experimental study of the effects of the thermal contact resistance on the performance of thermoelectric generator *Appl. Therm. Eng.* **130** 847–53

[67] Hinterleitner B, Knapp I, Poneder M, Shi Y, Müller H, Eguchi G, Eisenmenger-Sittner C, Stöger-Pollach M, Kakefuda Y, Kawamoto N, Guo Q, Baba T, Mori T, Ullah S, Chen X Q and Bauer E 2019 Thermoelectric performance of a metastable thin-film Heusler alloy *Nature* **576** 85–90

[68] Liu J, van der Zee B, Alessandri R, Sami S, Dong J, Nugraha M I, Barker A J, Rousseva S, Qiu L, Qiu X, Klasen N, Chiechi R C, Baran D, Caironi M, Anthopoulos T D, Portale G, Havenith R W A, Marrink S J, Hummelen J C and Koster L J A 2020 N-type organic thermoelectrics: demonstration of ZT > 0.3 *Nat. Commun.* **11** 5694

[69] Hu G, Edwards H and Lee M 2019 Silicon integrated circuit thermoelectric generators with a high specific power generation capacity *Nat. Electron.* **2** 300–6

[70] Sailor M J and Link J R 2005 "Smart dust": nanostructured devices in a grain of sand *Chem. Commun.* **36** 1375–83

[71] Ziouche K, Yuan Z, Lejeune P, Lasri T, Leclercq D and Bougrioua Z 2017 Silicon-based monolithic planar micro thermoelectric generator using bonding technology *J. Microelectromech. Syst.* **26** 45–47

[72] Toberer E S, Cox C A, Brown S R, Ikeda T, May A F, Kauzlarich S M and Jeffrey Snyder G 2008 Traversing the metal-insulator transition in a zintl phase: rational enhancement of thermoelectric efficiency in $Yb_{14}Mn_{1-x}Al_xSb_{11}$ *Adv. Funct. Mater.* **18** 2795–800

[73] Yan X, Liu W, Wang H, Chen S, Shiomi J, Esfarjani K, Wang H, Wang D, Chen G and Ren Z 2012 Stronger phonon scattering by larger differences in atomic mass and size in p-type half-Heuslers $Hf_{1-x}Ti_xCoSb_{0.8}Sn_{0.2}$ *Energy Environ. Sci.* **5** 7543–8

[74] Sekimoto T, Kurosaki K, Muta H and Yamanaka S 2007 High-thermoelectric figure of merit realized in p-type half-Heusler compounds: zrCoSnxSb1-x *Jpn. J. Appl. Phys.* **46** L673

[75] Van Nong N, Pryds N, Linderoth S and Ohtaki M 2011 Enhancement of the thermoelectric performance of p-type layered oxide Ca3Co4O9+δ through heavy doping and metallic nanoinclusions *Adv. Mater.* **23** 2484–90

[76] Chung D-Y, Hogan T P, Rocci-Lane M, Brazis P, Ireland J R, Kannewurf C R, Bastea M, Uher C, Kanatzidis M G 2004 A new thermoelectric material: $csBi_4Te_6$ *J. Am. Chem. Soc.* **126** 6414–28

[77] Pei Y L, Wu H, Wu D, Zheng F and He J 2014 High thermoelectric performance realized in a bicuseo system by improving carrier mobility through 3D modulation doping *J. Am. Chem. Soc.* **136** 13902–8

[78] Poudel B, Hao Q, Ma Y, Lan Y, Minnich A, Yu B, Yan X, Wang D, Muto A, Vashaee D, Chen X, Liu J, Dresselhaus M S, Chen G and Ren Z 2008 High-thermoelectric performance of nanostructured bismuth antimony telluride bulk alloys *Science* **320** 634–8

[79] Kim S I, Lee K H, Mun H A, Kim H S, Hwang S W, Roh J W, Yang D J, Shin W H, Li X S, Lee Y H, Snyder G J and Kim S W 2015 Dense dislocation arrays embedded in grain boundaries for high-performance bulk thermoelectrics *Science* **348** 109–14

[80] Zhao L D, Tan G, Hao S, He J, Pei Y, Chi H, Wang H, Gong S, Xu H, Dravid V P, Uher C, Snyder G J, Wolverton C and Kanatzidis M G 2016 Ultrahigh power factor and thermoelectric performance in hole-doped single-crystal SnSe *Science* **351** 141–4

[81] He W, Wang D, Wu H, Xiao Y, Zhang Y, He D, Feng Y, Hao Y-J, Dong J-F, Chetty R, Hao L, Chen D, Qin J, Yang Q, Li X, Song J-M, Zhu Y, Xu W, Niu C, Li X, Wang G, Liu C, Ohta M, Pennycook S J, He J, Li J-F and Zhao L-D 2019 High thermoelectric performance in low-cost $SnS_{0.91}Se_{0.09}$ crystals *Science* **365** 1418–24

[82] Fu C, Bai S, Liu Y, Tang Y, Chen L, Zhao X and Zhu T 2015 Realizing high figure of merit in heavy-band p-type half-Heusler thermoelectric materials *Nat. Commun.* **6** 8144

[83] Zhao L-D, Lo S-H, Zhang Y, Sun H, Tan G, Uher C, Wolverton C, Dravid V P and Kanatzidis M G 2014 Ultralow thermal conductivity and high thermoelectric figure of merit in SnSe crystals. *Nature* **508** 373–7

[84] Qin B, Wang D, Liu X, Qin Y, Dong J F, Luo J, Li J W, Liu W, Tan G, Tang X, Li J F, He J and Zhao L D 2021 Power generation and thermoelectric cooling enabled by momentum and energy multiband alignments *Science* **373** 556–61

[85] Biswas K, He J, Blum I D, Wu C I, Hogan T P, Seidman D N, Dravid V P and Kanatzidis M G 2012 High-performance bulk thermoelectrics with all-scale hierarchical architectures *Nature* **489** 414–8

[86] Roychowdhury S, Ghosh T, Arora R, Samanta M, Xie L, Singh N K, Soni A, He J, Waghmare U V and Biswas K 2021 Enhanced atomic ordering leads to high thermoelectric performance in AgSbTe2 *Science* **371** 722–7

[87] Zhao X B, Ji X H, Zhang Y H, Zhu T J, Tu J P and Zhang X B 2005 Bismuth telluride nanotubes and the effects on the thermoelectric properties of nanotube-containing nanocomposites *Appl. Phys. Lett.* **86** 062111

[88] Wang Q, Quhe R, Guan Z, Wu L, Bi J, Guan P, Lei M and Lu P 2018 High n-type and p-type thermoelectric performance of two-dimensional SiTe at high temperature *RSC Adv.* **8** 21280–7

[89] Mao J, Zhu H, Ding Z, Liu Z, Gamage GA, Chen G and Ren Z 2019 High thermoelectric cooling performance of n-type Mg3Bi2-based materials *Science* **365** 495–8

[90] Wan C, Gu X, Dang F, Itoh T, Wang Y, Sasaki H, Kondo M, Koga K, Yabuki K, Snyder G J, Yang R and Koumoto K 2015 Flexible n-type thermoelectric materials by organic intercalation of layered transition metal dichalcogenide TiS2 *Nat. Mater.* **14** 622–7

[91] Zhang J, Song L, Pedersen S H, Yin H, Hung L T and Iversen B B 2017 Discovery of high-performance low-cost n-type Mg3Sb2-based thermoelectric materials with multi-valley conduction bands *Nat. Commun.* **8** 13901

[92] Saramat A, Svensson G, Palmqvist A E C, Stiewe C, Mueller E, Platzek D, Williams S G K, Rowe D M, Bryan J D and Stucky G D 2006 Large thermoelectric figure of merit at high temperature in Czochralski-grown clathrate Ba 8Ga 16Ge 30 *J. Appl. Phys.* **99** 023708

[93] Jiang B, Yu Y, Cui J, Liu X, Xie L, Liao J, Zhang Q, Huang Y, Ning S, Jia B, Zhu B, Bai S, Chen L, Pennycook S J and He J 2021 High-entropy-stabilized chalcogenides with high thermoelectric performance *Science* **371** 830–4

[94] Liu W, Tan X, Yin K, Liu H, Tang X, Shi J, Zhang Q and Uher C 2012 Convergence of conduction bands as a means of enhancing thermoelectric performance of n-type Mg 2Si 1-xSn x solid solutions *Phys. Rev. Lett.* **108** 166601

[95] Jabar B, Li F, Zheng Z, Mansoor A, Zhu Y, Liang C, Ao D, Chen Y, Liang G, Fan P and Liu W 2021 Homo-composition and hetero-structure nanocomposite Pnma Bi_2SeS_2—Pnnm Bi_2SeS_2 with high thermoelectric performance *Nat. Commun.* **12** 7192

[96] Wang S, Li H, Lu R, Zheng G and Tang X 2013 Metal nanoparticle decorated n-type Bi_2Te_3-based materials with enhanced thermoelectric performances *Nanotechnology* **24** 285702

[97] Shi X, Yang J, Salvador J R, Chi M, Cho J Y, Wang H, Bai S, Yang J, Zhang W and Chen L 2011 Multiple-filled skutterudites: high thermoelectric figure of merit through separately optimizing electrical and thermal transports *J. Am. Chem. Soc.* **133** 7837–46

[98] Rhyee J S, Lee K H, Lee S M, Cho E, Kim S Il, Lee E, Kwon Y S, Shim J H and Kotliar G 2009 Peierls distortion as a route to high thermoelectric performance in In4Se3-) crystals *Nature* **459** 965–8

[99] Chang C, Wu M, He D, Pei Y, Wu C F, Wu X, Yu H, Zhu F, Wang K, Chen Y, Huang L, Li J F, He J and Zhao L D 2018 3D charge and 2D phonon transports leading to high out-of-plane ZT in n-type SnSe crystals *Science* **360** 778–83

[100] Hsu K F, Loo S, Guo F, Chen W, Dyck J S, Uher C, Hogan T, Polychroniadis E K and Kanatzidis M G 2004 Cubic AgPbmSbTe2+m: bulk thermoelectric materials with high figure of merit *Science* **303** 818–21

[101] Perez-Marín A P, Lopeandía A F, Abad L, Ferrando-Villaba P, Garcia G, Lopez A M, Muñoz-Pascual F X and Rodríguez-Viejo J 2014 Micropower thermoelectric generator from thin Si membranes *Nano Energy* **4** 73–80
[102] Noyan I D, Dolcet M, Salleras M, Stranz A, Calaza C, Gadea G, Pacios M, Morata A, Tarancon A and Fonseca L 2019 All-silicon thermoelectric micro/nanogenerator including a heat exchanger for harvesting applications *J. Power Sources* **413** 125–33
[103] Tomita M, Oba S, Himeda Y, Yamato R, Shima K, Kumada T, Xu M, Takezawa H, Mesaki K, Tsuda K, Hashimoto S, Zhan T, Zhang H, Kamakura Y, Suzuki Y, Inokawa H, Ikeda H, Matsukawa T, Matsuki T and Watanabe T 2018 Modeling, simulation, fabrication, and characterization of a 10-μW/cm^2 class Si-nanowire thermoelectric generator for IoT applications motohiro *IEEE Trans. Electron Devices* **65** 5180–8
[104] Vullers R J M, van Schaijk R, Doms I, Van Hoof C and Mertens R 2009 Micropower energy harvesting *Solid State Electron.* **53** 684–93
[105] Zhang H, Xu T, Hashimoto S and Watanabe T 2018 The possibility of mW/cm^2-class on-chip power generation using ultrasmall si nanowire-based thermoelectric generators *IEEE Trans. Electron Devices* **65** 2016–23
[106] Hi-Z Technology, Inc. HZ-2 thermoelectric module (available at: https://hi-z.com/wp-content/uploads/2016/08/HZ-2-data-sheet.pdf)
[107] Ecogen Technology Specification of generating thermoelectric module Mars-35 (available at: https://ecogenthermoelectric.com/tpl/specification/Spec_TGM-127-1.0-0.8.pdf)
[108] Marlow Industries, Inc. Technical data sheet for RC12 - 2. 5 single - stage thermoelectric generator by II-VI MARLOW (available at: https://cdn2.hubspot.net/hubfs/547732/Data_Sheets/TG12-2.5.pdf)
[109] Böttner H, Nurnus J, Schubert A and Volkert F 2007 New high density micro structured thermogenerators for stand alone sensor systems *2007 26th Int. Conf. on Thermoelectrics* (*Jeju, Korea (South)*, *2007*) pp 306–9
[110] Zhang W, Yang J and Xu D 2016 A high power density micro-thermoelectric generator fabricated by an integrated bottom-up approach *J. Microelectromech. Syst.* **25** 744–9
[111] Roth R, Rostek R, Cobry K, Kohler C, Groh M and Woias P 2014 Design and characterization of micro thermoelectric cross-plane generators with electroplated Bi_2Te_3, SbxTey, and reflow soldering *J. Microelectromech. Syst.* **23** 961–71
[112] Curtin B M, Fang E W and Bowers J E 2012 Highly ordered vertical silicon nanowire array composite thin films for thermoelectric devices *J. Electron. Mater.* **41** 887–94
[113] Li Y, Buddharaju K, Singh N, Lo G Q and Lee S J 2011 Chip-level thermoelectric power generators based on high-density silicon nanowire array prepared with top-down CMOS technology *IEEE Electron Device Lett.* **32** 674–6
[114] Yang S M, Cong M and Lee T 2011 Application of quantum well-like thermocouple to thermoelectric energy harvester by BiCMOS process *Sens. Actuators* A **166** 117–24
[115] Yu X, Wang Y, Liu Y, Li T, Zhou H, Gao X, Feng F, Roinila T and Wang Y 2012 CMOS MEMS-based thermoelectric generator with an efficient heat dissipation path *J. Micromech. Microeng.* **22** 105011
[116] Noyan I D, Gadea G, Salleras M, Pacios M, Calaza C, Stranz A, Dolcet M, Morata A, Tarancon A and Fonseca L 2019 SiGe nanowire arrays based thermoelectric microgenerator *Nano Energy* **57** 492–9
[117] Sun Y, Sheng P, Di C, Jiao F, Xu W, Qiu D and Zhu D 2012 Organic thermoelectric materials and devices based on p- and n-type poly(metal 1,1,2,2-ethenetetrathiolate)s *Adv. Mater.* **24** 932–7
[118] Wang L, Zhang Z, Geng L, Yuan T, Liu Y, Guo J, Fang L, Qiu J and Wang S 2018 Solution-printable fullerene/TiS_2 organic/inorganic hybrids for high-performance flexible n-type thermoelectrics *Energy Environ. Sci.* **11** 1307–17
[119] Erturk A and Inman D J 2011 *Piezoelectric Energy Harvesting* (New York: Wiley)
[120] Priya S 2007 Advances in energy harvesting using low profile piezoelectric transducers *J. Electroceramics* **19** 165–82
[121] Li H, Tian C and Deng Z D 2014 Energy harvesting from low frequency applications using piezoelectric materials *Appl. Phys. Rev.* **1** 041301
[122] Caliò R, Rongala U B, Camboni D, Milazzo M, Stefanini C, de Petris G and Oddo C M 2014 Piezoelectric energy harvesting solutions *Sensors* **14** 4755–90
[123] Safaei M, Sodano H A and Anton S R 2019 A review of energy harvesting using piezoelectric materials: state-of-the-art a decade later (2008-2018) *Smart Mater. Struct.* **28** 113001
[124] Priya S, Song H-C, Zhou Y, Varghese R, Chopra A, Kim S-G, Kanno I, Wu L, Ha D S, Ryu J and Polcawich R G 2019 A review on piezoelectric energy harvesting: materials, methods, and circuits *Energy Harvest. Syst.* **4** 3–39
[125] Kim H, Priya S, Stephanou H and Uchino K 2007 Consideration of impedance matching techniques for efficient piezoelectric energy harvesting *IEEE Trans. Ultrason. Ferroelectr. Freq. Control* **54** 1851–8
[126] Li F, Lin D, Chen Z, Cheng Z, Wang J, Li C, Xu Z, Huang Q, Liao X, Chen L Q, Shrout T R and Zhang S 2018 Ultrahigh piezoelectricity in ferroelectric ceramics by design *Nat. Mater.* **17** 349–54
[127] Nataf G F, Guennou M, Gregg J M, Meier D, Hlinka J, Salje E K H and Kreisel J 2020 Domain-wall engineering and topological defects in ferroelectric and ferroelastic materials *Nat. Rev. Phys.* **2** 634–48
[128] Damjanovic D, Klein N, Li J and Porokhonskyy V 2010 What can be expected from lead-free piezoelectric materials? *Funct. Mater. Lett.* **3** 5–13
[129] De Jong M, Chen W, Geerlings H, Asta M and Persson K A 2015 A database to enable discovery and design of piezoelectric materials *Sci. Data* **2** 1–13
[130] Choudhary K, Garrity K F, Sharma V, Biacchi A J, Hight Walker A R and Tavazza F 2020 High-throughput density functional perturbation theory and machine learning predictions of infrared, piezoelectric, and dielectric responses *npj Comput. Mater.* **6** 1–13
[131] Liu S and Cohen R E 2017 Origin of negative longitudinal piezoelectric effect *Phys. Rev. Lett.* **119** 207601
[132] Shaw T M, Trolier-Mckinstry S and McIntyre P C 2000 The properties of ferroelectric films *Annu. Rev. Mater. Sci.* **30** 263–98
[133] Schlom D G, Chen L, Eom C, Rabe K M, Streiffer S K and Triscone J 2007 Strain tuning of ferroelectric thin films *Annu. Rev. Mater. Res.* **37** 589–626
[134] Hu J M, Chen L Q and Nan C W 2016 Multiferroic heterostructures integrating ferroelectric and magnetic materials *Adv. Mater.* **28** 15–39
[135] Gao W, Zhu Y, Wang Y, Yuan G and Liu J M 2020 A review of flexible perovskite oxide ferroelectric films and their application *J. Mater.* **6** 1–16
[136] Chen X, Han X and Shen Q D 2017 PVDF-based ferroelectric polymers in modern flexible electronics *Adv. Electron. Mater.* **3** 1600460
[137] Barkas D A, Psomopoulos C S, Papageorgas P, Kalkanis K, Piromalis D and Mouratidis A 2019 Sustainable energy harvesting through triboelectric nano—generators: a review of current status and applications *Energy Proc.* **157** 999–1010

[138] Song M, Zhang Y, Peng M and Zhai J 2014 Low frequency wideband nano generators for energy harvesting from natural environment *Nano Energy* **6** 66–72
[139] Ramsay M J and Clark W W 2001 Piezoelectric energy harvesting for bio-MEMS applications *Proc. SPIE 4332, Smart Structures and Materials 2001: Industrial and Commercial Applications of Smart Structures Technologies* (*14 June 2001*) vol 4332 pp 429–38
[140] Zhou D, Wang F, Luo L, Chen J, Ge W, Zhao X and Luo H 2008 Characterization of complete electromechanical constants of rhombohedral 0.72Pb($Mg_{1/3}Nb_{2/3}$)-0.28$PbTiO_3$ single crystals *J. Phys. D: Appl. Phys.* **41** 185402
[141] Amin A, McLaughlin E, Robinson H and Ewart L 2007 Mechanical and thermal transitions in morphotropic PZN-PT and PMN-PT single crystals and their implication for sound projectors *IEEE Trans. Ultrason. Ferroelectr. Freq. Control* **54** 1090–5
[142] Yin J, Jiang B and Cao W 2000 Elastic, piezoelectric, and dielectric properties of 0.955pb(zn1/3nb2/3)o3-0.45pbtio3 single crystal with designed multidomains *IEEE Trans. Ultrason. Ferroelectr. Freq. Control* **47** 285–91
[143] *Technical Publication TP-238 Piezoelectricity* (available at: www.ultrasonic-resonators.org/misc/references/articles/Morgan_Technical_Publication_TP-221__%27Power_Capacities_of_Piezoelectric_Ceramics_in_Sonar_Type_Acoustic_Transducers%27.pdf)
[144] Zheng L, Huo X, Wang R, Wang J, Jiang W and Cao W 2013 Large size lead-free (Na,K)(Nb,Ta)O_3 piezoelectric single crystal: growth and full tensor properties *CrystEngComm* **15** 7718–22
[145] Ul R, Rouffaud R, Tran-Huu-Hue L P, Levassort F, Pham-Thi M and Bantignies C 2017 Complete electroelastic set of co doped barium titanate for transducer applications *2017 IEEE Int. Ultrasonics Symposium (IUS)* (*Washington, DC, USA, 2017*) (https://doi.org/10.1109/ULTSYM.2017.8091772)
[146] Roundy S and Wright P K 2004 A piezoelectric vibration based generator for wireless electronics *Smart Mater. Struct.* **13** 1131–42
[147] Ren B, Or S W, Zhao X and Luo H 2010 Energy harvesting using a modified rectangular cymbal transducer based on 0.71Pb($Mg_{1/3}Nb_{2/3}$)O_3-0.29$PbTiO_3$ single crystal *J. Appl. Phys.* **107** 034501
[148] Sessler G M, Pondrom P and Zhang X 2016 Stacked and folded piezoelectrets for vibration-based energy harvesting *Phase Transit.* **89** 667–77
[149] Xu C, Ren B, Di W, Liang Z, Jiao J, Li L, Li L, Zhao X, Luo H and Wang D 2012 Cantilever driving low frequency piezoelectric energy harvester using single crystal material 0.71Pb($Mg_{1/3}Nb_{2/3}$)O_3-0.29$PbTiO_3$ *Appl. Phys. Lett.* **101** 033502
[150] Li P, Gao S and Cai H 2015 Modeling and analysis of hybrid piezoelectric and electromagnetic energy harvesting from random vibrations *Microsyst. Technol.* **21** 401–14
[151] Zi Y, Lin L, Wang J, Wang S, Chen J, Fan X, Yang P K, Yi F and Wang Z L 2015 Triboelectric-pyroelectric-piezoelectric hybrid cell for high-efficiency energy-harvesting and self-powered sensing *Adv. Mater.* **27** 2340–7
[152] Yang Y, Shen Q, Jin J, Wang Y, Qian W and Yuan D 2014 Rotational piezoelectric wind energy harvesting using impact-induced resonance *Appl. Phys. Lett.* **105** 053901
[153] Gilbert J M and Balouchi F 2008 Comparison of energy harvesting systems for wireless sensor networks *Int. J. Autom. Comput.* **5** 334–47
[154] Cross L E 2006 Flexoelectric effects: charge separation in insulating solids subjected to elastic strain gradients *J. Mater. Sci.* **41** 53–63
[155] Zubko P, Catalan G and Tagantsev A K 2013 Flexoelectric effect in solids *Annu. Rev. Mater. Res.* **43** 387–421
[156] Zhang X, Liu J, Chu M and Chu B 2016 Flexoelectric piezoelectric metamaterials based on the bending of ferroelectric ceramic wafers *Appl. Phys. Lett.* **109** 072903
[157] Bhaskar U K, Banerjee N, Abdollahi A, Wang Z, Schlom D G, Rijnders G and Catalan G 2016 A flexoelectric microelectromechanical system on silicon *Nat. Nanotechnol.* **11** 263–6
[158] Gao P, Yang S, Ishikawa R, Li N, Feng B, Kumamoto A, Shibata N, Yu P and Ikuhara Y 2018 Atomic-scale measurement of flexoelectric polarization at $SrTiO_3$ dislocations *Phys. Rev. Lett.* **120** 267601
[159] Yokota H, Usami H, Haumont R, Hicher P, Kaneshiro J, Salje E K H and Uesu Y 2014 Direct evidence of polar nature of ferroelastic twin boundaries in CaTiO3 obtained by second harmonic generation microscope *Phys. Rev.* B **89** 144109
[160] Scott J F, Salje E K H and Carpenter M A 2012 Domain wall damping and elastic softening in $SrTiO_3$: evidence for polar twin walls *Phys. Rev. Lett.* **109** 187601
[161] Frenkel Y, Haham N, Shperber Y, Bell C, Xie Y, Chen Z, Hikita Y, Hwang H Y, Salje E K H and Kalisky B 2017 Imaging and tuning polarity at $SrTiO_3$ domain walls *Nat. Mater.* **16** 1203–8
[162] Ma H J H, Scharinger S, Zeng S W, Kohlberger D, Lange M, Stöhr A, Wang X R, Venkatesan T, Kleiner R, Scott J F, Coey J M D, Koelle D and Ariando 2016 Local electrical imaging of tetragonal domains and field-induced ferroelectric twin walls in conducting $SrTiO_3$ *Phys. Rev. Lett.* **116** 257601
[163] Yun S, Song K, Chu K, Hwang S Y, Kim G Y, Seo J, Woo C S, Choi S Y and Yang C H 2020 Flexopiezoelectricity at ferroelastic domain walls in WO_3 films *Nat. Commun.* **11** 4898
[164] Wang K F and Wang B L 2018 Energy gathering performance of micro/nanoscale circular energy harvesters based on flexoelectric effect *Energy* **149** 597–606
[165] Huang W, Kim K, Zhang S, Yuan F G and Jiang X 2011 Scaling effect of flexoelectric (Ba,Sr)TiO_3 microcantilevers *Phys. Status Solidi* **5** 350–2
[166] Chen W, Liang X and Shen S 2021 Forced vibration of piezoelectric and flexoelectric Euler–Bernoulli beams by dynamic Green's functions *Acta Mech.* **232** 449–60
[167] Chu B and Salem D R 2012 Flexoelectricity in several thermoplastic and thermosetting polymers *Appl. Phys. Lett.* **101** 103905
[168] Poddar S and Ducharme S 2013 Measurement of the flexoelectric response in ferroelectric and relaxor polymer thin films *Appl. Phys. Lett.* **103** 202901
[169] Maranganti R and Sharma P 2009 Atomistic determination of flexoelectric properties of crystalline dielectrics *Phys. Rev.* B **80** 054109
[170] Zubko P, Catalan G, Buckley A, Welche P R L and Scott J F 2007 Strain-gradient-induced polarization in $SrTiO_3$ single crystals *Phys. Rev. Lett.* **99** 167601
[171] Zubko P, Catalan G, Buckley A, Welche P R L and Scott J F 2008 Erratum: strain-gradient-induced polarization in $srTiO_3$ single crystals (Physical Review Letters (2007) 99 (167601)) *Phys. Rev. Lett.* **100** 199906
[172] Ponomareva I, Tagantsev A K and Bellaiche L 2012 Finite-temperature flexoelectricity in ferroelectric thin films from first principles *Phys. Rev.* B **85** 104101
[173] Ma W and Cross L E 2005 Flexoelectric effect in ceramic lead zirconate titanate *Appl. Phys. Lett.* **86** 072905
[174] Ma W and Cross L E 2001 Observation of the flexoelectric effect in relaxor Pb($Mg_{1/3}Nb_{2/3}$)O_3 ceramics *Appl. Phys. Lett.* **78** 2920–1

[175] Ma W and Cross L E 2006 Flexoelectricity of barium titanate *Appl. Phys. Lett.* **88** 232902
[176] Baskaran S, He X, Chen Q and Fu J Y 2011 Experimental studies on the direct flexoelectric effect in α -phase polyvinylidene fluoride films *Appl. Phys. Lett.* **98** 242901
[177] Zhou Y, Liu J, Hu X, Chu B, Chen S and Salem D 2017 Flexoelectric effect in PVDF-based polymers *IEEE Trans. Dielectr. Electr. Insul.* **24** 727–31
[178] Lu J, Lv J, Liang X, Xu M and Shen S 2016 Improved approach to measure the direct flexoelectric coefficient of bulk polyvinylidene fluoride *J. Appl. Phys.* **119** 094104
[179] Qi Y, Kim J, Nguyen T D, Lisko B, Purohit P K and McAlpine M C 2011 Enhanced piezoelectricity and stretchability in energy harvesting devices fabricated from buckled PZT ribbons *Nano Lett.* **11** 1331–6
[180] Kodali P, Saravanavel G and Sambandan S 2017 Crumpling for energy: modeling generated power from the crumpling of polymer piezoelectric foils for wearable electronics *Flex. Print. Electron.* **2** 035005
[181] Zhou W, Chen P, Pan Q, Zhang X and Chu B 2015 Lead-free metamaterials with enormous apparent piezoelectric response *Adv. Mater.* **27** 6349–55
[182] Wang B, Yang S and Sharma P 2019 Flexoelectricity as a universal mechanism for energy harvesting from crumpling of thin sheets *Phys. Rev.* B **100** 035438
[183] Majdoub M S, Sharma P and Çağin T 2008 Dramatic enhancement in energy harvesting for a narrow range of dimensions in piezoelectric nanostructures *Phys. Rev.* B **78** 121407(R)
[184] Yan Z 2017 Modeling of a nanoscale flexoelectric energy harvester with surface effects *Physica E: Low-dimensional Systems and Nanostructures* **88** 125–32
[185] Liang X, Zhang R, Hu S and Shen S 2017 Flexoelectric energy harvesters based on Timoshenko laminated beam theory *J. Intell. Mater. Syst. Struct.* **28** 2064–73
[186] Wang K F, Wang B L and Zeng S 2018 Analysis of an array of flexoelectric layered nanobeams for vibration energy harvesting *Compos. Struct.* **187** 48–57
[187] Javvaji B, Zhang R, Zhuang X and Park H S 2021 Flexoelectric electricity generation by crumpling graphene *J. Appl. Phys.* **129** 225107
[188] Bhaskar U K, Banerjee N, Abdollahi A, Solanas E, Rijnders G and Catalan G 2016 Flexoelectric MEMS: towards an electromechanical strain diode *Nanoscale* **8** 1293–8
[189] Ji D, Cai S, Paudel T R, Sun H, Zhang C, Han L, Wei Y, Zang Y, Gu M, Zhang Y, Gao W, Huyan H, Guo W, Wu D, Gu Z, Tsymbal E Y, Wang P, Nie Y and Pan X 2019 Freestanding crystalline oxide perovskites down to the monolayer limit *Nature* **570** 87–90
[190] Cai S, Lun Y, Ji D, Han L, Guo C, Zang Y, Gao S, Wei Y, Gu M, Zhang C, Gu Z, Wang X, Addiego C, Fang D, Nie Y, Hong J, Wang P and Pan X 2020 Giant polarization and abnormal flexural deformation in bent freestanding perovskite oxides (arXiv:2009.03177 [cond-mat.mtrl-sci])
[191] Kumar A, Chauhan A, Vaish R, Kumar R and Jain S C 2018 Structural optimization for wideband flexoelectric energy harvester using bulk paraelectric $Ba_{0.6}Sr_{0.4}TiO_3$ *J. Electron. Mater.* **47** 394–401
[192] Kumar A, Sharma A, Vaish R, Kumar R and Jain S C 2018 A numerical study on flexoelectric bistable energy harvester *Appl. Phys.* A **124** 483
[193] De Pasquale G, Somà A and Fraccarollo F 2013 Comparison between piezoelectric and magnetic strategies for wearable energy harvesting *J. Phys.: Conf. Ser.* **476** 012097
[194] Foisal A R M and Chung G S 2012 Design and analysis of a vibration-driven AA size electromagnetic energy harvester using magnetic spring *Trans. Electr. Electron. Mater.* **13** 125–8
[195] Masoumi M and Wang Y 2016 Repulsive magnetic levitation-based ocean wave energy harvester with variable resonance: modeling, simulation and experiment *J. Sound Vib.* **381** 192–205
[196] Morais R, Silva N M, Santos P M, Frias C M, Ferreira J A F, Ramos A M, Simões J A O, Baptista J M R and Reis M C 2011 Double permanent magnet vibration power generator for smart hip prosthesis *Sens. Actuators* A **172** 259–68
[197] Apo D J and Priya S 2014 High power density levitation-induced vibration energy harvester *Energy Harvest. Syst.* **1** 79–88
[198] Imbaquingo C 2021 Energy harvesting with permanent magnets *PhD dissertation* (Technical University of Denmark)
[199] Cheng S, Wang N and Arnold D P 2007 Modeling of magnetic vibrational energy harvesters using equivalent circuit representations *J. Micromech. Microeng.* **17** 2328–35
[200] Mann B P and Sims N D 2009 Energy harvesting from the nonlinear oscillations of magnetic levitation *J. Sound Vib.* **319** 515–30
[201] Enrique Imbaquingo C, Beleggia M, Roberto Insinga A, R H Bahl, Mann B and Bjork R 2020 Analytical force and flux for a 1D electromagnetic vibration energy harvester *IEEE Trans. Magn.* **56** 1
[202] Carneiro P, Santos M P S d, Rodrigues A, Ferreira J A F, Simões J A O, Marques A T and Kholkin A L 2020 Electromagnetic energy harvesting using magnetic levitation architectures: a review *Appl. Energy* **260** 114191
[203] Nguyen H T, Genov D A and Bardaweel H 2020 Vibration energy harvesting using magnetic spring based nonlinear oscillators: design strategies and insights *Appl. Energy* **269** 115102
[204] Santos M P S D, Ferreira J A F, Simões J A O, Pascoal R, Torrão J, Xue X and Furlani E P 2016 Magnetic levitation-based electromagnetic energy harvesting: a semi-analytical non-linear model for energy transduction *Sci. Rep.* **6** 18579
[205] Jensen T W, Insinga A R, Ehlers J C and Bjoerk R 2021 The full phase space dynamics of a magnetically levitated electromagnetic vibration harvester *Sci. Rep.* **11** 16607
[206] Shen Y and Lu K 2020 Scavenging power from ultra-low frequency and large amplitude vibration source through a new non-resonant electromagnetic energy harvester *Energy Convers. Manage.* **222** 113233
[207] Shahosseini I and Najafi K 2015 Cylindrical halbach magnet array for electromagnetic vibration energy harvesters *2015 28th IEEE Int. Conf. on Micro Electro Mechanical Systems (MEMS)* (*Estoril, Portugal, February 2015*) pp 1051–4
[208] Yeo J, Park H, Jo J and Yang Y 2015 Multi-dimensional vibration energy harvester for efficient use in common environment *2015 IEEE SENSORS Busan, Korea (South)* pp 1–4
[209] Imbaquingo C, Bahl C, Insinga A R and Bjørk R 2022 A two-dimensional electromagnetic vibration energy harvester with variable stiffness *Appl. Energy* **325** 119650
[210] Imbaquingo C, Bahl C, Insinga A R and Bjørk R 2022 Two-dimensional elliptically shaped electromagnetic vibration energy harvester: techRxiv (https://doi.org/10.36227/techrxiv.20709031.v1)
[211] Fan K, Cai M, Liu H and Zhang Y 2019 Capturing energy from ultra-low frequency vibrations and human motion through a monostable electromagnetic energy harvester *Energy* **169** 356–68

[212] Aldawood G, Nguyen H T and Bardaweel H 2019 High power density spring-assisted nonlinear electromagnetic vibration energy harvester for low base-accelerations *Appl. Energy* **253** 113546
[213] Choi Y, Ju S, Chae S H, Jun S and Ji C-H 2015 Low-frequency vibration energy harvester using a spherical permanent magnet with controlled mass distribution *Smart Mater. Struct.* **24** 065029
[214] Hadas Z and Ondrusek C 2015 Nonlinear spring-less electromagnetic vibration energy harvesting system *Eur. Phys. J. Spec. Top.* **224** 2881–96
[215] Sato T and Igarashi H 2015 A chaotic vibration energy harvester using magnetic material *Smart Mater. Struct.* **24** 025033
[216] Gutierrez M, Shahidi A, Berdy D and Peroulis D 2015 Design and characterization of a low frequency 2-dimensional magnetic levitation kinetic energy harvester *Sens. Actuators* A **236** 1–10
[217] Palagummi S V 2015 Low frequency vibration energy harvesting using diamagnetically stabilized *PhD Thesis* North Carolina State University (ProQuest Dissertations Publishing)
[218] Khan F U and Ahmad S 2019 Flow type electromagnetic based energy harvester for pipeline health monitoring system *Energy Convers. Manage.* **200** 112089
[219] Beeby S P and O'Donnell T 2009 Electromagnetic energy harvesting *Energy Harvesting Technologies* ed S Priya and D J Inman (Boston, MA: Springer) pp 129–61
[220] Tay C J, Quan C, Lee C and Liu H 2015 Development of a micro energy harvester using multiple vibration modes *Proc. The Int. Conf. on Engineering & MIS 2015, Ser. ICEMIS'15* (New York: Association for Computing Machinery) pp 1–4
[221] Zhang Q and Kim E S 2014 Vibration energy harvesting based on magnet and coil arrays for watt-level handheld power source *Proc. IEEE* **102** 1747–61
[222] Polyzoidis C, Rogdakis K and Kymakis E 2021 Indoor perovskite photovoltaics for the internet of things-challenges and opportunities toward market uptake *Adv. Energy Mater.* **11** 2101854
[223] Ahmad F F, Ghenai C and Bettayeb M 2021 Maximum power point tracking and photovoltaic energy harvesting for internet of things: a comprehensive review *Sustain. Energy Technol. Assess.* **47** 101430
[224] Biswas S and Kim H 2020 Solar cells for indoor applications: progress and development *Polymers* **12** 1338
[225] Hou X Y, Wang Y W, Lee H K H, Datt R, Miano N U, Yan D, Li M, Zhu F R, Hou B, Tsoi W C and Li Z 2020 Indoor application of emerging photovoltaics-progress, challenges and perspectives *J. Mater. Chem.* A **8** 21503–25
[226] Xu X, Liu W, Luo X Y, Chen H B, Wei Q Y, Yuan J and Zou Y P 2021 An overview of high-performance indoor organic photovoltaics *Chem. Sus. Chem.* **14** 3428–48
[227] Venkateswararao A, Ho J K W, So S K, Liu S-W and Wong K-T 2020 Device characteristics and material developments of indoor photovoltaic devices *Mater. Sci. Eng.*R **139** 100517
[228] Luque A and Hegedus S 2003 *Handbook of Photovoltaic Science and Engineering* (Chichester: John Wiley & Sons, Ltd)
[229] Cheng P and Zhan X 2016 Stability of organic solar cells: challenges and strategies *Chem. Soc. Rev.* **45** 2544–82
[230] Manceau M, Rivaton A, Gardette J L, Guillerez S and Lemaître N 2009 The mechanism of photo- and thermooxidation of poly(3-hexylthiophene) (P3HT) reconsidered *Polym. Degrad. Stab.* **94** 898–907
[231] Bregnhøj M, Prete M, Turkovic V, Petersen A U, Nielsen M B, Madsen M and Ogilby P R 2020 Oxygen-dependent photophysics and photochemistry of prototypical compounds for organic photovoltaics: inhibiting degradation initiated by singlet oxygen at a molecular level *Methods Appl. Fluoresc.* **8** 014001
[232] Turkovic V, Prete M, Bregnhøj M, Inasaridze L, Volyniuk D, Obrezkov F A, Grazulevicius J V, Engmann S, Rubahn H G, Troshin P A, Ogilby P R and Madsen M 2019 Biomimetic approach to inhibition of photooxidation in organic solar cells using beta-carotene as an additive *ACS Appl. Mater. Interfaces* **11** 41570–9
[233] Salvador M, Gasparini N, Perea J D, Paleti S H, Distler A, Inasaridze L N, Troshin P A, Lüer L, Egelhaaf H J and Brabec C 2017 Suppressing photooxidation of conjugated polymers and their blends with fullerenes through nickel chelates *Energy Environ. Sci.* **10** 2005–16
[234] Destouesse E, Top M, Lamminaho J, Rubahn H G, Fahlteich J and Madsen M 2019 Slot-die processing and encapsulation of non-fullerene based ITO-free organic solar cells and modules *Flex. Print. Electron.* **4** 045004
[235] Ahmad J, Bazaka K, Anderson L J, White R D and Jacob M V 2013 Materials and methods for encapsulation of OPV: a review *Renew. Sustain. Energy Rev.* **27** 104–17
[236] Arredondo B, Del Pozo G, Hernández-Balaguera E, Martín D M, López González M D C, Romero B, López-Fraguas E, Vergaz R, Quintana X, Lamminaho J, Destouesse E, Ahmadpour M, Turkovic V and Madsen M 2020 Identification of degradation mechanisms in slot-die-coated nonfullerene ITO-free organic solar cells using different illumination spectra *ACS Appl. Energy Mater.* **3** 6476–85
[237] Park S and Son H J 2019 Intrinsic photo-degradation and mechanism of polymer solar cells: the crucial role of non-fullerene acceptors *J. Mater. Chem.* A **7** 25830–7
[238] Amelot D, Ahmadpour M, Ros Q, Cruguel H, Casaretto N, Cossaro A, Floreano L, Madsen M and Witkowski N 2021 Deciphering electron interplay at the fullerene/sputtered TiOx interface: a barrier-free electron extraction for organic solar cells *ACS Appl. Mater. Interfaces* **13** 19460–6
[239] Hintz H, Sessler C, Peisert H, Egelhaaf H and Chasse T 2012 Wavelength-dependent pathways of poly-3-hexylthiophene photo-oxidation *Chem. Mater.* **24** 2739–43
[240] Ho J K W, Yin H and So S K 2020 From 33% to 57%—an elevated potential of efficiency limit for indoor photovoltaics *J. Mater. Chem.* A **8** 1717–23
[241] Rühle S 2016 Tabulated values of the Shockley–Queisser limit for single junction solar cells *Sol. Energy* **130** 139–47
[242] Li B, Hou B and Amaratunga G A J 2021 Indoor photovoltaics, the next big trend in solution-processed solar cells *InfoMat* **3** 445–59
[243] Yang P C, Chan I M, Lin C H and Chang Y L 2011 Thin film solar cells for indoor use *2011 37th IEEE Photovoltaic Specialists Conf. (Seattle, WA, USA, 2011)* (IEEE) pp 696–8
[244] Ma L-K, Chen Y, Chow P C Y, Zhang G, Huang J, Ma C, Zhang J, Yin H, Hong Cheung A M, Wong K S, So S K and Yan H 2020 High-efficiency indoor organic photovoltaics with a band-aligned interlayer *Joule* **4** 1486–500
[245] He X, Chen J, Ren X, Zhang L, Liu Y, Feng J, Fang J, Zhao K and Liu S 2021 40.1% record low-light solar-cell efficiency by holistic trap-passivation using micrometer-thick perovskite film *Adv. Mater.* **33** 2100770
[246] Meyer B K, Polity A, Reppin D, Becker M, Hering P, Klar PJ, Sander T, Reindl C, Benz J, Eickhoff M, Heiliger C, Heinemann M, Bläsing J, Krost A, Shokovets S, Müller C and Ronning C 2012 Binary copper oxide semiconductors: from materials towards devices *Phys. Status Solidi B* **249** 1487–509

[247] Miller E L, Paluselli D, Marsen B and Rocheleau R E 2004 Low-temperature reactively sputtered iron oxide for thin film devices *Thin Solid Films* **466** 307–13
[248] Al-Kuhaili M F, Saleem M and Durrani S M A 2012 Optical properties of iron oxide (α-Fe_2O_3) thin films deposited by the reactive evaporation of iron *J. Alloys Compd.* **521** 178–82
[249] Peng H W, Ndione P F, Ginley D S, Zakutayev A and Lany S 2015 Design of semiconducting tetrahedral Mn1-xZnxO alloys and their application to solar water splitting *Phys. Rev.* X **5** 21016
[250] Ho C Y, Liu C P, Chen Y C, Huang Z Q, Chuang F C and Yu K M 2019 Effects of oxygen stoichiometry on the phase stability of sputter-deposited $Cd_xZn_{1-x}O$ alloys *Phys. Rev. Mater.* **3** 74605
[251] Ma X, Chen P, Zhang R and Yang D 2011 Optical properties of sputtered hexagonal CdZnO films with band gap energies from 1.8 to 3.3eV *J. Alloys Compd.* **509** 6599–602
[252] Detert D M, Lim S H M, Tom K, Luce A V, Anders A, Dubon O D, Yu K M and Walukiewicz W 2013 Crystal structure and properties of $Cd_xZn_{1-x}O$ alloys across the full composition range *Appl. Phys. Lett.* **102** 232103
[253] Ishihara J, Nakamura A, Shigemori S, Aoki T and Temmyo J 2006 Zn1−xCdxO systems with visible band gaps *Appl. Phys. Lett.* **89** 91914
[254] Liu Q, Jiang Y, Jin K, Qin J, Xu J, Li W, Xiong J, Liu J, Xiao Z, Sun K, Yang S, Zhang X and Ding L 2020 18% efficiency organic solar cells *Sci. Bull.* **65** 272–5
[255] Zhang Y, Duan C and Ding L 2020 Indoor organic photovoltaics *Sci. Bull.* **65** 2040–2
[256] Jahandar M, Kim S and Lim D C 2021 Indoor organic photovoltaics for self-sustaining IoT devices: progress, challenges and practicalization *Chem. Sus. Chem.* **14** 3449–74
[257] Mainville M and Leclerc M 2020 Recent progress on indoor organic photovoltaics: from molecular design to production scale *ACS Energy Lett.* **5** 1186–97
[258] Saeed M A, Kim S H, Kim H, Liang J, Woo H Y, Kim T G, Yan H and Shim J W 2021 Indoor organic photovoltaics: optimal cell design principles with synergistic parasitic resistance and optical modulation effect *Adv. Energy Mater.* **11** 2003103
[259] Opoku H, Kim Y H, Lee J H, Ahn H, Lee J J, Baek S W and Jo J W 2021 A tailored graft-type polymer as a dopant-free hole transport material in indoor perovskite photovoltaics *J. Mater. Chem.* A **9** 15294–300
[260] Mahapatra A, Prochowicz D, Tavakoli M M, Trivedi S, Kumar P and Yadav P 2020 A review of aspects of additive engineering in perovskite solar cells *J. Mater. Chem.* A **8** 27–54
[261] Wang M, Wang Q, Zhao J, Xu Y, Wang H, Zhou X, Yang S, Ci Z and Jin Z 2022 Low-trap-density CsPbX3 film for high-efficiency indoor photovoltaics *ACS Appl. Mater. Interfaces* **14** 11528–37
[262] Yang F, Su Z, Pascual J, Li M, Liu H, Qin C, Gao X, Li G, Li Z and Wang Z 2022 Enhancement of exciton separation in indoor perovskite photovoltaics by employing conjugated organic chromophores *J. Power Sources* **520** 230785
[263] Jin I S, Parida B and Jung J W 2022 Simultaneously enhanced efficiency and ambient stability of inorganic perovskite solar cells by employing tetramethylammonium chloride additive in CsPbI2Br *J. Mater. Sci. Technol.* **102** 224–31
[264] Prasad J, Shao Z, Machhi H K, Sharma D S, Patel V K, Pang S, Cui G and Soni S S 2021 'V' shape A–D–A-type designed small hole conductors for efficient indoor and outdoor staging from solid dye-sensitized solar cells and perovskite solar cells *Sol. RRL* **5** 2100206
[265] Singh R, Parashar M, Sandhu S, Yoo K and Lee J J 2021 The effects of crystal structure on the photovoltaic performance of perovskite solar cells under ambient indoor illumination *Sol. Energy* **220** 43–50
[266] Wang K L, Li X M, Lou Y H, Li M and Wang Z K 2021 CsPbBrI2 perovskites with low energy loss for high-performance indoor and outdoor photovoltaics *Sci. Bull.* **66** 347–53
[267] Bi Z, Zhang S, Thandapani M, Zhu Y, Zheng Y, Liem N Q, Xiao X, Xu G, Guerrero A and Xu X 2021 High shunt resistance SnO_2-PbO electron transport layer for perovskite solar cells used in low lighting applications *Adv. Sustain. Syst.* **5** 2100120
[268] Castro-Hermosa S, Lucarelli G, Top M, Fahland M, Fahlteich J and Brown T M 2020 Perovskite photovoltaics on roll-to-roll coated ultra-thin glass as flexible high-efficiency indoor power generators *Cell Rep. Phys. Sci.* **1** 100045
[269] Lee J H, Kang H C, Lee J J and Jo J W 2022 Concentrated perovskite photovoltaics enable minimization of energy loss below 0.5 eV under artificial light-emitting diode illumination *Int. J. Energy Res.* **46** 5260–8
[270] Chen C H, Su Z H, Lou Y H, Yu Y J, Wang K L, Liu G L, Shi Y R, Chen J, Cao J J, Zhang L, Gao X Y and Wang Z K 2022 Full-dimensional grain boundary stress release for flexible perovskite indoor photovoltaics *Adv. Mater.* **34** 2200320
[271] Jiang S, Bai Y, Xu Z, Wang F, Xia L, Yang Y, Li C and Tan Z 2022 Efficient perovskite indoor photovoltaics with open-circuit voltage of 1.15 V via collaborative optimization of CsPbI 2 Br layer and hole transport layer *Small Methods* **6** 2200624
[272] Cho Y, Kumari T, Jeong S, Lee S M, Jeong M, Lee B, Oh J, Zhang Y, Huang B, Chen L and Yang C 2020 Guest-oriented non-fullerene acceptors for ternary organic solar cells with over 16.0% and 22.7% efficiencies under one-sun and indoor light *Nano Energy* **75** 104896
[273] Cui Y, Wang Y, Bergqvist J, Yao H, Xu Y, Gao B, Yang C, Zhang S, Inganäs O, Gao F and Hou J 2019 Wide-gap non-fullerene acceptor enabling high-performance organic photovoltaic cells for indoor applications *Nat. Energy* **4** 768–75
[274] Park S, Ahn H, Kim J Y, Park J B, Kim J, Im S H and Son H J 2020 High-performance and stable nonfullerene acceptor-based organic solar cells for indoor to outdoor light *ACS Energy Lett.* **5** 170–9
[275] Miranda B H *et al* 2021 Efficient fully roll-to-roll coated encapsulated organic solar module for indoor applications *Sol. Energy* **220** 343–53
[276] Bai F, Zhang J, Zeng A, Zhao H, Duan K, Yu H, Cheng K, Chai G, Chen Y, Liang J, Ma W and Yan H 2021 A highly crystalline non-fullerene acceptor enabling efficient indoor organic photovoltaics with high EQE and fill factor *Joule* **5** 1231–45
[277] Saeed M A, Cheng S, Biswas S, Kim S H, Kwon S K, Kim H, Kim Y H and Shim J W 2022 Remarkably high performance of organic photovoltaic devices with 3,9-bis(2-methylene- (3-(1,1-dicyanomethylene)-indanone))-5,5,11,11-tetrakis(4-hexyl meta-phenyl)-dithieno[2,3-d:2′,3′-d']-s-indaceno[1,2-b:5,6-b']dithiophene)- ethylhexyloxy] photoactive ac *J. Power Sources* **518** 230782
[278] Yang Z, Guan C, Jiang X, Zhang G, Xie C, Liu C, Xiao C and Li W 2022 High-performance indoor organic solar cells based on a double-cable conjugated polymer *Sol. RRL* **6** 2100981
[279] Huang J, Ren Z, Zhang Y, Liu K, Zhang H, Tang H, Yan C, Zheng Z and Li G 2021 Stretchable ITO-free organic solar cells with intrinsic anti-reflection substrate for high-efficiency outdoor and indoor energy harvesting *Adv. Funct. Mater.* **31** 2010172
[280] Elahi H, Munir K, Eugeni M, Atek S and Gaudenzi P 2020 Energy harvesting towards self-powered IoT devices *Energies* **13** 5528
[281] Gurung A, Reza K M, Mabrouk S, Bahrami B, Pathak R, Lamsal B S, Rahman S I, Ghimire N, Bobba R S, Chen K, Pokharel J, Baniya A, Laskar M A R, Liang M, Zhang W, Zhang W H, Yang S, Xu K and Qiao Q 2020 Rear-illuminated perovskite photorechargeable lithium battery *Adv. Funct. Mater.* **30** 2001865

[282] Fojtik M, Kim D, Chen G, Lin Y S, Fick D, Park J, Seok M, Cn M Ter, Foo Z, Blaauw D and Sylvester D 2013 A millimeter-scale energy-autonomous sensor system with stacked battery and solar cells *IEEE J. Solid-State Circuits* **48** 801–13
[283] Wang Y, Chen C, Xie H, Gao T, Yao Y, Pastel G, Han X, Li Y, Zhao J, Fu K K and Hu L 2017 3D-printed all-fiber Li-ion battery toward wearable energy storage *Adv. Funct. Mater.* **27** 1703140
[284] Yang Y 2020 A mini-review: emerging all-solid-state energy storage electrode materials for flexible devices *Nanoscale* **12** 3560–73
[285] Whitacre J F, West W C, Ratnakumar B V, Brandon E and Surampudi S 2001 Low process temperature nanocrystalline $LiCoO_2$ thin film cathodes *Power Sources for the New Millennium: Proc. Int. Symp.* ed M A Ryan, S Surampudi and M Jain (New Jersey: The Electrochemical Society, Inc) pp 257–65
[286] Lin J, Lin L, Qu S, Deng D, Wu Y, Yan X, Xie Q, Wang L and Peng D 2022 Promising electrode and electrolyte materials for high-energy-density thin-film lithium batteries *Energy Environ. Mater.* **5** 133–56
[287] Balaish M, Gonzalez-Rosillo J C, Kim K J, Zhu Y, Hood Z D and Rupp J L M 2021 Processing thin but robust electrolytes for solid-state batteries *Nat. Energy* **6** 227–39
[288] Fenech M and Sharma N 2020 Pulsed laser deposition-based thin film microbatteries *Chem. Asian J.* **15** 1829–47
[289] Zhao W, Yi J, He P and Zhou H 2019 Solid-state electrolytes for lithium-ion batteries: fundamentals, challenges and perspectives *Electrochem. Energy Rev.* **2** 574–605
[290] Zheng F, Kotobuki M, Song S, Lai M O and Lu L 2018 Review on solid electrolytes for all-solid-state lithium-ion batteries *J. Power Sources* **389** 198–213
[291] Nowak S, Berkemeier F and Schmitz G 2015 Ultra-thin LiPON films—fundamental properties and application in solid state thin film model batteries *J. Power Sources* **275** 144–50
[292] DeWees R and Wang H 2019 Synthesis and properties of NaSICON-type LATP and LAGP solid electrolytes *ChemSusChem* **12** 3713–25
[293] Shan Y J, Chen L, Inaguma Y, Itoh M and Nakamura T 1995 Oxide cathode with perovskite structure for rechargeable lithium batteries *J. Power Sources* **54** 397–402
[294] Zhu Y, He X and Mo Y 2015 Origin of outstanding stability in the lithium solid electrolyte materials: insights from thermodynamic analyses based on first-principles calculations *ACS Appl. Mater. Interfaces* **7** 23685–93
[295] Sastre J, Futscher M H, Pompizi L, Aribia A, Priebe A, Overbeck J, Stiefel M, Tiwari A N and Romanyuk Y E 2021 Blocking lithium dendrite growth in solid-state batteries with an ultrathin amorphous Li-La-Zr-O solid electrolyte *Commun. Mater.* **2** 76
[296] Liang X, Tan F, Wei F and Du J 2019 Research progress of all solid-state thin film lithium battery *IOP Conf. Ser.: Earth Environ. Sci.* **218** 012138
[297] Yi E, Wang W, Kieffer J and Laine R M 2017 Key parameters governing the densification of cubic-Li7La3Zr2O12 Li+ conductors *J. Power Sources* **352** 156–64
[298] Kato Y, Hori S, Saito T, Suzuki K, Hirayama M, Mitsui A, Yonemura M, Iba H and Kanno R 2016 High-power all-solid-state batteries using sulfide superionic conductors *Nat. Energy* **1** 16030
[299] Tsukasaki H, Igarashi K, Wakui A, Yaguchi T, Nakajima H, Kimura T, Sakuda A, Tatsumisago M, Hayashi A and Mori S 2021 *In situ* observation of the deterioration process of sulfide-based solid electrolytes using airtight and air-flow TEM systems *Microscopy* **70** 519–25
[300] Wang L, Chen B, Ma J, Cui G and Chen L 2018 Reviving lithium cobalt oxide-based lithium secondary batteries-toward a higher energy density *Chem. Soc. Rev.* **47** 6505–602
[301] Ren X, Zhang X, Shadike Z, Zou L, Jia H, Cao X, Engelhard M H, Matthews B E, Wang C, Arey B W, Yang X Q, Liu J, Zhang J G and Xu W 2020 Designing advanced *in situ* electrode/electrolyte interphases for wide temperature operation of 4.5 V Li||LiCoO2 batteries *Adv. Mater.* **32** 2004898
[302] Yi T F, Mei J and Zhu Y R 2016 Key strategies for enhancing the cycling stability and rate capacity of LiNi0.5Mn1.5O4 as high-voltage cathode materials for high power lithium-ion batteries *J. Power Sources* **316** 85–105
[303] Chen J, Huang Z, Zeng W, Cao F, Ma J, Tian W and Mu S 2021 Synthesis, modification, and lithium-storage properties of spinel $LiNi_{0.5}Mn_{1.5}O_4$ *ChemElectroChem* **8** 608–24
[304] Konishi H, Suzuki K, Taminato S, Kim K, Zheng Y, Kim S, Lim J, Hirayama M, Son J Y, Cui Y and Kanno R 2014 Effect of surface Li_3PO_4 coating on $LiNi_{0.5}Mn_{1.5}O_4$ epitaxial thin film electrodes synthesized by pulsed laser deposition *J. Power Sources* **269** 293–8
[305] Li J, Ma C, Chi M, Liang C and Dudney N J 2015 Solid electrolyte: the key for high-voltage lithium batteries *Adv. Energy Mater.* **5** 1401408
[306] Yubuchi S, Ito Y, Matsuyama T, Hayashi A and Tatsumisago M 2016 5V class LiNi0.5Mn1.5O4 positive electrode coated with Li_3PO_4 thin film for all-solid-state batteries using sulfide solid electrolyte *Solid State Ion.* **285** 79–82
[307] Song J, Shin D W, Lu Y, Amos C D, Manthiram A and Goodenough J B 2012 Role of oxygen vacancies on the performance of $Li[Ni_{0.5-x}Mn_{1.5+x}]O_4$ ($x = 0$, 0.05, and 0.08) spinel cathodes for lithium-ion batteries *Chem. Mater.* **24** 3101–9
[308] Nishio K, Nakamura N, Horiba K, Kitamura M, Kumigashira H, Shimizu R and Hitosugi T 2020 Low resistance at $LiNi_{1/3}Mn_{1/3}Co_{1/3}O_2$ and Li_3PO_4 interfaces *Appl. Phys. Lett.* **116** 053901
[309] Martha S K, Nanda J, Kim Y, Unocic R R, Pannala S and Dudney N J 2013 Solid electrolyte coated high voltage layered-layered lithium-rich composite cathode: $li_{1.2}Mn_{0.525}Ni_{0.175}Co_{0.1}O_2$ *J. Mater. Chem.* A **1** 5587–95
[310] Yan B, Liu J, Song B, Xiao P and Lu L 2013 Li-rich thin film cathode prepared by pulsed laser deposition *Sci. Rep.* **3** 3332
[311] Yim H, Kong W Y, Kim Y C, Yoon S-J and Choi J-W 2012 Electrochemical properties of $Li[Li_{0.2}Mn_{0.54}Co_{0.13}Ni_{0.13}]O_2$ cathode thin film by RF sputtering for all-solid-state lithium battery *J. Solid State Chem.* **196** 288–92
[312] Martha S K, Nanda J, Veith G M and Dudney N J 2012 Electrochemical and rate performance study of high-voltage lithium-rich composition: li1.2Mn0.525Ni0.175Co 0.1O2 *J. Power Sources* **199** 220–6
[313] Ariyoshi K, Yamato R and Ohzuku T 2005 Zero-strain insertion mechanism of $Li[Li_{1/3}Ti_{5/3}]O_4$ for advanced lithium-ion (shuttlecock) batteries *Electrochim. Acta* **51** 1125–9
[314] Priyono B, Winowatan P W, Syahrial A Z, Faizah and Subhan A 2018 Optimizing the performance of $Li_4Ti_5O_{12}$/LTO by addition of silicon microparticle in half cell litium-ion battery anode *IOP Conf. Ser.: Earth Environ. Sci.* **105** 012121
[315] Xu W, Wang J, Ding F, Chen X, Nasybulin E, Zhang Y and Zhang J-G 2014 Lithium metal anodes for rechargeable batteries *Energy Environ. Sci.* **7** 513–37
[316] Cho S J, Uddin M J and Alaboina P 2017 Review of nanotechnology for cathode materials in batteries ed L M Rodriguez-Martinez and N Omar *Micro and Nano Technologies, Emerging Nanotechnologies in Rechargeable Energy Storage Systems* (Amsterdam: Elsevier) ch 3, pp 83–129
[317] Lee S J, Lee J K, Chung S H, Lee H Y, Lee S M and Baik H K 2001 Stress effect on cycle properties of the silicon thin-film anode *J. Power Sources* **97–98** 191–3

[318] Lee G, Schweizer S L and Wehrspohn R B 2014 CMOS-compatible metal-stabilized nanostructured Si as anodes for lithium-ion microbatteries *Nanoscale Res. Lett.* **9** 613
[319] Polat B D, Keles O and Amine K 2015 Silicon-copper helical arrays for new generation lithium ion batteries *Nano Lett.* **15** 6702–8
[320] Kasemchainan J, Zekoll S, Spencer Jolly D, Ning Z, Hartley G O, Marrow J and Bruce P G 2019 Critical stripping current leads to dendrite formation on plating in lithium anode solid electrolyte cells *Nat. Mater.* **18** 1105–11
[321] Neudecker B J, Dudney N J and Bates J B 2000 "Lithium-free" thin-film battery with *in situ* plated Li anode *J. Electrochem. Soc.* **147** 517
[322] Lee Y-G, Fujiki S, Jung C, Suzuki N, Yashiro N, Omoda R, Ko D-S, Shiratsuchi T, Sugimoto T, Ryu S, Ku J H, Watanabe T, Park Y, Aihara Y, Im D and Han I T 2020 High-energy long-cycling all-solid-state lithium metal batteries enabled by silver–carbon composite anodes *Nat. Energy* **5** 299–308
[323] Kanehori K, Matsumoto K, Miyauchi K and Kudo T 1983 Thin film solid electrolyte and its application to secondary lithium cell *Solid State Ion.* **9–10** 1445–8
[324] Brett S 2018 Applications of thin film batteries (AzoM) (available at: www.azom.com/article.aspx?ArticleID=15741) (Accessed 12 October 2022)
[325] Sastre J, Chen X, Aribia A, Tiwari A N and Romanyuk Y E 2020 Fast charge transfer across the $Li_7La_3Zr_2O_{12}$ solid electrolyte/$LiCoO_2$ cathode interface enabled by an interphase-engineered all-thin-film architecture *ACS Appl. Mater. Interfaces* **12** 36196–207
[326] TDK 2019 *CeraCharge- Rechargeable solid-state SMD battery* (available at: www.tdk-electronics.tdk.com/en/ceracharge)
[327] Cymbet Corporation- 2019 EnerChip™ Bare Die CBC005/CBC015/CBC050—EnerChip bare die (available at: www.cymbet.com/wp-content/uploads/2019/02/DS-72-41-v6.pdf)
[328] Front Edge Technology, Inc. A thin film battery company (available at: http://frontedgetechnology.com/tech.htm)
[329] Infinite power solutions-THINERGY®MEC202 Solid-state, Flexible, Rechargeable Thin-Film Micro-Energy Cell (available at: https://media.digikey.com/pdf/Data%20Sheets/Infinite%20Power%20Solutions%20PDFs/MEC202.pdf)
[330] 2014 EnFilm ™—rechargeable solid state lithium thin film battery (available at: www.st.com/en/power-management/efl700a39.html)
[331] Bates J B, Dudney N J, Neudecker B, Ueda A and Evans C D 2000 Thin-film lithium and lithium-ion batteries *Solid State Ion.* **135** 33–45
[332] Gockeln M, Glenneberg J, Busse M, Pokhrel S, Mädler L and Kun R 2018 Flame aerosol deposited $Li_4Ti_5O_{12}$ layers for flexible, thin film all-solid-state Li-ion batteries *Nano Energy* **49** 564–73
[333] Yamamoto T, Iwasaki H, Suzuki Y, Sakakura M, Fujii Y, Motoyama M and Iriyama Y 2019 A Li-free inverted-stack all-solid-state thin film battery using crystalline cathode material *Electrochem. commun.* **105** 106494
[334] Taberna P L, Mitra S, Poizot P, Simon P and Tarascon J M 2006 High rate capabilities Fe_3O_4-based Cu nano-architectured electrodes for lithium-ion battery applications *Nat. Mater.* **5** 567–73
[335] Mazor H, Golodnitsky D, Burstein L and Peled E 2009 High power copper sulfide cathodes for thin-film microbatteries *Electrochem. Solid-State Lett.* **12** A232
[336] Baggetto L, Knoops H C M, Niessen R A H, Kessels W M M and Notten P H L 2010 3D negative electrode stacks for integrated all-solid-state lithium-ion microbatteries *J. Mater. Chem.* **20** 3703–8
[337] Zhu Y, Gonzalez-Rosillo J C, Balaish M, Hood Z D, Kim K J and Rupp J L M 2021 Lithium-film ceramics for solid-state lithionic devices *Nat. Rev. Mater.* **6** 313–31
[338] TG 2018 Li-ion ANSMANN specifications for model : Li—ion battery 3. 6V 3500mAh with inside protection board (PCB) (available at: www.mega-piles.com/docs/pdf/557.pdf)
[339] HHTM Widex unveils fuel cell powered hearing aid (available at: https://hearinghealthmatters.org/blog/2019/widex-fuel-cell-hearing-aid-evoke/)
[340] Basmaji T, Alamri D, Habash O, Salim R, Alkhedher M and Ghazal M 2021 Hydrogen-based PEM fuel cells for low-cost sustainable powering of IoT systems *2021 Int. Conf. on Decision Aid Sciences and Application (DASA)* (*Sakheer, Bahrain*) pp 436–40
[341] Curry J and Harris N 2019 Powering the environmental internet of things *Sensors* **19** 1940
[342] Akimoto Y, Takezawa H, Iijima Y, Suzuki S-N and Okajima K 2020 Comparative analysis of fuel cell and battery energy systems for internet of things devices *Energy Rep.* **6** 29–35
[343] Peighambardoust S J, Rowshanzamir S and Amjadi M 2010 Review of the proton exchange membranes for fuel cell applications *Int. J. Hydrog. Energy* **35** 9349–84
[344] Yu J, Cheng P, Ma Z and Yi B 2003 Fabrication of a miniature twin-fuel-cell on silicon wafer *Electrochim. Acta* **48** 1537–41
[345] Morisawa I, Suzuki T, Katayama N, Dowaki K and Hayase M 2014 Miniature fuel cell with monolithically fabricated Si electrodes-uniformity of catalyst layer thickness *J. Phys.: Conf. Ser.* **557** 012108
[346] Gautier G 2018 Micro fuel cells based on silicon materials *Portable Hydrogen Energy Systems: Fuel Cells and Storage Fundamentals and Applications* (New York: Elsevier) ed Ferreira-Aparicio P and Chaparro A M ch 7, pp 107–23
[347] Yu Y, Wang Y, Zhang S, Zhang P, Xue S, Xie Y, Zhou Z, Li J and Kang J 2019 The construction of integrated Si-based micro proton exchange membrane fuel cells with improved performances *Nano Energy* **61** 604–10
[348] Evans A, Bieberle-Hütter A, Rupp J L M and Gauckler L J 2009 Review on microfabricated micro-solid oxide fuel cell membranes *J. Power Sources* **194** 119–29
[349] Chiabrera F, Garbayo I, Alayo N and Tarancón A 2017 Micro solid oxide fuel cells: a new generation of micro-power sources for portable applications *Smart Sensors, Actuators, and MEMS VIII* vol 10246 p 102460S
[350] Garbayo I, Tarancón A, Santiso J, Peiró F, Alarcón-Lladó E, Cavallaro A, Gràcia I, Cané C and Sabaté N 2010 Electrical characterization of thermomechanically stable YSZ membranes for micro solid oxide fuel cells applications *Solid State Ion.* **181** 322–31
[351] Chiabrera F, Garbayo I, López-Conesa L, Martín G, Ruiz-Caridad A, Walls M, Ruiz-González L, Kordatos A, Núñez M, Morata A, Estradé S, Chroneos A, Peiró F and Tarancón A 2019 Engineering transport in manganites by tuning local nonstoichiometry in grain boundaries *Adv. Mater.* **31** 1805360
[352] Chiabrera F, Baiutti F, Diercks D, Cavallaro A, Aguadero A, Morata A and Tarancón A 2022 Visualizing local fast ionic conduction pathways in nanocrystalline lanthanum manganite by isotope exchange-atom probe tomography *J. Mater. Chem.* A **10** 2228–34
[353] Baiutti F, Chiabrera F, Diercks D, Cavallaro A, Yedra L, López-Conesa L, Estradé S, Peiró F, Morata A, Aguadero A and Tarancón A 2021 Direct measurement of oxygen mass transport at the nanoscale *Adv. Mater.* **33** 2105622

[354] Sanna S, Esposito V, Andreasen J W, Hjelm J, Zhang W, Kasama T, Simonsen S B, Christensen M, Linderoth S and Pryds N 2015 Enhancement of the chemical stability in confined δ -Bi_2O_3 *Nat. Mater.* **14** 500–4
[355] Sanna S, Esposito V, Tebano A, Licoccia S, Traversa E and Balestrino G 2010 Enhancement of ionic conductivity in Sm-doped ceria/yttria-stabilized zirconia heteroepitaxial structures *Small* **6** 1863–7
[356] Janek J, Martin M and Becker K D 2009 Physical chemistry of solids—the science behind materials engineering: Concepts, Models, Methods *Zeitschrift für Physikalische Chemie* **223**
[357] Develos-Bagarinao K, Ishiyama T, Kishimoto H, Shimada H and Yamaji K 2021 Nanoengineering of cathode layers for solid oxide fuel cells to achieve superior power densities *Nat. Commun.* **12** 3979
[358] Garbayo I, Chiabrera F, Alayo N, Santiso J, Morata A and Tarancón A 2019 Thin film oxide-ion conducting electrolyte for near room temperature applications *J. Mater. Chem.* A **7** 25772–8
[359] Garcia-Barriocanal J, Rivera-Calzada A, Varela M, Sefrioui Z, Iborra E, Leon C, Pennycook S J and Santamaria J 2008 Colossal ionic conductivity at interfaces of epitaxial ZrO_2: Y_2O_3/$SrTiO_3$Heterostructures *Science* **321** 676–81
[360] Gunkel F, Christensen D V and Pryds N 2020 Charge-transfer engineering strategies for tailored ionic conductivity at oxide interfaces *J. Mater. Chem.* C **8** 11354–9
[361] Baiutti F, Chiabrera F, Acosta M, Diercks D, Parfitt D, Santiso J, Wang X, Cavallaro A, Morata A, Wang H, Chroneos A, MacManus-Driscoll J and Tarancon A 2021 A high-entropy manganite in an ordered nanocomposite for long-term application in solid oxide cells *Nat. Commun.* **12** 2660
[362] Garbayo I, Baiutti F, Morata A and Tarancón A 2019 Engineering mass transport properties in oxide ionic and mixed ionic-electronic thin film ceramic conductors for energy applications *J. Eur. Ceram. Soc.* **39** 101–14
[363] Wen K, Lv W and He W 2015 Interfacial lattice-strain effects on improving the overall performance of micro-solid oxide fuel cells *J. Mater. Chem.* A **3** 20031–50
[364] Shin J W, Go D, Kye S H, Lee S and An J 2019 Review on process-microstructure-performance relationship in ALD-engineered SOFCs *J. Phys. Energy* **1** 042002
[365] Pla D, Sánchez-González A, Garbayo I, Salleras M, Morata A and Tarancón A 2015 Is it possible to design a portable power generator based on micro-solid oxide fuel cells? A finite volume analysis *J. Power Sources* **293** 264–73
[366] Scherrer B, Evans A, Santis-Alvarez A J, Jiang B, Martynczuk J, Galinski H, Nabavi M, Prestat M, Tölke R, Bieberle-Hütter A, Poulikakos D, Muralt P, Niedermann P, Dommann A, Maeder T, Heeb P, Straessle V, Muller C and Gauckler L J 2014 A thermally self-sustained micro-power plant with integrated micro-solid oxide fuel cells, micro-reformer and functional micro-fluidic carrier *J. Power Sources* **258** 434–40
[367] FuelCellsWorks (available at: https://fuelcellsworks.com/news/widex-named-as-ces)
[368] Bieberle-Hütter A, Beckel D, Infortuna A, Muecke U P, Rupp J L M, Gauckler L J, Rey-Mermet S, Muralt P, Bieri N R, Hotz N, Stutz M J, Poulikakos D, Heeb P, Müller P, Bernard A, Gmür R and Hocker T 2008 A micro-solid oxide fuel cell system as battery replacement *J. Power Sources* **177** 123–30
[369] An J, Kim Y-B, Park J, Gür T M and Prinz F B 2013 Three-dimensional nanostructured bilayer solid oxide fuel cell with 1.3 W/cm^2 at 450 C *Nano Lett.* **13** 4551–5
[370] Chao C-C, Hsu C-M, Cui Y and Prinz F B 2011 Improved solid oxide fuel cell performance with nanostructured electrolytes *ACS Nano* **5** 5692–6
[371] Tölke R, Bieberle-Hütter A, Evans A, Rupp J L M and Gauckler L J 2012 Processing of Foturan® glass ceramic substrates for micro-solid oxide fuel cells *J. Eur. Ceram. Soc.* **32** 3229–38
[372] Muecke U P, Beckel D, Bernard A, Bieberle-Hütter A, Graf S, Infortuna A, Müller P, Rupp J L M, Schneider J and Gauckler L J 2008 Micro solid oxide fuel cells on glass ceramic substrates *Adv. Funct. Mater.* **18** 3158–68
[373] Schlupp M V F, Evans A, Martynczuk J and Prestat M 2014 Micro-solid oxide fuel cell membranes prepared by aerosol-assisted chemical vapor deposition *Adv. Energy Mater.* **4** 1301383
[374] Kerman K, Lai B-K and Ramanathan S 2011 Pt/$Y_{0.16}Zr_{0.84}O_{1.92}$/Pt thin film solid oxide fuel cells: electrode microstructure and stability considerations *J. Power Sources* **196** 2608–14
[375] Tsuchiya M, Lai B-K and Ramanathan S 2011 Scalable nanostructured membranes for solid-oxide fuel cells *Nat. Nano* **6** 282–6
[376] Kerman K, Lai B-K and Ramanathan S 2012 Free standing oxide alloy electrolytes for low temperature thin film solid oxide fuel cells *J. Power Sources* **202** 120–5
[377] Kerman K, Lai B -K and Ramanathan S 2012 Nanoscale compositionally graded thin-film electrolyte membranes for low-temperature solid oxide fuel cells *Adv. Energy Mater.* **2** 656–61
[378] Kerman K, Xuza S and Ramanathan S 2015 Free standing yttria-doped zirconia membranes: geometrical effects on stability *J. Electroceramics* **34** 91–99
[379] Garbayo I, Pla D, Morata A, Fonseca L, Sabaté N, Tarancón A, Sabate N and Tarancon A 2014 Full ceramic micro solid oxide fuel cells: towards more reliable MEMS power generators operating at high temperatures *Energy Environ. Sci.* **7** 3617–29
[380] Baek J D, Yoon Y-J, Lee W and Su P-C 2015 A circular membrane for nano thin film micro solid oxide fuel cells with enhanced mechanical stability *Energy Environ. Sci.* **8** 3374–80
[381] Baek J D, Yu C-C and Su P-C 2016 A silicon-based nanothin film solid oxide fuel cell array with edge reinforced support for enhanced thermal mechanical stability *Nano Lett.* **16** 2413–7
[382] Kim K J, Park B H, Kim S J, Lee Y, Bae H and Choi G M 2016 Micro solid oxide fuel cell fabricated on porous stainless steel: a new strategy for enhanced thermal cycling ability *Sci. Rep.* **6** 22443
[383] Joo J H and Choi G M 2008 Simple fabrication of micro-solid oxide fuel cell supported on metal substrate *J. Power Sources* **182** 589–93
[384] Shin S S, Kim J H, Bae K T, Lee K-T, Kim S M, Son J -W, Choi M and Kim H 2020 Multiscale structured low-temperature solid oxide fuel cells with 13 W power at 500 °c *Energy Environ. Sci.* **13** 3459–68
[385] Kwon C-W, Son J-W, Lee J-H, Kim H-M, Lee H-W and Kim K-B 2011 High-performance micro-solid oxide fuel cells fabricated on nanoporous anodic aluminum oxide templates *Adv. Funct. Mater.* **21** 1154–9
[386] Park J, Chang I, Paek J Y, Ji S, Lee W, Cha S W and Lee J-M 2014 Fabrication of the large area thin-film solid oxide fuel cells *CIRP Annal* **63** 513–6
[387] Oh S, Park J, Shin J W, Yang B C, Zhang J, Jang D Y and An J 2018 High performance low-temperature solid oxide fuel cells with atomic layer deposited-yttria stabilized zirconia embedded thin film electrolyte *J. Mater. Chem.* A **6** 7401–8
[388] Ha S, Su P-C and Cha S-W 2013 Combinatorial deposition of a dense nano-thin film YSZ electrolyte for low temperature solid oxide fuel cells *J. Mater. Chem.* A **1** 9645–9

[389] Shin J W, Oh S, Lee S, Yu J-G, Park J, Go D, Yang B C, Kim H J and An J 2019 Ultrathin atomic layer-deposited CeO_2 overlayer for high-performance fuel cell electrodes *ACS Appl. Mater. Interfaces* **11** 46651–7
[390] Li Y, Wang S and Su P C 2016 Proton-conducting micro-solid oxide fuel cells with improved cathode reactions by a nanoscale thin film gadolinium-doped ceria interlayer *Sci. Rep.* **6** 22369
[391] Kim Y B, Gür T M, Kang S, Jung H-J, Sinclair R and Prinz F B 2011 Crater patterned 3D proton conducting ceramic fuel cell architecture with ultra thin Y:$BaZrO_3$ electrolyte *Electrochem. commun.* **13** 403–6
[392] Chang I, Heo P and Cha S W 2013 Thin film solid oxide fuel cell using a pinhole-free and dense Y-doped $BaZrO_3$ *Thin Solid Films* **534** 286–90
[393] Reolon R P, Sanna S, Xu Y, Lee I, Bergmann C P, Pryds N and Esposito V 2018 Effects of accelerated degradation on metal supported thin film-based solid oxide fuel cells *J. Mater. Chem.* A **6** 7887–96
[394] Noh H S, Yoon K J, Kim B K, Je H J, Lee H W, Lee J H and Son J W 2014 The potential and challenges of thin-film electrolyte and nanostructured electrode for yttria-stabilized zirconia-base anode-supported solid oxide fuel cells *J. Power Sources* **247** 105–11
[395] Milliken R J, Silva-Martínez J and Sánchez-Sinencio E 2007 Full on-chip CMOS low-dropout voltage regulator *IEEE Trans. on Circuits and Systems I: Regular Papers, no. 9* vol 54 pp 1879–90
[396] Okuma Y, Ishida K, Ryu Y, Zhang X, Chen P H, Watanabe K, Takamiya M and Sakurai T 2010 0.5-V input digital LDO with 98.7% current efficiency and 2.7-μA quiescent current in 65nm CMOS *IEEE Custom Integrated Circuits Conf. 2010* (*San Jose, CA, 2010*) pp 1–4
[397] Park Y-J, Park J-H, Kim H-J, Ryu H, Kim S, Pu Y, Hwang K-C, Yang Y, Lee M and Lee K-Y 2017 A design of a 92.4% efficiency triple mode control DC-DC buck converter with low power retention mode and adaptive zero current detector for IoT/wearable applications *IEEE Trans. on Power Electronics* **32** 6946–60
[398] Chen C W and Fayed A 2015 A low-power dual-frequency SIMO buck converter topology with fully-integrated outputs and fast dynamic operation in 45 nm CMOS *IEEE J. Solid-State Circuits* **50** 2161–73
[399] Safarian Z and Hashemi H 2014 Capacitance-sharing, dual-output, compact, switched-capacitor DC-DC converter for low-power biomedical implants *Electron. Lett.* **50** 1673–5
[400] Larsen D Ø, Vinter M and Jørgensen I 2019 Systematic synthesis of step-down switched-capacitor power converter topologies **66** 863–7
[401] Elhebeary M and Yang C-K K 2020 A 92%-efficiency battery powered hybrid DC-DC converter for IoT applications *IEEE Trans. on Circuits and Systems I: Regular Papers* **67** 3342–51
[402] Wieckowski M, Chen G K, Seok M, Blaauw D and Sylvester D 2009 Hybrid DC-DC converter for sub-microwatt sub-1V implantable applications *2009 Symp. on VLSI Circuits* (*Kyoto, Japan, 2009*) vol 91 pp 166–7
[403] Li J, Seo J S, Kymissis I and Seok M 2017 Triple-mode, hybrid-storage, energy harvesting power management unit: achieving high efficiency against harvesting and load power variabilities *IEEE J. Solid-State Circuits* **52** 2550–62
[404] Elgendy M A, Zahawi B and Atkinson D J 2012 Assessment of perturb and observe MPPT algorithm implementation techniques for PV pumping applications *IEEE Trans. on Sustainable Energy* **3** 21–33
[405] Selvan D S 2013 Modeling and simulation of incremental conductance MPPT algorithm for photovoltaic applications *Int. J. Sci. Eng. Technol.* **2** 681–5
[406] Carreon-Bautista S, Huang L and Sanchez-Sinencio E 2016 An autonomous energy harvesting power management unit with digital regulation for IoT applications *IEEE J. Solid-State Circuits* **51** 1457–74
[407] Dini M, Romani A, Filippi M and Tartagni M 2015 A nanocurrent power management IC for low-voltage energy harvesting sources *IEEE Trans. Power Electron.* **30** 5665–80
[408] Rajendran M K, Kansal S, Mantha A, Priya V, Priyamvada Y B and Dutta A 2016 Automated environment aware nW FOCV—MPPT controller for self-powered IoT applications *2016 IEEE Int. Symp. on Circuits and Systems (ISCAS)* (*Montreal, QC, Canada*) pp 1818–21
[409] Le H T, Member S, Nour Y, Pavlovic Z, Knott A and Jensen F 2019 High- Q three-dimensional microfabricated magnetic-core toroidal inductors for power *IEEE Trans. Power Electron.* **34** 74–85
[410] Lê H T 2018 Microfabricated 3D inductors for integrated switched-mode power supplies *PhD Thesis* Technical University of Denmark
[411] Yuan F, Zhang Q T, Jin S and Zhu H 2015 Optimal harvest-use-store strategy for energy harvesting wireless systems *IEEE Trans. Wirel. Commun.* **14** 698–710